

University of Kentucky

UKnowledge

Theses and Dissertations--Chemistry

Chemistry

2023

FIRST PRINCIPLES CALCULATIONS TO INVESTIGATE SURFACE AND CATALYTIC PROPERTIES OF MATERIALS FOR GREEN ENERGY GENERATION

Keerthan Raghavendra Rao

University of Kentucky, keerthanr1@gmail.com

Author ORCID Identifier:

 <https://orcid.org/0000-0003-2557-2374>

Digital Object Identifier: <https://doi.org/10.13023/etd.2023.432>

[Right click to open a feedback form in a new tab to let us know how this document benefits you.](#)

Recommended Citation

Rao, Keerthan Raghavendra, "FIRST PRINCIPLES CALCULATIONS TO INVESTIGATE SURFACE AND CATALYTIC PROPERTIES OF MATERIALS FOR GREEN ENERGY GENERATION" (2023). *Theses and Dissertations--Chemistry*. 183.

https://uknowledge.uky.edu/chemistry_etds/183

This Doctoral Dissertation is brought to you for free and open access by the Chemistry at UKnowledge. It has been accepted for inclusion in Theses and Dissertations--Chemistry by an authorized administrator of UKnowledge. For more information, please contact UKnowledge@lsv.uky.edu.

STUDENT AGREEMENT:

I represent that my thesis or dissertation and abstract are my original work. Proper attribution has been given to all outside sources. I understand that I am solely responsible for obtaining any needed copyright permissions. I have obtained needed written permission statement(s) from the owner(s) of each third-party copyrighted matter to be included in my work, allowing electronic distribution (if such use is not permitted by the fair use doctrine) which will be submitted to UKnowledge as Additional File.

I hereby grant to The University of Kentucky and its agents the irrevocable, non-exclusive, and royalty-free license to archive and make accessible my work in whole or in part in all forms of media, now or hereafter known. I agree that the document mentioned above may be made available immediately for worldwide access unless an embargo applies.

I retain all other ownership rights to the copyright of my work. I also retain the right to use in future works (such as articles or books) all or part of my work. I understand that I am free to register the copyright to my work.

REVIEW, APPROVAL AND ACCEPTANCE

The document mentioned above has been reviewed and accepted by the student's advisor, on behalf of the advisory committee, and by the Director of Graduate Studies (DGS), on behalf of the program; we verify that this is the final, approved version of the student's thesis including all changes required by the advisory committee. The undersigned agree to abide by the statements above.

Keerthan Raghavendra Rao, Student

Dr. Chad Michael Risko, Major Professor

Dr. Kenneth Graham, Director of Graduate Studies

FIRST PRINCIPLES CALCULATIONS TO INVESTIGATE SURFACE AND
CATALYTIC PROPERTIES OF MATERIALS FOR GREEN ENERGY GENERATION

DISSERTATION

A dissertation submitted in partial fulfillment of the
requirements for the degree of Doctor of Philosophy in the
College of Arts and Sciences
at the University of Kentucky

By

Keerthan Raghavendra Rao

Lexington, Kentucky

Director: Dr. Chad M. Risko, Professor of Chemistry

Lexington, Kentucky

2023

Copyright © Keerthan Raghavendra Rao 2023
<https://orcid.org/0000-0003-2557-2374>

ABSTRACT OF DISSERTATION

FIRST PRINCIPLES CALCULATIONS TO INVESTIGATE SURFACE AND CATALYTIC PROPERTIES OF MATERIALS FOR GREEN ENERGY GENERATION

Climate change due to greenhouse gas build up in the earth's atmosphere is an existential threat to humanity. To mitigate climate change, a significant shift from fossil fuels is necessary. Over the years, several renewable energy sources like solar, wind, geothermal etc. have been explored with the aim providing carbon-free energy. In this work, we focus on using density functional theory (DFT) methods to investigate key functional properties of materials of interest for applications in solar cells and catalytic conversion for energy generation. We show geometric effects of carboxylic acid binding on a transition metal surface to impact the deoxygenation reaction mechanism. Using insights from binding energy calculations and transition state theory, we elucidate the reaction pathway. We then use the same methods to investigate the surface of perovskites substituted with organic ligands and show the effect of fluorination of the phenyl ring of anilinium on the relative surface energy, relative binding energy, surface penetration, work function, and surface electronic properties. Lastly, we turn to DFT studies of molecular systems to investigate the impact of a perylene diimide (PDI) chromophore substituted on a rhenium-based organometallic complex. We show that unfolding of the PDI away from the organometallic complex is a key step in the catalytic reduction of CO₂ and demonstrate how the PDI acts as an electronic reservoir during this process.

KEYWORDS: Density Functional Theory, Catalysis, Green Energy Generation, Surface Binding, Reaction Mechanisms, Electron Reservoir

Keerthan Raghavendra Rao

(Name of Student)

08/15/2023

Date

FIRST PRINCIPLES CALCULATIONS TO INVESTIGATE SURFACE AND
CATALYTIC PROPERTIES OF MATERIALS FOR GREEN ENERGY GENERATION

By
Keerthan Raghavendra Rao

Dr. Chad Michael Risko

Director of Dissertation

Dr. Kenneth Graham

Director of Graduate Studies

08/15/2023

Date

DEDICATION

To humanity and our beloved world, in hope that my work lays the foundation for a better future with clean air, water and food for all to thrive.

To my mother Nanda, who endured all the pain so I could have a comfortable life, this work is a result of that comfort and your never-ending love and support.

To my brothers Kaushal and Kedaar, for charting an inspiring path for me to follow, I hope this work embodies the values we share- hard work, perseverance, and integrity.

To Rosa, the love of my life, for showing me that no challenge is too big and together, we can overcome anything. This work is a result of that belief.

Last but not the least, to my advisor Dr. Chad Risko, for all the support, direction and belief in me even when I could not see it myself. I hope this is only a beginning of our partnered contribution to society.

Thank you.

ACKNOWLEDGMENTS

As a graduate student, I am incredibly indebted to many individuals who have shaped my personality, skills, abilities and most importantly values that define me. My acknowledgements are not limited to these words and certainly is not limited to the people and organizations mentioned here. To begin, I would like to acknowledge my research advisor Professor Chad Risko for giving me an opportunity to explore my research abilities, challenge me to become better at what I do, explore new endeavors and guide me to a successful completion of this program. I sincerely thank you for your mentorship that has shaped my future and hope to carry on the service with grace and humility.

I am incredibly thankful to the University of Kentucky for this opportunity that has shaped me to become stronger, more responsible and confident in my abilities as a researcher.

My wholehearted thanks to all my committee members, Professors Mark Crocker, Doo Young Kim, and Mathew Beck for their guidance that has led to successfully carry out this work. My sincere thanks to all the Professors and course instructors that imparted me with the necessary knowledge to carry out my research. A special thanks to Professors Dong-Sheng Yang and Mark Crocker for their incredible courses that inspired this work. I would also like to thank my teaching supervisor and all the staff members that helped me navigate my way through the program.

I would like to thank Dr. Eduardo Santillan-Jimenez for his support and direction for the work on decarbonylation of carboxylic acid and general insights on navigating the graduate student life. My sincere thanks to Dr. Robert Pace for his insights and

contribution that supports this work. I would also like to thank Hanna Suarez who helped me grow as a mentor and develop a deeper understanding of my work and its implications.

It has been a privilege to be a part of a fantastic group of researchers at the Risko Lab. I would like to thank Vinayak Bhat for his incredible support over the years that improved my research significantly. I would like to thank Dr. Ling-Yi Huang for his incredible insights and support, Dr. Joel Bombile and Dr. Connor Callaway for their encouragement throughout my journey. I would like to thank Ayanthi Thisera for her contribution to shape my work and expand my knowledge. I would like to thank Anton Uswanththa Perera for his ideas and encouragement, Rebekah Duke for her pin-point insights that has vastly improved my presentation skills, and Parker Sornberger for his encouragement and lively demeanor that filled the void left in wake of the pandemic.

I would like to thank all my friends for their constant support in various ways throughout my journey as a graduate student. Special thanks to Rutika, Nikhil, and Swetalina who kept me grounded when success arrived at my doorstep and lifted me when setbacks slowed me down.

I am incredibly thankful to Rosa Delgado, the love of my life, for her love, support and making me a better person.

I am immensely grateful to my mother Nanda CH, for her incredible and omnipresent love, comfort and support, without which this work would not have been possible. I strongly acknowledge my brothers Kaushal and Kedaar who kept me grounded and motivated to always do better.

TABLE OF CONTENTS

ACKNOWLEDGMENTS	iii
LIST OF TABLES	vii
LIST OF FIGURES	viii
CHAPTER 1. INTRODUCTION	1
1.1 Energy outlook, challenges and potential	1
1.2 Heterogeneous catalysis for biofuel generation	2
1.3 Perovskite solar cells for electricity generation	5
1.4 Organometallics for CO ₂ conversion	8
1.5 Objectives and outline of the dissertation	12
CHAPTER 2. METHODS	16
2.1 Density functional theory (DFT)	16
2.1.1 Wave functions to electron density	18
2.1.2 Exchange-correlation functional:	22
2.1.3 Periodic DFT	25
2.1.4 Pseudopotentials	28
2.2 Nudged elastic band and dimer method	29
2.2.1 Dimer method	32
2.3 Microkinetic modeling	36
2.3.1 Rate of a reaction	36
2.3.2 Steady state approximation	37
2.3.3 Potential energy surface and kinetic parameters	38
2.3.4 Mean-field approximation	39
2.3.5 Steps in microkinetic modeling	40
2.4 Surface energy	41
2.5 Adsorption energy	42

2.6	Spin density.....	43
CHAPTER 3. CARBOXYLIC ACID DECARBONYLATION ON NICKEL: THE CRITICAL ROLE OF THE ACID BINDING GEOMETRY		
3.1	Introduction.....	45
3.2	Methods.....	45
3.3	Results and Discussion	48
3.3.1	Determining the DCN reaction mechanism.....	48
3.3.1.1	Binding energies and stable modes.....	50
3.3.2	Microkinetic modeling.....	59
3.3.2.1	Lateral interaction effect.....	67
3.4	Conclusion	75
CHAPTER 4. IMPACT OF FLUORINATED ANILINIUM-BASED LIGANDS ON THE SURFACE ELECTRONIC PROPERTIES OF FORMAMIDINIUM TIN IODIDE (FASNI ₃) PEROVSKITE.....		
4.1	Introduction.....	77
4.2	Methods.....	78
4.3	Results and Discussion	80
4.4	Conclusion	94
CHAPTER 5. DFT STUDIES OF CO ₂ REDUCTION USING N-ANNULATED PERYLENE DIIMIDE RHENIUM BIPYRIDINE DYADS		
5.1	Introduction.....	95
5.2	Methods.....	95
5.3	Results and discussion	96
5.3.1	Electronic and optical properties of PDI and PDI ⁻	97
5.3.2	Investigation of CO ₂ reduction mechanism using Re(bpy-C2-PDI).....	100
5.4	Conclusions.....	129
CHAPTER 6. SYNOPSIS		
6.1	Conclusions and future perspective	132
VITA.....		156

LIST OF TABLES

Table 3.1 Adsorption energies of key DCN intermediates in the most stable binding modes, where * indicates surface intermediate.	52
Table 3.2 Reaction free energy, Activation barrier and Entropy correction terms for each elementary step without lateral interaction effect. All energies are in eV.	54
Table 3.3 Shorthand notation of DCN reaction intermediates.	62
Table 3.4 List of all elementary steps in the DCN mechanism	63
Table 3.5 Zero-point energy corrected activation energy barrier, reaction free energy change, and turnover frequency for each elementary step involved in the DCN mechanism of PAc on Ni[111] with lateral interaction effects included.	69
Table 4.1 Surface energy, relative binding energy, work function, N–I distance, \angle I–Sn–I and \angle Sn–I–Sn of periodic surfaces at PBE+U level of theory.	85

LIST OF FIGURES

Figure 1.1 A generic architecture of a perovskite solar cell with indium tin oxide (ITO) as the glass substrate, electron transport layer (ETL), perovskite, hole transport layer (HTL) and an electrode.	6
Figure 2.1 Periodic reciprocal lattice describing the Irreducible Brillouin Zone (IBZ). ..	27
Figure 2.2 A comparison between NEB and cNEB showing an image at the saddle point of the cNEB calculation.	32
Figure 2.3 Definition of various position, force and rotational vectors. All rotational vectors are in the plane of rotation. Image taken from Henkelman and co-workers. ¹⁴⁸	34
Figure 2.4 Movement of the dimer towards the saddle point as a result of the effective force acting at the center of the dimer taken from Henkelman and co-workers. ¹⁴⁸	35
Figure 2.5 Potential energy diagram depicting E_a and E_{rxn} for a reaction $A \rightarrow B$	39
Figure 3.1 Binding modes of PAc on Ni[111] surface determined from DFT calculations with ZPE corrected adsorption energies. PAc structures in (A) was reproduced from [18]. Copyright [2020] American Chemical Society. While structures in (B) include PAc obtained from the NIST database. The difference between the two PAc structures is depicted by the green curved arrow indicating the internal C-C bond rotation of the molecule.	49
Figure 3.2 Stable binding modes of DCN intermediates on Ni[111] surface with top-view and side-view (Blue=Ni; Black=C; White=H; Red=O). (a) CH_3CH_2COOH (b) $CH_3CHCOOH$ (c) CH_3CCOOH (d) CH_3CCO (e) CH_3CH_2CO (f) CH_3CHCO (g) CH_3CH (h) CH_3C (i) CH_3CH_2 (j) CO (k) OH (l) H	51

Figure 3.3 Free energy surface diagrams for three DCN reaction pathways on a Ni[111] surface with $CH_3CH_2COOH_{(g)} + H_{2(g)} + *$ as the reference state (transition states with an activation barrier are shown in red for each elementary step).....	59
Figure 3.4 Arrhenius plot built to determine the apparent activation energy for the overall rate of the PAc DCN reaction in the 473 to 673 K temperature range.	72
Figure 4.1 The bulk cubic structure of $FASnI_3$ perovskite (A) and the proposed surface ligands (B).....	78
Figure 4.2 The electronic density of states (DOS) (A) and the band structure (B) of the bulk cubic $FASnI_3$ perovskite determined at PBE+U level of theory. The DOS shows the nature of VBM and CBM with a slight indirect bandgap of 1.37 eV shown via the band structure.	81
Figure 4.3 Net dipole moments of fluorine substituted Aniline (An) based ligands calculated at M06L/6-31g(d,p) level of theory.	82
Figure 4.4 Periodic DFT optimized surfaces (side view) with 1ML coverage of each ligands. The surface structures shown here are the most stable modes.	83
Figure 4.5 Correlation diagram of net molecular dipole moment and the surface work function.	88
Figure 4.6 Vacuum potential and the fermi energy for 1ML coverage of An^+ and its fluorinated derivatives. The reference line chosen is with respect to An^+ on the surface.	89
Figure 4.7 Charge density difference plots (side view) of periodic surfaces at PBE+U level of theory where, the yellow and blue regions represent charge accumulation and depletion respectively.	92

Figure 4.8 Charge density difference plots (top) view of clean surface and 1ML of An^+ and its fluorinated derivatives. The figure depicts the regions of charge accumulation (yellow) and depletion (blue) on the ligands, Sn and I atoms.	94
Figure 5.1 Pictorial representations of select frontier molecular orbitals (MO) for PDI^- and PDI as determined at the M06/6-31G(d,p) level of theory.	98
Figure 5.2 Pyrrolic N-atom of the PDI molecule.	98
Figure 5.3 Simulated absorption spectra for PDI^- and PDI as determined via TDDFT calculations at the M06/6-31G(d,p) level of theory. The full width at half-maximum (fwhm) used in the gaussian convolution of the vertical excited states was 0.33 eV.	99
Figure 5.4 DFT-optimized structure of ground-state $Re(bpy-C2-PDI)$ determined at M06/6- 31G(d,p)/LANL2DZ level of theory.	101
Figure 5.5 Molecular orbital diagram of $Re(bpy-C2-PDI)$ (center), comprised of N-annulated PDI (left) and $Re(bpy-TAz)$ (right) as determined at the M06/6-31G(d,p)/LANL2DZ level of theory.	102
Figure 5.6 Proposed electrocatalytic CO_2 reduction cycle of $Re(bpy-C2-PDI)$. Optimized geometries and relevant HOMO or $HO\alpha O$ calculations were determined at the M06/6-31G(d,p)/LANL2DZ level of theory. Black, green, or blue coloration of the $Re(bpy-TAz)$ and PDI structural moieties indicate the presence of zero, one, or two electrons, respectively.	103
Figure 5.7 Face-on and side-on perspectives of the optimized geometry (A & C) and spin density map (B & D) for the doublet state of $Re^I(bpy-C2-PDI^{\bullet-})$ as determined at the M06/6- 31G(d,p)/LANL2DZ level of theory.	104

Figure 5.8 Frontier molecular orbitals of the doublet state of $\text{Re}^{\text{I}}(\text{bpy-C2-PDI}^{\bullet-})$ at the M06/6-31G(d,p)/LANL2DZ level of theory, where (A) represents $\text{HO}\alpha\text{O}$ and (B & C) represent the $\text{LU}\alpha\text{O}$ and $\text{LU}\beta\text{O}$ with α - and β -spins, respectively.	105
Figure 5.9 Face-on and side-on perspectives of the optimized geometry (A & C) and spin density map(B & D) for the triplet state of $\text{Re}^{\text{I}}(\text{bpy-C2-PDI}^{2-})$ as determined at the M06/6-31G(d,p)/LANL2DZ level of theory.....	106
Figure 5.10 Frontier molecular orbitals of the triplet state of $\text{Re}^{\text{I}}(\text{bpy-C2-PDI}^{2-})$ at the M06/6-31G(d,p)/LANL2DZ level of theory, where (A & B) represent the $\text{HO}\alpha\text{O-1}$ and $\text{HO}\alpha\text{O}$ with α -spins, respectively, and (C) is the $\text{LU}\beta\text{O}$ with β -spin.....	107
Figure 5.11 Frontier molecular orbitals of the singlet state of $\text{Re}^{\text{I}}(\text{bpy-C2-PDI}^{2-})$ at the M06/6-31G(d,p)/LANL2DZ level of theory, where (A) represents the HOMO and (B) is the LUMO.....	107
Figure 5.12 Face-on and side-on perspectives of the optimized geometry (A & C) and spin density map (B & D) for the doublet state of $\text{Re}^{\text{I}}(\text{bpy}^{\bullet-}\text{-C2-PDI}^{2-})$ as determined at the M06/6- 31G(d,p)/LANL2DZ level of theory.....	108
Figure 5.13 Frontier molecular orbitals of the doublet state of $\text{Re}^{\text{I}}(\text{bpy}^{\bullet-}\text{-C2-PDI}^{2-})$ at the M06/6-31G(d,p)/LANL2DZ level of theory, where (A) represents the HOMO with electrons paired on PDI, while (B & C) represent the $\text{HO}\alpha\text{O}$ and $\text{LU}\beta\text{O}$ with α - and β -spins, respectively.	109
Figure 5.14 Face-on and side-on perspectives of the optimized geometry (A & C) and spin density map (B & D) for the triplet state of $\text{Re}^{\text{0}}(\text{bpy}^{\bullet-}\text{-C2-PDI}^{2-})$ as determined at the M06/6- 31G(d,p)/LANL2DZ level of theory.....	110

Figure 5.15 Frontier molecular orbitals of the triplet state of $\text{Re}^0(\text{bpy}^{\bullet-}\text{-C2-PDI}^{2-})$ at the M06/6-31G(d,p)/LANL2DZ level of theory, where (A) represents the HOMO with paired electrons on PDI, and (B & C) are the α -spin $\text{HO}\alpha\text{O-1}$ and $\text{HO}\alpha\text{O}$, respectively.....	111
Figure 5.16 Molecular orbital diagram of $\text{Re}^0(\text{bpy}^{\bullet-}\text{-C2-PDI}^{2-})$ showing HOMO-1, HOMO, $\text{HO}\alpha\text{O}$, $\text{LU}\beta\text{O}$, and LUMO+1 as determined at the M06/6-31G(d,p)/LANL2DZ level of theory.	112
Figure 5.17 Molecular orbital diagram of $\text{Re}^I(\text{bpy}^{\bullet-}\text{-C2-PDI}^{2-})$ showing HOMO, $\text{HO}\alpha\text{O}$ and $\text{LU}\beta\text{O}$ as determined at the M06/6-31G(d,p)/LANL2DZ level of theory.	113
Figure 5.18 Face-on and side-on perspectives of the optimized geometry (A & C) and spin density map (B & D) for the doublet state of $\text{Re}^0(\text{bpy}^{\bullet-}\text{-C2-PDI}^{\bullet-})$ as determined at the M06/6-31G(d,p)/LANL2DZ level of theory.....	114
Figure 5.19 Frontier molecular orbitals of the doublet state of $\text{Re}^0(\text{bpy}^{\bullet-}\text{-C2-PDI}^{\bullet-})$ at the M06/6-31G(d,p)/LANL2DZ level of theory, where (A) represents the HOMO with paired electrons on $\text{Re}(\text{bpy})$, and (B & C) are the $\text{HO}\alpha\text{O}$ and $\text{LU}\beta\text{O}$ with α - and β -spins, respectively.	115
Figure 5.20 Molecular orbital diagram of $\text{Re}^0(\text{bpy}^{\bullet-}\text{-C2-PDI}^{\bullet-})$ showing HOMO-1, HOMO, $\text{HO}\alpha\text{O}$, $\text{LU}\beta\text{O}$, and LUMO+1 as determined at the M06/6-31G(d,p)/LANL2DZ level of theory.	116
Figure 5.21 Frontier molecular orbitals and spin density mapping at the M06/6-31G(d,p)/LANL2DZ level of theory for the doublet state of $\text{Re}^0(\text{bpy}^{\bullet-}\text{-C2-PDI}^{\bullet-})$ stabilized by an explicit molecule of DMF, where (A) represents the HOMO with paired electrons on $\text{Re}(\text{bpy})$, and (B & C) are the $\text{HO}\alpha\text{O}$ and $\text{LU}\beta\text{O}$ with α - and β -spins, respectively, and (D) is the spin density map.....	118

Figure 5.22 Frontier molecular orbitals and spin density mapping at the M06/6-31G(d,p)/LANL2DZ level of theory for the doublet state of $\text{Re}^0(\text{bpy}^{\bullet-}\text{-C2-PDI}^{\bullet-})$ stabilized by explicit protonation of PDI imide oxygens, where (A) represents the HOMO with paired electrons on $\text{Re}(\text{bpy})$, and (B & C) are the $\text{HO}\alpha\text{O}$ and $\text{LU}\beta\text{O}$ with α - and β -spins, respectively, and (D) is the spin density map. 119

Figure 5.23 Molecular orbital diagram showing the transition from $\text{Re}^{\text{I}}(\text{bpy}^{\bullet-}\text{-C2-PDI}^{2-})$ to $\text{Re}^0(\text{bpy}^{\bullet-}\text{-C2-PDI}^{\bullet-})$ as determined at the M06/6-31G(d,p)/LANL2DZ level of theory. Loss of axial chloride leads to significant stabilization of relative energy levels. 120

Figure 5.24 Face-on and side-on perspectives of the optimized geometry (A & C) and spin density map (B & D) for the doublet state of $\text{HOOC-Re}^{\text{I}}(\text{bpy-C2-PDI}^{\bullet-})$ as determined at the M06/6-31G(d,p)/LANL2DZ level of theory..... 121

Figure 5.25 Face-on and side-on perspectives of the optimized geometry (A & C) and spin density map (B & D) for the triplet state of $^-\text{OOC-Re}^{\text{I}}(\text{bpy-C2-PDI}^{\bullet-})$ as determined at the M06/6-31G(d,p)/LANL2DZ level of theory..... 122

Figure 5.26 Frontier molecular orbitals of the triplet state of $^-\text{OOC-Re}^{\text{I}}(\text{bpy-C2-PDI}^{\bullet-})$ at the M06/6-31G(d,p)/LANL2DZ level of theory, where (A) represents the HOMO, and (B & C) are the $\text{HO}\alpha\text{O}$ and $\text{LU}\beta\text{O}$ with α - and β -spins, respectively..... 123

Figure 5.27 Molecular orbital diagram showing the transition from $^-\text{OOC-Re}^{\text{I}}(\text{bpy-C2-PDI}^{\bullet-})$ to $\text{HOOC-Re}^{\text{I}}(\text{bpy-C2-PDI}^{\bullet-})$ as determined at the M06/6-31G(d,p)/LANL2DZ level of theory. Addition of proton leads to significant stabilization of relative energy levels. 124

Figure 5.28 Face-on and side-on perspectives of the optimized geometry (A & C) and spin density map (B & D) for the triplet state of HOOC-Re ^I (bpy ^{•-} -C2-PDI ^{•-}) as determined at the M06/6-31G(d,p)/LANL2DZ level of theory.....	125
Figure 5.29 Frontier molecular orbitals of the triplet state of HOOC-Re ^I (bpy ^{•-} -C2-PDI ^{•-}) at the M06/6-31G(d,p)/LANL2DZ level of theory, where (A) represents the HOMO, and (B & C) are the HO α O-1 and HO α O with α -electrons, respectively.....	126
Figure 5.30 Face-on and side-on perspectives of the optimized geometry (A & C) and spin density map (B & D) for the triplet state of OC-Re ^I (bpy ^{•-} -C2-PDI ^{•-}) as determined at the M06/6-31G(d,p)/LANL2DZ level of theory.....	127
Figure 5.31 Frontier molecular orbitals of the triplet state of OC-Re ^I (bpy ^{•-} -C2-PDI ^{•-}) at the M06/6-31G(d,p)/LANL2DZ level of theory, where (A & B) represent the HO α O-1 and HO α O with α -electrons, and (C) is the LU β O with β -spin.....	128
Figure 5.32 Face-on and side-on perspectives of the optimized geometry (A & C) and spin density map (B & D) for the doublet state of OC [•] -Re ⁰ (bpy ^{•-} -C2-PDI ^{•-}) as determined at the M06/6-31G(d,p)/LANL2DZ level of theory.....	129

CHAPTER 1. INTRODUCTION

1.1 Energy outlook, challenges and potential

Over the last century, the world has seen enormous changes in fuel sources, going from firewood for heating and cooking to coal for electricity generation and crude oil for a host of applications. As we look to the future, solar-, wind-, and hydrothermal-generated fuels and electricity offer promise to power buildings, transportation, and more. Advances in the production of materials for daily consumption in food, construction, energy, farming, and computing sectors, to name a few, has had tremendous impact both on society and the environment. At the heart of these changes lies improvements in factors such as efficiency, speed, and scale of manufacturing. These improvements can partly (if not enormously) be credited to the field of materials science and chemistry.

Global energy demand has grown exponentially as population and economies have expanded along with technology. Most of the demand has been met using fossil fuels like coal, oil, and natural gas. However, in recent decades, there has been a growing interest in renewable energy sources, such as biofuels and solar, wind, hydro, and geothermal power with the aim of mitigating the impact of energy production and use on climate change. Some sources like solar and wind are widely available to generate electricity. Although electricity can be used for purposes ranging from lighting to transportation via electric cars, some sectors like aviation and marine travel require higher energy density sources and battery technologies have a long way to go before we can electrify these sectors. Large-scale industries that produce commercial products also face the need for high energy density fuel to power their plants, and the use of solar panels to generate energy would require enormous area of land and consistent supply of the Sun's energy. In the case of

biofuels generated from sources like crops, biowaste, and other organic materials, although the generated fuel can have a higher energy density when compared to solar energy, they are plagued with drawbacks of their own. Some of these include competition with food crops, negative impact on biodiversity and ecosystems, soil degradation, deforestation, and low production efficiency, to name a few. However, biofuels from biowaste like waste oil and other organic matter can overcome some of these drawbacks.

From this discussion, it is clear that green energy generation is a multidimensional problem that needs to be addressed using *targeted* materials and methods. Although there is no *one* renewable energy source that can power every sector, all these sources can benefit certain sectors from a *targeted* approach. In this work, we will discuss three approaches that can achieve net zero carbon emissions.

1.2 Heterogeneous catalysis for biofuel generation

The challenge to produce renewable fuels that mitigate negative impacts of fossil fuel use on the environment is daunting. While electric and hybrid vehicles are beginning to find wide commercial adoption, aviation and marine travel are currently uneconomical to electrify due to the lack of adequate, high-energy density storage.¹ Biofuels from waste and residual feedstocks provide a viable alternative to fossil fuels given, in part, that they provide a lower carbon footprint.¹⁻⁴

Although oxygenated biofuels such as the fatty acid methyl esters (FAME) comprising biodiesel are renewable alternatives to fossil fuels, they suffer from several drawbacks stemming from their high oxygen content.⁵ To improve the engine compatibility

of biofuels derived from renewable oleaginous feedstock, it is important to fully deoxygenate the latter to afford fuel-like hydrocarbons. The three main deoxygenation reactions are hydrodeoxygenation (HDO), which eliminates oxygen in the form of H₂O, decarboxylation (DCX), and decarbonylation (DCN), in which oxygen is eliminated as CO₂ and CO, respectively.⁶⁻⁷ HDO requires large amounts and pressures of H₂ gas, which pose safety, cost, and sustainability challenges since most H₂ is derived from fossil resources.⁸ In contrast, DCX and DCN require much smaller amounts and pressures of H₂ gas, which highlights the importance of developing catalysts favoring these reactions.⁹

Experimental efforts on DCX/DCN have predominately focused on supported Pt¹⁰⁻¹² or Pd^{7, 13-14} catalysts, which show remarkable conversion and selectivity to diesel-like hydrocarbons. In terms of the deoxygenation pathway followed, Lu and co-workers showed that α -carbon dehydrogenation is a likely selectivity descriptor for the deoxygenation of propanoic acid on a Pd[111] surface and that DCN is preferred over DCX.¹⁵ Recent reports on Ni[111] and other transition metal surfaces also suggest that DCX is either unfavorable relative to DCN¹⁶⁻¹⁹ or it is simply DCN followed by water gas shift.^{16, 20} Although Pt- and Pd-based catalysts and their alloys show significant DCX/DCN activity, these precious metals are expensive and subject to deactivation due to coking.²¹⁻²⁴ Less expensive, supported mono- or bi-metallic base metal catalysts containing Ni and Cu can afford high yields of fuel-like hydrocarbons and be resistant to coking.²⁵⁻²⁶ Noteworthy results have been obtained for supported Ni catalysts in general and Ni-containing bimetallic catalysts in particular: For instance, in their work on tristearin deoxygenation, Loe et al. observed 27% conversion and 87% selectivity to C₁₀-C₁₇ alkanes over 20%

Ni/Al₂O₃, the corresponding values being 97% and 99% over 20% Ni-5% Cu/Al₂O₃.²⁵ Experimental evidence indicates that the alkyl chain length has a minimal effect on the rate of fatty acid DCX/DCN,²⁷⁻³⁰ as well as a minimal impact on the adsorption energies of C₁-C₃ carboxylic acids.³¹ This can be attributed to the bidentate adsorption configuration of the carboxylic group, which places the alkyl chain away from – and renders negligible its interaction with – the surface, as reported in both experimental and theoretical studies.³¹⁻³⁴ These studies validate small-chain carboxylic acids like propanoic acid (PAC; CH₃CH₂COOH) as adequate surrogates for fatty acids, particularly given their near-ideal properties as probe molecules for spectroscopic and computational studies. However, recent works on Pd[111],¹⁵ Pt[111],¹⁶ Rh[111],²⁰ and Ni[111]¹⁸ surfaces do not account for the C–COOH internal rotation barrier in PAC,³⁵ this rotation being necessary for the α -carbon hydrogen atoms of PAC to be accessible to the catalyst surface and for the molecule to undergo dehydrogenation. Indeed, the initial state of PAC in these works represents a less stable configuration and requires a less favorable tilted *trans* adsorption mode to undergo dehydroxylation.¹⁵ Recent computational works show that the bidentate binding mode of PAC in which both the C=O and –OH moieties interact with the surface constitute the most stable adsorption mode.³⁶⁻³⁷ These conflicting results present an opportunity to establish the binding mode of PAC and its effect on the DCN reaction mechanism.

1.3 Perovskite solar cells for electricity generation

Perovskites are a class of materials with the general chemical formula ABX_3 , where A is typically an organic or inorganic cation, B is a metal cation, and X is a halide or oxide anion; the original perovskite mineral discovered was CaTiO_3 .³⁸ Perovskites show great potential in solar cell applications with recent chemical and engineering advances leading to perovskite solar cells (PSC) with power conversion efficiency (PCE) greater than 23%, which is comparable to its crystalline silicon counterparts.³⁹⁻⁴² PSC are typically made by depositing a thin film of perovskite onto a substrate, such as glass or plastic. The perovskite layer absorbs sunlight and generates an electric current, which can be collected by electrodes and used as electricity.

The capacity to chemically tune the electronic and optical properties of hybrid organic-inorganic perovskites (HOIP) makes these materials attractive as the active layer in PSC. HOIP can demonstrate large charge-carrier mobilities and optical absorption coefficients while at the same time being tolerant to chemical and structural defects.⁴³⁻⁴⁵ Notably, the large abundance of the starting components coupled with the ability to solution process (i.e., print) HOIP can lead to low-cost materials and PSC production.⁴⁶⁻⁴⁸

The PSC architecture (Figure 1.1) generally consists of an HOIP layer sandwiched between a hole transport layer (HTL) and an electron transport layer (ETL). Following photon absorption and exciton dissociation in the HOIP, holes and electrons (i.e., the charge carriers) transfer across the respective interfaces and are then transported in these layers to electrodes to generate a photocurrent. Charge-carrier recombination in the HOIP bulk and interfaces of materials,⁴⁹⁻⁵³ and interfacial ion mobility,⁵⁴⁻⁵⁵ are known factors for

poor PSC performance metrics or deactivation. Hence, regulating HOIP surface chemistry is an important consideration to increase PCE and stability of the PSC.

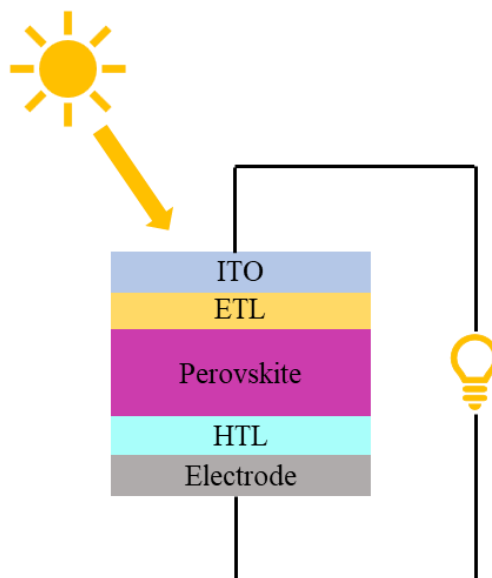


Figure 1.1 A generic architecture of a perovskite solar cell with indium tin oxide (ITO) as the glass substrate, electron transport layer (ETL), perovskite, hole transport layer (HTL) and an electrode.

The idea of surface modification with organic ligands has been explored on several PV materials, including metal oxides and graphene, to alter the work function.⁵⁶⁻⁶⁰ Xia and co-workers⁶¹ demonstrated via experiment and computation that surface defect passivation and hydrophobic effects of FAPbI₃ with 3-(trifluoromethyl) phenethylamine hydroiodide (CF₃PEAI) as the additive. Boehm and co-workers,⁶² through vapor treatment of formamidinium tin-iodide (FASnI₃) perovskite, showed that surface ligands can improve the stability of PSCs. Park et al. demonstrated the penetration of several ligands into the MAPbI₃ thin films and showed unfavorable surface energetics can result in low PV performance.⁶³ Shu and co-workers⁶⁴ showed improved PCE and stability of a Pb-based

6

HOIP upon surface defect passivation with self-assembled phenyltrimethylammonium bromide (PTABr). Other studies have employed the substitution of surface A-cation with organic ligands in metal HPs to improve stability.⁶⁵⁻⁶⁷ For instance, Ravi and co-workers⁶⁷ showed via first-principles calculations that substitution of Cs⁺ ions on CsPbBr₃ perovskite surface by methylammonium (MA⁺) ions is favored over adsorption of MA⁺ on the surface due to minimal energy requirement for surface reconstruction over binding via H-bonding.

From these studies, two main themes can be established where the surface passivation is either via surface adsorption or substitution of surface cations with ligands. Regardless of the surface passivation mechanism, it is well known that organic and polymer-based surface ligands improve the stability of the perovskite structure due to hydrophobic characteristics. However, improvement in the PCE of the cell is not guaranteed for all ligand types^{62-63, 68-69} and more investigation is needed to understand the complex correlation between surface modification and the PV performance.

While many significant improvements in HOIP and subsequent gains in PCE of the PSC have been discovered for lead (Pb)-based HOIP,⁴⁰⁻⁴¹ the presence of Pb comes with toxicity and environmental concerns. Tin (Sn)-based HOIP are seen as an alternative⁷⁰⁻⁷² as they have similar optoelectronic properties when compared to their Pb-based counterparts, though the performance of Sn-based HOIP is substantially lower.⁷³⁻⁷⁴ The deficiency in performance is due in part to the oxidation of Sn²⁺ to Sn⁴⁺ when exposed to air or water, which results in lower PCE.⁷⁵⁻⁷⁶

Several studies have explored the variation of A-cation (either via doping or complete substitution) in the ABX₃ structure of the HOIP to prevent oxidation of Sn²⁺ and

improve stability.^{54, 77-82} Although doping or compositional variations can be effective, the presence of defects can still result in high charge-carrier recombination rates. An alternative approach is to use surface ligands to protect the chemical, structural, and electronic characteristics of HOIP.

To passivate the surface from oxidation, several studies have shown organic ligands as surface modifiers that lower the surface formation energy.^{64, 68-69} In particular, phenylammonium-based ligands are known to be hydrophobic and can self-assemble on the surface by interacting with the perovskite cage through ionic and hydrogen bonds.⁸³⁻⁸⁵ These ligands can also provide π -conjugated mediated charge-carrier transport that can lead to improved PV performance.⁸³⁻⁸⁷ These preliminary analyses call for a thorough understanding of the effect of surface modification on the performance of the perovskite.

1.4 Organometallics for CO₂ conversion

Large industrial processes and the transportation sector are major contributors to greenhouse gas emissions. A prominent component of the greenhouse gas is CO₂. Sequestration of CO₂ in nature occurs via photosynthesis in plants and trees. Simply relying on this phenomenon is not viable since atmospheric CO₂ buildup has aggressively led to climate change. To counter this effect, many engineering and scientific solutions like direct CO₂ air capture and storage in high pressure environments below the sea bed or ocean floor have been explored.⁸⁸⁻⁸⁹ The practicality of these solutions pose enormous challenges like the high cost of CO₂ capture, purification, transportation, and storage⁸⁹ Hence, CO₂

treatment at the source can prove to be a necessary first step to mitigate atmospheric CO₂ buildup and in-turn reduce the risk of climate change.

One way to achieve this is via electrochemical reduction of CO₂ to useful chemicals.⁹⁰⁻⁹¹ The reduction products include carbon monoxide, formate, formic acid, methane, methanol, and more, all of which are precursors for the generation of high energy density fuels that can power air and marine sectors and in addition, close the carbon loop to achieve net zero emissions. In theory, solar radiation provides enough energy to overcome thermodynamic and kinetic barriers for such chemical reactions; but in practice, catalysts are required to enable efficient product delivery.⁹²⁻⁹³ Such electrochemical reduction processes primarily involve the use of organometallic catalysts due to advantages like 1) controllable reaction parameters, 2) recyclable materials, 3) high catalyst selectivity and 4) reduced energy cost for conversion to name a few.⁹³⁻⁹⁴ Organometallic catalysts are a class of catalysts that contain a metal atom or ion bound to one or more organic ligands. These ligands can comprise of alkyls, aryls, cyclopentadienyls, carbonyls, phosphines and more. They are widely used in industrial processes to produce chemicals, polymers, and pharmaceuticals and are ideal for catalytic reactions that involve the activation of small molecules, like carbon dioxide, and in reactions that require high selectivity and control over the reaction conditions.

The earliest known organometallic catalyst for CO₂ reduction is the Wilkinson's catalyst which is a rhodium triphenylphosphine (PhCl(PPh₃)₃) catalyst.⁹⁵ Since then, several other catalysts like ruthenium,⁹⁶⁻⁹⁹ iron,¹⁰⁰⁻¹⁰³ cobalt,^{101, 104-105} nickel,¹⁰⁶⁻¹⁰⁷ and rhenium¹⁰⁸⁻¹¹² based complexes (among others) have been reported. One of the most well-

explored CO₂ reduction catalyst, first introduced by Lehn and co-workers,¹¹³ is based upon Re(2,2'-bipyridine)(CO)₃Cl (henceforth referred to as Re(bpy)). The advantages of Re(bpy)-based catalysts are, they can be tethered to photosensitizers like naphthalimide,¹¹⁴ naphthalene diimide,¹¹⁵⁻¹¹⁷ and perylene diimide (PDI)¹¹⁸⁻¹¹⁹ among others. Of these, PDI is of primary interest in this work since they are ideally suited for photosensitization, possess high molar absorptivity and redox stability, as well as excellent electron-storage capabilities.¹²⁰⁻¹²² In addition, pyrrolic N-atom of the PDI has been explored as a synthetically versatile handle for tuning the physical and optoelectronic properties in organic solar cells and organic field-effect transistors (OFETs).¹²³⁻¹²⁶

To drive the catalytic reaction, an overpotential is needed to overcome the reaction barrier and ideally, if the overpotential is low enough, it could be provided by solar radiation.^{94, 127-131} Since the overpotential is the excess energy needed for by the system to carry out the reaction, catalyst design that lowers the overpotential is highly desirable. To achieve this, Liu and co-workers showed lowering of overpotentials in a Re-based complex by exploiting ligand modifications.¹³² Combining the idea of photosensitizing the Re(bpy) complex and ligand modification to lower the overpotential has been explored before in naphthalimides-based complex but lacks mechanistic details to explain the role of chromophores.¹¹⁴ Using density functional theory (DFT), Liu and co-workers concluded that the energetically favorable dissociation of the axial-chloride from the doubly-reduced catalyst triggers significant changes in the electronic structure of the complex.¹³² It was established that the frontier molecular orbitals (FMO) on the rhenium metal center

reorganize, such that electron-density from the ligand can be accessed by the metal center to enable activation of CO₂, without changing the oxidation state of Re^I.

For the electrochemical reduction of CO₂, a proton mediation coupled with electron-transfer mechanism has been well established with several organometallic catalysts.^{108, 133-138} To study the role of the chromophore, molecular-level understanding is necessary, and computational methods can be an essential tool. For example, Froehlich and Kubiak showed geometric distortions to the complex when a CO is bound to the metal center, to facilitate the CO₂ reduction.¹³⁹ In particular, they showed Ni carbonyls stabilize the five-coordinate active complex due to back-bonding interactions which is necessary for reduction mechanisms. Using computational methods, Benson and co-workers also showed delocalized electron density on the Re(bpy) moiety of their catalyst to be responsible for a proton-coupled electron mediated reduction on CO₂.¹⁴⁰ In addition, Manbeck and co-workers¹⁴¹ studied CO₂ reduction mechanisms in single- and doubly-reduced Re-based complex without a chromophore and found both to be favorable without much distinction, suggesting the presence of a chromophore could assist one of these mechanisms through a more feasible electron transfer mechanism. These findings warrant a comprehensive computational understanding of the effect of a chromophore such as PDI, on the lowering of electrocatalytic reduction overpotential of CO₂. Understanding the role of the chromophore through computation can lead to efficient design of organometallic catalysts for electrochemical CO₂ reduction.

1.5 Objectives and outline of the dissertation

From the outlook and challenges set forth in this chapter, a multi-dimensional approach involving *targeted* materials development, focused on individual sectors, that supports mitigation of climate change is necessary. The overarching hypothesis of this dissertation is that *critical understanding of surface and molecular geometry of functionalized materials from first principles can be used to tune the performance parameters for green energy generation.*

The necessary knowledge to develop an understanding of the methods employed in this dissertation to achieve the objectives and test the hypothesis is provided in Chapter 2. An overview of the electronic structure theory along with quantum mechanical descriptions is provided. The assumptions, clarifications, and approaches to these methods are also presented. In addition, brief description of key concepts encountered in this study are also explained to develop a comprehensive understanding necessary to assimilate the results of this work.

Chapter 3 discusses the results of mechanistic studies involving the DCN reaction mechanism of PAc on a Ni[111] surface. Specifically, DFT calculations are utilized to study the adsorption mode of PAc on the surface. The results from this work are discussed in comparison with previously established work and new findings are presented. From the preferred adsorption mode, the reaction mechanism is elucidated with thermodynamic and kinetic studies. The role of the adsorption mode in the direction of the mechanism is established and a theoretical analysis is presented. In developing the reaction mechanism, a mean-field microkinetic model is developed considering experimental reaction conditions.

The model is then refined based on initial results to obtain a more realistic understanding of the most dominant reaction pathway. The theoretical analysis presented is compared with the model predicted values and experimental results where applicable. An overarching conclusion is established where the PAc adsorbs on the surface in a bidentate fashion and this mode prevents the α -carbon dehydrogenation of PAc as the first step but instead, PAc undergoes dehydroxylation in the first step. This results in a lower apparent activation barrier when compared to previous results and very similar to previously established experimental results that also identified the same rate determining step as verified by this study. These conclusions highlight and reiterate the importance of surface geometry in heterogeneous catalysis.

The impact of fluorination of surface ligands on a perovskite surface is studied in Chapter 4. DFT calculations are employed to explore ligands that are known to passivate the oxidation of the Sn^{2+} to Sn^{4+} in the perovskite structure. The bulk properties of the FASnI_3 perovskites is determined and surfaces are constructed with self-assembled monolayer (SAM) of each of the proposed ligands. The effect of fluorination of the phenyl ring of the anilinium (An) ligands on properties like surface energy, binding energy and work function is studied. Surface electronic properties like charge density difference plots were constructed. A correlation was established between the ligand dipole moment and the vacuum potential and Fermi energy of the corresponding surface. However, it was established that the change in the ligand dipole moment had minimal effect on the work function of the surface. The phenyl ring of An was substituted with bulkier halogens to study its effect on the work function which resulted in minimal change of the property.

Understanding this behavior can lead to effective design of the perovskite surface to tune the work function and control the surface electronic properties.

In Chapter 5, the role of the PDI chromophore as an electron reservoir for electrochemical CO₂ reduction reaction is established using DFT calculations. The results from this work align with the proposed reaction mechanism based on experiments. It is observed that a geometric unfolding of the organometallic complex Re(bpy-C2-PDI) aids the transfer of electrons from the PDI chromophore to the catalytically active metal center. This photon-coupled electron-mediated CO₂ reduction pathways is responsible for the lowering of the reaction overpotential. To further understand the reaction mechanism, frontier molecular orbitals (FMO) and electronic spin densities were examined for each intermediate, which showed the formation of a well-known, stable five-coordinate Re(bpy) complex that is responsible for the electrochemical reduction of CO₂. Back-bonding interactions between the Re-atom and the carbonyl was identified to stabilize the catalytically active five-coordinated complex. In addition to back-bonding, an electron transfer is observed from a highly energetic orbital localized on the PDI to the Re(bpy) moiety of the complex and, this electron transfer preserves the oxidation state of the metal center making it the active site for CO₂ reduction. Conclusions from this study allows the development of chromophore assisted organometallic complexes with low overpotential for electrochemical or photochemical CO₂ reduction.

Chapter 6 provides a synopsis of this dissertation with emphasis on key findings presented in this work. The hypothesis is revisited and a discussion on broader implications based on the work presented in this dissertation is presented. Future directions to bridge

the knowledge gap and explore new methods to study promising chemical spaces is provided.

CHAPTER 2. METHODS

In this section, we present a brief introduction to density functional theory (DFT), which is the core computational approach used in this work. Note, this work does not present an improvement over the methods presented, rather we test, validate, and make use of DFT approaches to study chemical processes and materials properties for the questions outlined in Chapter 1. The two main books used in the following to summarize DFT were “Computational Materials Science – An Introduction”, by June Gunn Lee¹⁴² and “Density Functional Theory – A Practical Introduction”, by David S. Sholl and Janice A. Steckel.¹⁴³ This Chapter also provides descriptions of the nudged elastic band and dimer methods, microkinetic modeling, surface and absorption energies, and spin densities, each which feature throughout the remaining Chapters.

2.1 Density functional theory (DFT)

In the early twentieth century, Niels Bohr proposed the quantum nature of electrons wherein an electron circulates around a nucleus in specific ‘orbitals’ in which it does not radiate energy and that they possess a specific energy that are allowed for a particular orbital. Bohr also proposed that these electrons can jump up or down from one energy level to the other upon absorption or emission of specific ‘quanta’ of energies, respectively. Prior to Bohr, in 1900, Max Planck reported the non-continuous radiation of a blackbody which was due to the loss of energies in quanta, that is, $E = nh\nu$, where n is an integer, ν is the frequency of the radiation and h is the Planck’s constant. Louis de Broglie in 1924 established the dual nature of electrons where he said the momentum of a particle is

inversely proportional to the wavelength of the particle and the frequency is directly proportional to the kinetic energy of that particle. Then, in 1926, Erwin Schrödinger derived the wave equation:

$$\left[\frac{\hbar^2}{2m} \sum_{i=1}^N \nabla_i^2 + \sum_{i=1}^N V(r_i) + \sum_{i=1}^N \sum_{j<i}^N U(r_i, r_j) \right] \psi = E\psi \quad (2.1)$$

where, m is the electron mass, the three terms in the brackets are the kinetic energy of each electron, the interaction energy between each electron and the collection of atomic nuclei, and the interaction energy between different electrons, respectively. The wavefunction ψ , represents the spatial coordinates of each of the N electrons in the system. So, $\psi = \psi(r_1, \dots, r_N)$, and E is the ground-state energy of the system of electrons.[†] Although the ψ_N values are complex numbers, E (eigen value) is always a real number. This description of Schrödinger equation is time independent and is called as the time-independent Schrödinger equation. The wavefunction ψ can be further approximated as $\psi = \psi_1(r)\psi_2(r) \dots \psi_N(r)$, which is the product of N number of single electron wavefunctions, also known as the Hartree product, which simplifies the Schrödinger wave equation further. We note, however, that this is now a ‘many-body’ problem.

The fundamental problem in quantum mechanics is to solve the equation (2.1), but it is important to realize that the wavefunction cannot be observed directly for any given set of coordinates. However, for physical significance, the probability of a set of N

[†] Electron spin is neglected for simplicity; in a more complete sense, each electron is defined by the spatial coordinates and its spin state.

electrons in any order having coordinates r_1, \dots, r_N is of interest. This can be written in terms of the individual electron wavefunctions as the density of electrons at a particular position in space, $\rho(r)$,

$$\rho(r) = 2 \sum_i \psi_i^*(r) \psi_i(r) \quad (2.2)$$

Here, the * indicates the complex conjugate of the wavefunction. The summation is for all the electrons described by its individual wavefunctions and the term in the summation is the probability of the electron in the individual wavefunction $\psi_i(r)$ located at position r . The factor of two is a result of the Pauli exclusion principle that states that the individual electron wavefunction can be occupied by two separate electrons with different spin. Note that the electron density is a function of three coordinates, while the Schrödinger equation (2.1) is a function of $3N$ coordinates. This quantity, as opposed to the full Schrödinger equation (2.1), is physically observable and has a great amount of information.

2.1.1 Wave functions to electron density

The fundamental theorems of DFT were established by Kohn, Hohenberg and Sham in the mid-1960s. Theorem 1 by Kohn and Hohenberg states that the ground-state energy from Schrödinger's equation is a unique functional of the electron density. In simple terms, a functional is a function of a function. A function is dependent on a set of variables and a functional is dependent on a set of functions described by a set of variables. For example,

$$F[f] = \int_0^1 f(x) dx \quad (2.3)$$

where, $F[f]$ is a function of a function $f(x)$. Here, the ground state energy can be expressed in terms of the electron density as $E[n(r)]$. An important result of this theorem is that from the ground state electron density, one can uniquely determine all properties including the wave function and the energy of the ground state using just three dimensions instead of $3N$ dimensions. However, this theorem only shows that a functional exists, falling short of defining the actual functional itself. The concept of ground-state energy takes it further in the sense that an atom or a set of atoms/molecules have a minimum energy and the electron density at this state is the true ground state electron density corresponding to the full solution of the Schrödinger's wave equation. This is a function of the variational principle, which outlines the procedure to find the relevant electron density that minimizes the energy functional, if the 'true' form of the functional is known.

The energy functional, as described by the Hohenberg-Kohn theorem, can be written in terms of the single-electron wave functions as

$$E[\{\psi_i\}] = E_{known}[\{\psi_i\}] + E_{XC}[\{\psi_i\}] \quad (2.4)$$

Note that the electron density is collectively described by equation (2.4), where the functional is split into the $E_{known}[\{\psi_i\}]$ and everything else in the $E_{XC}[\{\psi_i\}]$ term. The $E_{known}[\{\psi_i\}]$ term includes contributions from the kinetic energies of the electrons, the interactions between the electrons and the nuclei, the coulombic interactions between

electron pairs, and the coulombic interactions between pairs of nuclei. These terms can be generalized as

$$\begin{aligned}
 E_{known}[\{\psi_i\}] = & \frac{\hbar^2}{m} \sum_i \int \psi_i^* \nabla^2 \psi_i d^3r + \int V(r) \rho(r) d^3r \\
 & + \frac{e^2}{2} \int \int \frac{\rho(r) \rho(r')}{|r - r'|} d^3r \cdot d^3r' + E_{ion}
 \end{aligned} \tag{2.5}$$

The exchange-correlation functional, $E_{XC}[\{\psi_i\}]$, is set to include the quantum mechanical effects that cannot be observed and are not part of the ‘known’ term. $E_{XC}[\{\psi_i\}]$ can be described as a correction term to the energy functional. For example, the coulombic interaction term between pairs of electrons includes the self-interaction energy of an electron with itself. It makes sense to add a correction term to mitigate the self-interaction of the electron in the total energy functional.

To solve the equation (2.5) and find the right electron density, Kohn and Sham expressed a method in which a set of equations can be solved where each equation involves only a single electron. The Kohn-Sham equations are of the form

$$\left[\frac{\hbar^2}{2m} \nabla^2 + V(r) + V_H(r) + V_{XC}(r) \right] \psi_i(r) = \epsilon_i \psi_i(r) \tag{2.6}$$

This is similar to the full Schrödinger equation (2.1) with the exception that it does not include the summations since equation (2.6) depends on a single electron’s spatial coordinates, $\psi_i(r)$. The first term is the kinetic energy term of the electrons followed by three potential energy terms. The first term $V(r)$ is the ‘known’ part of the total energy

functional, which defines the interaction between the electrons and the atomic nuclei. The second potential term is the Hartree potential,

$$V_H(r) = e^2 \int \frac{\rho(r')}{|r - r'|} d^3r' \quad (2.7)$$

which describes the repulsive coulombic interaction of each electron of concern with the mean electron field comprising of all the electrons including the electron of concern represented by the Kohn-Sham equation (2.6). By definition, this term includes the self-interaction energy of the electron of concern. Note that the mean electron field is represented by the total electron density. This self-interaction is unphysical and must be corrected for by the exchange and correlation term, $V_{xc}(r)$. This term, grouped with other quantum mechanical effects (more on this later) can be represented as,

$$V_{xc}(r) = \frac{\delta E_{xc}(r)}{\delta \rho(r)} \quad (2.8)$$

Note that the functional derivative is not the same as the regular derivative in the sense that it is with respect to a function and not a variable. The problem now becomes an iterative one where, to solve the Kohn-Sham equations, we need to know the Hartree potential, and to define $V_H(r)$, we need to know the electron density, $\rho(r)$. But to determine the $\rho(r)$, we need to know the solution to the single-electron wave functions, and to know this, we must solve the Kohn-Sham equations. To solve this iterative problem and obtain the ground state electron density, we employ the following:

1. Define a trial electron density, $\rho(r)$.

2. Find the single-electron wave functions by solving the Kohn-Sham equations defined by $\rho(r)$.
3. Calculate the new electron density from the Kohn-Sham single-electron wave functions obtained from step 2, $\rho_{KS}(r) = 2 \sum_i \psi_i^*(r)\psi_i(r)$.
4. Compare the initial electron density with $\rho_{KS}(r)$ and if they are the same, then this is the ground state electron density, which can be used to calculate the total energy of the system. If they are not the same, the electron density must be updated in some way and the procedure must resume from step 2.

Although many important details are captured, answers to the questions ‘How similar should the electron densities be before concluding that they are the same? How should the trial electron density be updated? How do we define the initial density?’, are missing; The steps entailed here is known as the self-consistency approach.

2.1.2 Exchange-correlation functional:

As mentioned earlier, the exchange-correlation functional involves the ‘unphysical’ interactions. These account for the self-interaction of an electron with itself in the mean electron field, the neglected interacting kinetic energy, and the exchange energy as a result of two electrons with identical spins occupying the same orbital, which goes against the Pauli’s exclusion principle. The exchange-correlation functional cannot be determined exactly and needs to be approximated. Approximation methods are broadly classified into two methods, the Local Density Approximation (LDA) and the Generalized Gradient

Approximation (GGA). Although other methods exist, for the purpose of this work, LDA and GGA will suffice.

$E_{XC}[\{\psi_i\}]$ can be determined exactly for the case of a uniform electron gas. Although it is not a realistic system, the results are very important to understand the exchange-correlation functional. This approach considers a constant electron density across all points in space. The exchange-correlation potential can then be written as

$$V_{XC}(r) = V_{XC}^{electron\ gas}[\rho(r)] \quad (2.9)$$

This is referred to as LDA since it uses only the local $\rho(r)$ to approximate the E_{XC} and now allows us to completely define the Kohn-Sham equations. However, this is not the true form of the E_{XC} functional and as a result does not solve the true Schrödinger equation (2.1).

The GGA functional, on the other hand, uses the information from the local electron density and the gradient in electron density to provide a more accurate description of the functional. Though, this may not be the case always. There are many different GGA functionals of which, Perdew-Wang functional (PW-91)¹⁴⁴ and the Perdew-Burke-Ernzerhof functional (PBE)¹⁴⁵ are common. These functionals in general provide more accurate representation of the electron density by including density gradient as an additional parameter. The general form of the GGA functional can be expressed as

$$E_{XC}^{GGA}[\rho(r)] = \int \rho(r) \epsilon_{XC}^{GGA}[\rho(r), \Delta\rho(r)] dr \quad (2.10)$$

where $\Delta\rho(r)$ is the electron density gradient and ϵ_{XC}^{GGA} is a function of the local electron density and the electron density gradient per electron. The exchange-correlation potential can now be written as,

$$V_{XC}^{GGA}[\rho(r)] = \frac{\delta E_{XC}^{GGA}}{\delta\rho(r)} = \rho(r) \frac{d\epsilon_{XC}^{GGA}[\rho(r)]}{d\rho(r)} + \epsilon_{XC}^{GGA}[\rho(r)] \quad (2.11)$$

A more appropriate form of the exchange-correlation energy integral would include the spin variable as,

$$E_{XC}^{GGA}[\rho \uparrow, \rho \downarrow] = \int \rho(r) \epsilon_{XC}^{GGA}[\rho \uparrow, \rho \downarrow, \Delta\rho \uparrow, \Delta\rho \downarrow] dr \quad (2.12)$$

It should be noted that there is no simple form of the GGA functional that would describe the GGA data correctly and, hence, the $E_{XC}^{GGA}[\rho(r)]$ needs to be expressed in an form and fit to satisfy various physical constraints. It is easier in practice to express the general form of GGA based on the LDA and an additional enhancement factor $F(s)$ that modifies the LDA energy directly,

$$E_{XC}^{GGA}[\rho(r), s] = \int \epsilon_{XC}^{LDA}[\rho(r)] \rho(r) F(s) dr \quad (2.13)$$

where, the s depends on both the electron density and its gradient,

$$s = C \frac{|\Delta\rho(r)|}{\rho^{\frac{4}{3}}(r)} \quad (2.14)$$

In the following work, we employed the PBE functional within the GGA since it is the most widely used functional for the transition metal systems under study and is an improvement over PW91, which is known to produce spurious wiggles in the exchange-

correlation potential at both low and high electron density. The PBE functional is expressed as¹⁴⁵

$$E_{XC}^{GGA/PBE}[\rho \uparrow, \rho \downarrow] = \int d^3r \rho \epsilon_X^{unif}(\rho) F_{XC}(r_s, \zeta, s) \quad (2.15)$$

When ζ is independent of r , this equation represents any GGA exactly and is always approximately valid. At the high-density limit, the exchange turns on more and the correlation turns off. Conversely, the correlation dominates the exchange at the low-density limit.

2.1.3 Periodic DFT

To understand the concepts of periodic DFT, we first need to recap the idea of a periodic/Bravais lattice and the fundamentals thereof. A periodic crystal lattice is a system of infinite points periodically repeated in space. A primitive lattice vector is a vector from one lattice point to the nearest lattice point. Each point is positioned at a lattice vector \vec{R} , which is a linear combination of primitive lattice vectors \vec{a}_1 and \vec{a}_2 with integer coefficients n_1 and n_2 .

$$\vec{R} = n_1 \vec{a}_1 + n_2 \vec{a}_2 \quad (2.16)$$

A unit cell of a crystal is the smallest repeating unit of the crystal lattice. Reciprocal lattice on the other hand describes the points of constructive interference in the diffraction pattern of a crystal lattice. It is called so because these points are reciprocally/inversely related to the lattice points in real space. The length of the unit cell in reciprocal lattice is

$2\pi/L$, where L is the length of a unit cell in real space. The reciprocal lattice vectors follow the property of ortho-normality:

$$\vec{a}_i \cdot \vec{b}_j = 2\pi\delta_{ij} \quad (2.17)$$

where, \vec{a}_i is the primitive translation vector and \vec{b}_j is the primitive reciprocal lattice vector. If V is the volume of the unit cell in real space, the volume in reciprocal space (or k-space) is $2\pi/V$. Following these properties, in simple terms, we can now define the *Brillouin zone* as the most symmetric unit cell of the reciprocal lattice. In other words, it is the uniquely defined primitive cell in the reciprocal space. The 1st Brillouin zone (BZ) is the primitive cell in reciprocal space that is closer to the origin of the reciprocal lattice point (Γ -point) than any other reciprocal lattice points. It comprises of a set of points called the k-points in k-space that can be reached (by k-vectors) from the Γ -point without crossing the Bragg planes. When this zone is reduced by all symmetries in the point group of the lattice, it is called the Irreducible Brillouin zone (IBZ). This leads to the Bloch Theorem, which describes the periodicity of wavefunctions obtained from the solution of the Schrödinger wave equation and the implications of thereof in periodic DFT. Bloch theorem can be written as

$$\psi_k(r) = e^{ikr} u_k(r) \quad (2.18)$$

where $\psi_k(r)$ is the single particle wavefunction at a point ' r ' in k-space described by the k-vector for any periodic potential $V(r)$ and $u_k(r)$ is any arbitrary function that satisfies the above equation. This arbitrary function satisfies the periodicity,

$$u_k(r + T) = u_k(r) \quad (2.19)$$

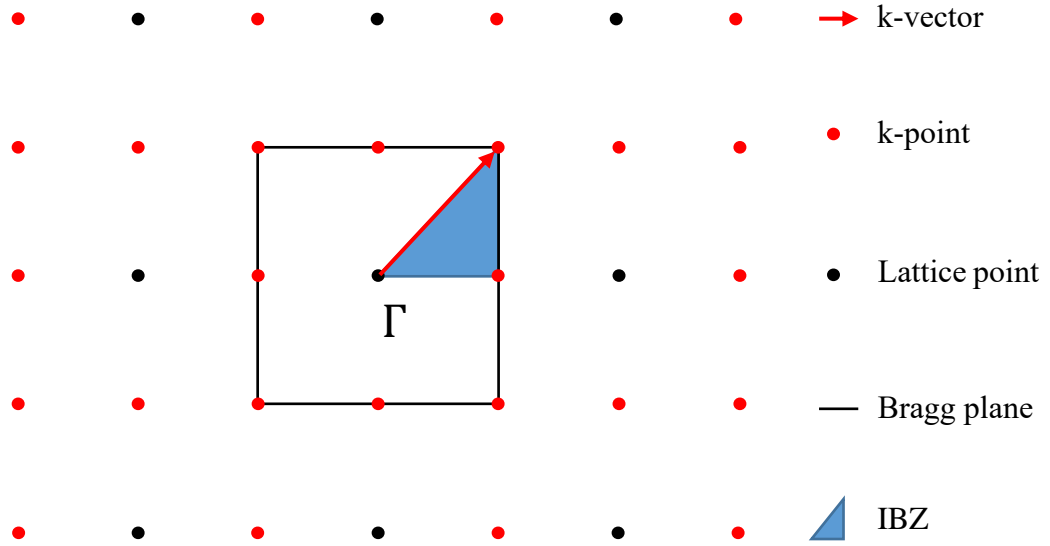


Figure 2.1 Periodic reciprocal lattice describing the Irreducible Brillouin Zone (IBZ).

implying that any function $\psi_k(r)$ that is a solution to the Schrödinger wave equation differs only by a phase factor e^{ikT} between equivalent positions in the lattice. This would also imply that the probability of finding an electron is same at any equivalent position in the lattice. It should be noted that molecular DFT would simply be a case where $k = T = 0$, where solving Kohn-Sham equations for N -electron system would suffice. In the periodic case, for all k and T , $|e^{ikT}|^2 = 1$. This implies

$$|\psi_k(r + T)|^2 = |\psi_k(r)|^2 \quad (2.20)$$

If $\psi_k(k)$ is a solution to the Schrödinger wave equation, the corresponding eigen value is $E(k)$ and since this wave function is identical to $\psi_k(k + T)$, we can say,

$$E(k + T) = E(k) \quad (2.21)$$

This is an important implication of the Bloch theorem where any reciprocal lattice point can be the origin of the $E(k)$ function and within each periodic space (from 0 to k), we can describe a set of wavefunctions that contains all possible energies of the system. From this inference, we can say that the 1st Brillouin zone contains all possible energies of the system and solving the Kohn-Sham equations for particles within this zone will be enough to obtain all possible properties of the system.

2.1.4 Pseudopotentials

In large systems with many electrons, the number of plane waves necessary is large and makes the calculations extremely costly. The core electrons of an atom are associated with plane waves that oscillate on short length scales in real space, which require a large *cutoff energy*. But these core electrons are hardly involved in chemical bonding and the physical properties of a material. As a result, if these plane waves are approximated to the properties of core electrons, the number of plane waves necessary for calculation is greatly reduced. Pseudopotentials do exactly this by replacing the core electron density with a smooth density that matches the physical properties of the core electrons. This approximation can be applied to all atoms involved in a DFT calculation and it is called as the frozen core approximation. These properties are transferable in the sense that a pseudopotential can be developed via an all-electron calculation of an isolated atom and can be used in calculations involving this atom in any chemical environment.

This work involves the use of projector augmented-wave (PAW) method introduced by Blochl and adopted by Kresse and Joubert in plane-wave calculations. Their

method shows the results from the PAW method agrees well with the all-electron calculations for small molecules and extended solids.¹⁴⁶

2.2 Nudged elastic band and dimer method

The following work employs the climbing image nudged elastic band (cNEB)¹⁴⁷ calculations along with the dimer method¹⁴⁸ to predict transition states (TS) and the minimum energy pathway (MEP) between the initial and final states of elementary steps. This method was presented by Henkelman and co-workers¹⁴⁷⁻¹⁴⁹ and this section briefly explains the theory behind cNEB and dimer calculations.

In addition to the Born-Oppenheimer approximation, transition state theory (TST) builds on two basic assumptions: (a) the Boltzmann distribution for the reactant can be established if the rate is slow, (b) the reaction trajectory crosses a dividing surface only once going from initial state to the final state. This surface acts as a bottleneck to the transition under consideration. In crystal structures, atoms are closely packed and the temperature for a reaction is far lower than the melting point of the crystal, and as a result we can apply the harmonic approximation to TST. This enables the search for a few saddle points near the edge of the potential energy basin of the initial state. From the energy and frequencies of normal modes at the saddle point and the initial state, we can determine the rate constant for transition across the saddle point using

$$k_{hTST} = \frac{\prod_i^{3N} \nu_i^{init}}{\prod_i^{3N-1} \nu_i^{SP}} e^{-(E^{SP} - E^{init})/k_B T} \quad (2.22)$$

where ν_i^{init} and ν_i^{SP} are the vibrational frequencies of the initial state and the saddle point for the i^{th} vibrational mode and E^{SP} and E^{init} are the energies of the saddle point and the initial state respectively. The MEP is the pathway between the initial and final state with the highest statistical probability. The force acting on any atoms along this path is always along this path. Along the perpendicular degree of freedom (DOF), the energy is stationary. The saddle point is the maxima of the MEP and the reaction coordinate from this point is determined by normal mode eigenvector with negative curvature. The highest saddle point determines the rate of the elementary step.

To begin, a set of $(N - 1)$ intermediate images between the initial and final state is created. To ensure the continuity of the path, a spring force is added between adjacent images, which mimics an elastic band. A force optimizer minimizes the forces on the band without the spring force interfering with the optimization. The total force acting on an image on this band is broken into two components: (a) the spring force along the tangent to the path and (b) the true force perpendicular to the path. This force projection is called the nudging of the band. If the spring force is not considered, the images would converge to the local minimum (initial/final state).

Consider an elastic band with $(N + 1)$ images and their coordinates, (R_0, R_1, \dots, R_N) with R_0 and R_N being the coordinates of the first and the final images respectively which will remain fixed throughout the calculation. The tangential force is the total force acting on an image and is the sum of spring force along the local tangent and the true force perpendicular to the local tangent

$$F_i = F_i^S \Big|_{\parallel} - \nabla E(R_i) \Big|_{\perp} \quad (2.23)$$

where the true force is given by

$$\nabla E(R_i) \Big|_{\perp} = \nabla E(R_i) - \nabla E(R_i) \cdot \hat{t}_i \quad (2.24)$$

where E is the energy of the system, and \hat{t}_i is the normalized local tangent at image i . The spring force is

$$F_i^S \Big|_{\parallel} = k(|R_{i+1} - R_i| - |R_i - R_{i-1}|)\hat{t}_i \quad (2.25)$$

where k is the spring constant. The images are converged on the MEP using a projected velocity Verlet Algorithm.¹⁵⁰ A drawback of this method is that the saddle point would need to be determined based on interpolation since none of the images will converge on the maxima due to the presence of a constant spring force between all images. Hence, we employ the cNEB method. In cNEB, the MEP is retained and convergence to a saddle point is achieved without much added computational cost. It begins with a regular NEB to identify the image with the highest energy, i_{max} . The tangential force on this image is given by

$$F_{i_{max}} = -\nabla E(R_{i_{max}}) + 2\nabla E(R_{i_{max}}) \Big|_{\parallel} \quad (2.26)$$

$$F_{i_{max}} = -\nabla E(R_{i_{max}}) + 2\nabla E(R_{i_{max}}) \cdot \hat{t}_{i_{max}} \hat{t}_{i_{max}} \quad (2.27)$$

This is the total force due to the potential with the spring forces inverted. In other words, this image does not depend on the spring forces and moves up the elastic band and down

the potential energy surface perpendicular to the band. The other images define the DOF along which energy is maximized to push the i_{max} image to the saddle point.

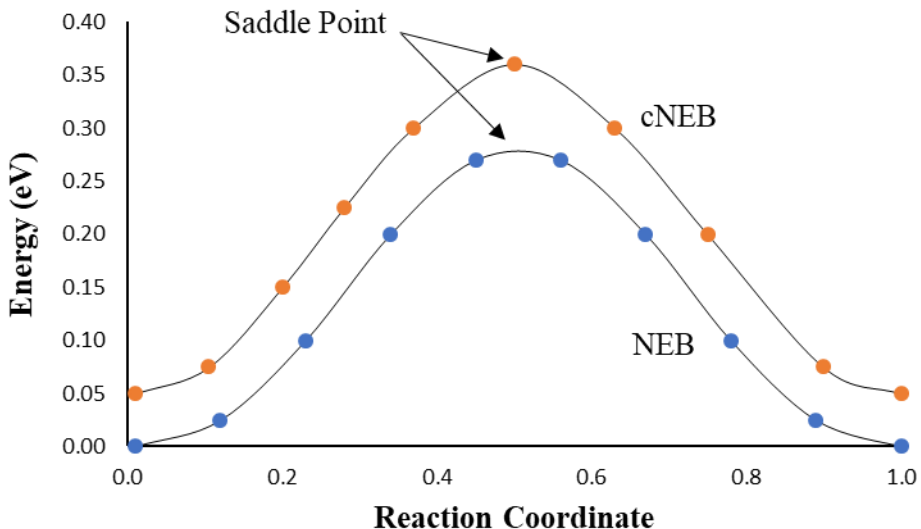


Figure 2.2 A comparison between NEB and cNEB showing an image at the saddle point of the cNEB calculation.

2.2.1 Dimer method

The dimer method¹⁴⁸ is used in combination with the NEB method to speed up the search for a saddle point. This method involves the use of two ‘replica’ images called the ‘dimer’. A system with ‘ n ’ atoms described by $3n$ set of coordinates will have two replicas with almost the same set of coordinates except that, they are displaced by a fixed distance. The search algorithm is designed to move the dimer up the potential energy surface towards the saddle point. The dimer is rotated as it is moved up towards a saddle point to find the lowest curvature mode of the potential energy at that point. To illustrate this, consider a simple curve $y = f(x)$ with an arc MM_1 with the two points displaced by δs . Now consider

a tangent at the two points of the arc which make an angle α and $\alpha + \delta\alpha$ with the x-axis. The mean curvature of this arc is given by, $\frac{\delta\alpha}{\delta s}$. As $\delta s \rightarrow 0$, we obtain the curvature of the curve at point M . The ‘guess’ image for the saddle point is obtained from the cNEB calculations when the forces on all images are below 0.5 eV/Å. The dimer images are produced using this guess at the common midpoint R and the dimers displaced by ΔR . A unit vector \hat{N} is chosen along the direction from one image R_2 to the second dimer R_1 and the corresponding coordinates of the dimer images can be written as

$$R_1 = R + \Delta R \hat{N} \quad (2.28)$$

$$\text{and } R_2 = R - \Delta R \hat{N} \quad (2.29)$$

Every time the dimer is moved, the forces acting on the dimer and the energy of the dimer is evaluated. A total energy of the dimer E will be the sum of the energies of the two dimers,

$$E = E_1 + E_2 \quad (2.30)$$

The energy and the forces acting on the midpoint of the dimer is calculated by interpolation between the two images as, F_R and E_0 respectively. The force at the midpoint is the average force,

$$F_R = \frac{(F_1 + F_2)}{2} \quad (2.31)$$

and a relation between the curvature and E_0 can be derived from the finite difference formula as,

$$C = \frac{(F_2 - F_1) \cdot \hat{N}}{2\Delta R} = \frac{E - 2E_0}{(\Delta R)^2} \quad (2.32)$$

E_0 can be evaluated from the known forces on the dimer images as,

$$E_0 = \frac{E}{2} + \frac{\Delta R}{4} (F_1 - F_2) \cdot \hat{N} \quad (2.33)$$

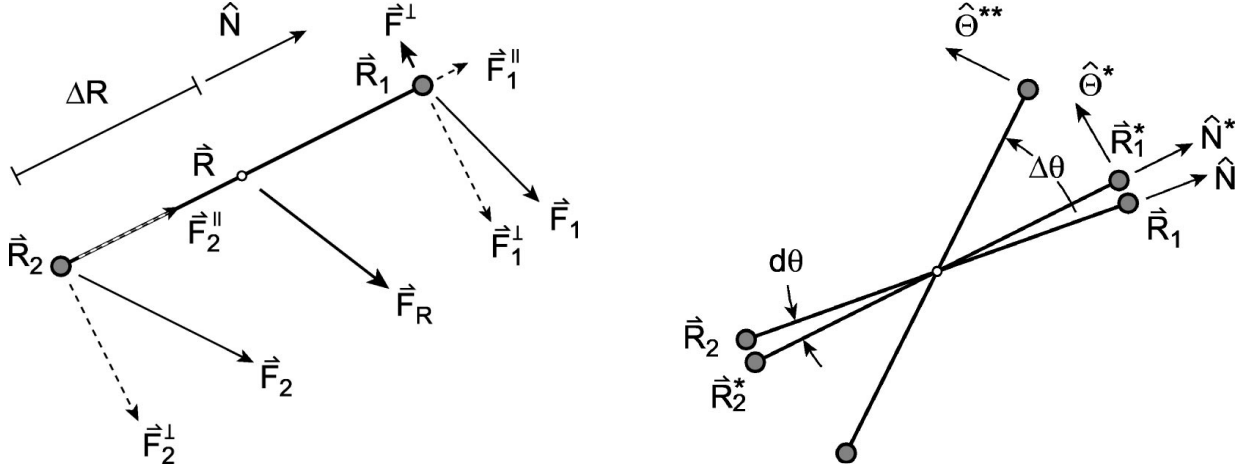


Figure 2.3 Definition of various position, force and rotational vectors. All rotational vectors are in the plane of rotation. Image taken from Henkelman and co-workers.¹⁴⁸

Note that the energy and forces at the midpoint need not be evaluated through computation and can be determined from the dimers, thus saving computational effort.

The dimer is rotated with every iteration towards the minimum energy configuration keeping the midpoint at R stationary. Since the energy of the dimer, E , and the curvature, C , are linearly dependent, a search for the low curvature mode is equivalent to minimizing the energy of the dimer. This greatly simplifies the search algorithm and improves efficiency. The rotation $\Delta\theta$ needed to reduce the force on the dimer can be determined from Newton's method

$$\Delta\theta \approx \frac{(F \cdot \hat{\Theta} + F^* \cdot \hat{\Theta}^*)}{-2F'} \quad (2.34)$$

where $F' = dF/d\theta$ is the change in the rotational force as the dimer rotates by $d\theta$. The search direction can be determined based on several known algorithms like the conjugate gradient algorithm employed in this study.

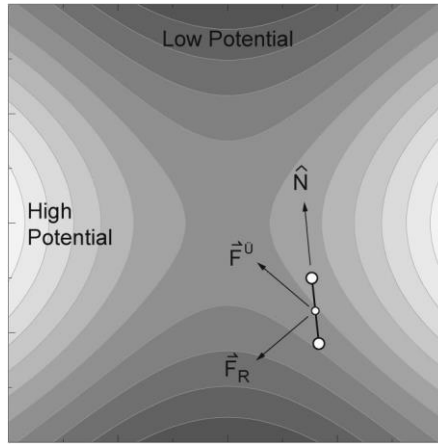


Figure 2.4 Movement of the dimer towards the saddle point as a result of the effective force acting at the center of the dimer taken from Henkelman and co-workers.¹⁴⁸

The translation of the dimer is much simpler where a modified force is employed with the force component along the dimer is inverted

$$F\ddot{U} = F_R - 2F^{\parallel} \quad (2.35)$$

This inversion is key to move the dimer towards the saddle point since the net translational force, F_R pulls the dimer to a minimum. Algorithms like the conjugate gradient algorithm can be employed for the translational search direction.

2.3 Microkinetic modeling

This section is derived from “Introduction to Microkinetic Modeling” by I. A.W. Filot.¹⁵¹ Before discussing the principles of microkinetic models (MKM), it is important to understand the basic concepts involved in reaction kinetics.

2.3.1 Rate of a reaction

Every chemical reaction can be broken down into a series of elementary reactions where each elementary reaction represents or accounts for only one bond breaking or bond formation. Consider an elementary reaction step between molecules A and B that give products C and D according to the following reaction equation,



where v_i is the stoichiometric coefficient of reactant or product i . Let k^+ be the rate constant of the forward reaction and k^- be the rate constant of the reverse reaction. The rate of this reaction can be defined as the rate of disappearance of a reactant or the rate of formation of a product. Namely,

$$r = -\frac{1}{v_a} \frac{d[A]}{dt} = -\frac{1}{v_b} \frac{d[B]}{dt} = \frac{1}{v_c} \frac{d[C]}{dt} = \frac{1}{v_d} \frac{d[D]}{dt} \quad (2.37)$$

where, $[X]$ is the concentration of a component in the reaction as a function of time t , and r is the reaction rate. Note that equation (2.37) can only be written for an elementary reaction. Hence, for a sequential set of elementary reactions, we can write the general rate expression as,

$$\frac{d[X]}{dt} = \sum_j \left(v_{x,j} \left(k^+ \prod_{v_i < 0} [X_i]^{v_i} - k^- \prod_{v_i > 0} [X_i]^{v_i} \right) \right) \quad (2.38)$$

where j represents all elementary steps in which component X takes part in the reaction. As such, summation over j would entail the formation or disappearance of the component X in the overall reaction mechanism. In Chapter 3, this component is referred as the surface intermediate and equation (2.38) will be described as the surface concentration of intermediate X .

2.3.2 Steady state approximation

Equation (2.38) is an ordinary differential equation (ODE) and to solve a system of ODEs, analytical approaches are usually the norm. However, solving a system of ODEs for a complex network of elementary reactions is not warranted. Instead, a valid assumption is made where the system of ODEs can be transformed to a system of differential algebraic equations (DAEs). The steady state approximation assumes that the rate of change of one of the intermediates is zero. This implies that the intermediate to which the approximation is applied to is highly reactive. So, if X is a highly reactive intermediate, we can say

$$\frac{d[X]}{dt} = 0 \quad (2.39)$$

This assumption allows us to solve the set of DAEs analytically and numerically. The numerical approach to the solution of the set of DAEs is encompassed by the microkinetic model. The analytical solution on the other hand proceeds with the assumption of a rate determining step (RDS) and deriving the equation of the overall rate

of the reaction which depends on the RDS. It is important to note that the microkinetic model does not make assumptions about the RDS. Hence, it is common practice to have the microkinetic model predict the RDS and use this as an assumption in deriving the overall rate equation analytically. The results from these two approaches are then compared and more discussion on this later.

2.3.3 Potential energy surface and kinetic parameters

The rate of a chemical reaction $A \rightarrow B$ is given by

$$r = -k \frac{d[A]}{dt} \quad (2.40)$$

where k is the rate constant, $[A]$ is the initial concentration of the reactant A and dt is a small change in time. The negative (-) sign indicates the decrease in concentration of reactant A . Increasing the rate constant with the aid of a catalyst naturally increases the rate of the reaction. The rate constant is given by the Arrhenius expression as

$$k = \nu e^{-E_a/k_B T} \quad (2.41)$$

where ν is a prefactor, k_B is the Boltzmann constant, E_a is the activation energy of the elementary step and T is the temperature in kelvin (K). Since the Boltzmann constant is 8.617×10^{-5} eV/K, the rate constant largely depends on the activation energy, E_a . A potential energy diagram for this typical reaction shown in Figure 2.5.

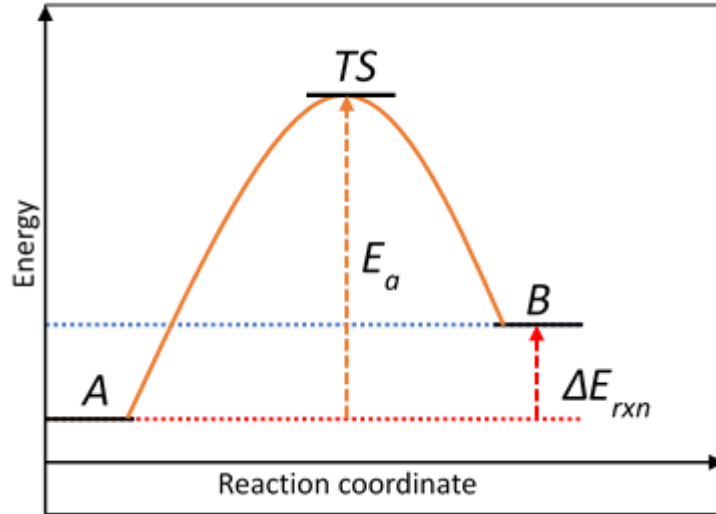


Figure 2.5 Potential energy diagram depicting E_a and E_{rxn} for a reaction $A \rightarrow B$

All elementary reactions can be approached from both forward and reverse direction. Irrespective of which side it is approached from, an energy barrier is encountered that needs to be overcome. If approaching from $A \rightarrow B$, a barrier of magnitude E_a needs to be overcome and if approaching from $B \rightarrow A$, a barrier of $(E_a - \Delta E_{rxn})$ needs to be overcome. It can be said that all elementary reaction steps can proceed in both the forward and the backward direction and regardless of the direction, you will encounter a barrier. This is the principle of microscopic reversibility.

2.3.4 Mean-field approximation

On a typical catalyst surface, there could be aggregation of a reaction intermediate in a certain region of the surface. This aggregation is usually due to attraction forces between intermediates. Such effects lead to island formation on the surface and such islands can prevent the adsorption of reactants and poisons the catalytic surface. Such effects typically reduce the binding energy of the reacting intermediates and are called

lateral interaction effect. Since it is difficult to account for such effects, as an initial approximation to the microkinetic model, we neglect the local topology of the catalyst surface and assume that every intermediate on the surface can interact with every other intermediate. Hence, we can describe the reaction rate using the surface concentration of each intermediate involved in the reaction. This assumption allows us to use equation (2.38) as an initial approximation to the model to solve for the concentration of each surface intermediate numerically. Using the results from the model, we can then refine the model to include lateral interaction effects by the most abundant surface intermediate (MASI).

2.3.5 Steps in microkinetic modeling

To perform microkinetic modeling, it is important to have either empirical or computational data on the reaction free energy and activation barrier for each elementary step. A combination of experimental and computational data on these parameters can also be used. All data employed in the microkinetic modeling in this work are computed from DFT calculations, as described in sections 2.1 and 2.2. Once this data is collected, the following steps are needed to construct the model:

1. Construct the set of elementary reaction steps.
2. Derive rate expressions for each of the elementary reaction steps.
3. Convert the set of rate expressions to a set of ordinary differential equations.
4. Define boundary conditions for the system (e.g. partial pressures), the initial values (e.g. initial surface concentrations) and any model parameters (e.g. temperature).
5. Solve the system of ordinary differential equations.

6. Interpret the results (using chemical intuition).

We have explored steps 1 to 3 already. For step 4, it is best to have experimentally determined conditions for partial pressures and temperature. If not, reasonable assumptions can be made by comparison with similar reactions. As for the initial surface concentrations, we need to first model a *transient* reactor where the reactants have barely settled on the surface. This condition is also said to be true when the percentage conversion of the reactant into products is $\sim 0\%$. In other words, the initial surface concentration of all reactants and reaction intermediates is zero at $t = 0$. In step 5, the set of DAEs are solved analytically to obtain the steady state surface concentrations of each intermediate. Using the surface concentrations and equation (2.38), we can calculate the turnover frequencies (TOFs) of each elementary step. Turnover frequency is the number of times a reaction occurs in time t . It is usually represented in units of (time^{-1}) . Chemical insights from the TOFs will be discussed in later sections.

2.4 Surface energy

Surfaces are created by cleaving atoms from the bulk across a pre-defined plane. Sometimes it is referred to as slab cutting. This creation of surfaces results in under-coordinated atoms at the surface, which are then available for chemical reactions. However, the energetics involved in creation of these surfaces play a vital role in whether this surface really exists. In other words, it would be futile to perform expensive DFT calculations on surfaces that require unrealistic energy for its formation in the first place. Hence, the term

surface energy, σ , can be defined as the energy needed to cleave a bulk crystal along a plane. The surface energy can be determined through DFT slab calculations as

$$\sigma = \frac{1}{A} [E_{slab} - nE_{bulk}] \quad (2.42)$$

where E_{slab} is the total energy of the slab model, E_{bulk} is the energy of a formula unit of the material in bulk, n is the number of formula units in the slab and A is the total surface area of the top and bottom of the slab. The surface energies are usually represented in eV/Å². It should be noted that surface energies need to be converged with respect to number of layers in the slab, k -points, energy cutoff and supercell size to name a few. Surface contributions to properties like adsorption energy play a crucial role in the accuracy of such properties. As a result, it is important to ensure convergence with respect to the aforementioned factors of the slab.

2.5 Adsorption energy

Adsorption energy or binding energy (BE) is qualitatively defined as the energy required (or liberated) for an atom or molecule to ‘stick/bind’ to the clean surface, where the surface can be a pure metal, alloy or an organometallic framework. The determination of the adsorption energy of a molecule (or atom) on a slab involves periodic DFT calculations to evaluate the total energy of the slab and the isolated molecule (or atom) separately and the system of the molecule (or atom) on top of the slab. A slab is a unit cell of the crystal lattice which is large enough to represent the bulk material. After calculating

the energy of the clean slab, E_{slab} , energy of the isolated molecule (or atom), E_{gas} and the system of the molecule on the slab, $E_{gas/slab}$, we can calculate the adsorption energy as

$$E_{ads} = E_{gas/slab} - E_{slab} - E_{gas} \quad (2.43)$$

The sign convention adopted in this study is if the adsorption energy is negative (−) the process is exothermic and if it is positive (+) it is endothermic. In other words, if the adsorption of a molecule on the surface is exothermic, it will have a negative (−) E_{ads} and vice versa. If the magnitude of the adsorption energy is in the range of 0.0 eV to 0.3 eV, it can be attributed to physisorption (or physical adsorption), which is simply a physical attraction of a molecule to the surface without any transfer of electrons from the molecule to the surface or vice versa. On the other hand, if the magnitude of the adsorption energy of a molecule on the surface is beyond 0.5 eV or 1.0 eV, it is termed as chemisorption (or chemical adsorption) which, unlike physisorption, involves transfer of electrons from the molecule to the surface or vice versa.

2.6 Spin density

Spin density is used to describe the (de-)localization of unpaired electron(s) on a free radical. It is calculated as the difference between the total electron density of a certain spin and the total electron density of the opposite spin. If the spin states are described as alpha (α) spin and beta (β) spin, the spin density can be described as,

$$\rho_{spin} = \rho_{\alpha} - \rho_{\beta} \quad (2.44)$$

When visualized, the spin density would represent the density corresponding to an unpaired electron present in the singly occupied molecular orbital (SOMO).

CHAPTER 3. CARBOXYLIC ACID DECARBONYLATION ON NICKEL: THE CRITICAL ROLE OF THE ACID BINDING GEOMETRY

3.1 Introduction

In this Chapter, a computational investigation of PAc DCN mechanisms on a Ni[111] surface was conducted with model validations being provided by spectroscopic measurements. The computational work presented in this chapter was carried out in collaboration with Dr. Eduardo Santillan-Jimenez and Dr. Robert Pace from Center for Applied Energy Research (CAER) and is published in ACS Catalysis.¹⁵² In this work, the reaction profile of PAc undergoing DCN was developed to understand the reaction mechanism as well as the descriptors that affect the turnover frequency (TOF) of this deoxygenation pathway. The results herein will form the basis for future work on other Ni phases and on Ni-based bimetallic systems, which are experimentally known to be practicable catalysts for deoxygenation reactions.^{25, 153-155}

3.2 Methods

Density functional theory (DFT) calculations were performed to determine the total ground state energies of all systems investigated using the Vienna Ab Initio Simulation Package (VASP).¹⁵⁶⁻¹⁵⁷ The Kohn-Sham equations were solved using plane wave basis sets. The projector-augmented wave (PAW) method¹⁴⁶ was used to describe electron-ion interactions. The Perdew-Burke-Ernzerhof (PBE) functional within the generalized gradient approximation (GGA) was used to calculate exchange-correlation energies.¹⁴⁵ The conjugate gradient algorithm was employed for ionic relaxation steps.¹⁵⁸ Geometric optimizations were performed with periodic boundary conditions with a plane wave energy

cutoff of 400 eV. A bulk calculation was performed on FCC-Ni to determine the lattice parameters. A periodic slab of Ni[111] surface was constructed from the respective bulk structure with five layers, separated by a vacuum of 15 Å to prevent interactions between repeating units. The bottom two layers were fixed to represent the bulk configuration while the top three layers were relaxed completely. The top layer consisted of 16 Ni atoms, allowing coverages as low as 1/16 ML.

The probe molecule PAc, which belongs to the C_s point group, was obtained from the NIST database.¹⁵⁹ Each adsorbate tested was isolated in a $20\text{Å}\times 20\text{Å}\times 20\text{Å}$ box to prevent inter-molecular interactions and relaxed with dipole corrections in all directions. Spin polarization was turned on for all relaxations. Self-consistent field (SCF) calculations for adsorption studies were converged to 1×10^{-6} eV/Å. A Methfessel-Paxton (MP) smearing of 0.2 eV and a Monkhorst-Pack grid of $3\times 3\times 1$ was used for Brillouin zone integration.

Using the above approach, the FCC-Ni bulk converged to a minimum total energy with a lattice constant of 3.52 Å, which is in reasonable agreement with reported values,¹⁶⁰⁻¹⁶² and identical to the experimental value.¹⁶³⁻¹⁶⁴ A clean surface of Ni[111] was constructed with a surface energy of $0.119\text{ eV}/\text{Å}^2$, which is lower than that of Ni[001] ($0.166\text{ eV}/\text{Å}^2$) and indicates that the close-packed [111] surface is more stable.¹⁴²⁻¹⁴³ All subsequent studies were performed on the Ni[111] surface with 16 surface atoms to account for minimal adsorbate interaction between periodic repeat units.

Adsorption studies were performed to determine the binding strength of each reaction intermediate isolated on the surface. For these studies, a dipole correction in the

z-coordinate was applied with second order MP smearing. Adsorbates were relaxed on the surface with the applied vacuum preventing interaction with repeating units in the periodic system. All adsorption energies and activation barriers were zero-point corrected.

The climbing-image nudged elastic band (cNEB)¹⁴⁷ method was used in combination with the dimer method¹⁴⁸ to determine the saddle points for each elementary step involved. A sequence of eight images between the initial and final state of an elementary step was used in the NEB calculations to identify an initial approximation of the saddle point, which was used as the starting point for the dimer method. In cases where the dimer run converged on the initial or the final state, the cNEB was allowed to progress until forces on all images were below 0.20 eV/Å to obtain a better approximation of the saddle point for a subsequent dimer calculation, which resulted in a converged saddle that was neither the initial nor the final state. Dynamical matrix calculations were carried out to determine vibrational frequencies according to the methods described by Henkelman and co-workers.¹⁶⁵

It is important to note that the experimental results, namely in situ diffuse reflectance infrared Fourier transform spectroscopy (DRIFTS) studies of PAc adsorption on a nickel catalyst were performed by Dr. Robert Pace and Dr. Eduardo Santillan-Jimenez from the Center for Applied Energy Research (CAER).

3.3 Results and Discussion

3.3.1 Determining the DCN reaction mechanism

Since the initial hypothesis of this work is that the binding mode of PAc plays a key role in the elucidation of the reaction mechanism, both DFT calculations and in situ DRIFTS measurements were used to test this hypothesis. The DFT results suggest that PAc binding on the Ni[111] surface energetically prefers a bidentate configuration comprised of an M–O–C σ bond on the top-site of a Ni atom and a weak Ni–HO interaction (indicated by O–H bond elongation from 0.98 Å in the gas phase to 1.02 Å on the surface), as shown in Figure 3.1. Notably, the α -carbon hydrogen atoms point away from the surface. A similar configuration was reported for PAc on a Pd[111] surface by Lu and co-workers;¹⁵ notably, the bidentate configuration was not identified to be the most energetically stable and was, instead, used to determine the transition state. The adsorption energy (E_{ads}) for the bidentate binding of PAc on Ni[111] is -0.34 eV. The free energy change for the binding of PAc on Ni[111] is exothermic by -0.34 eV, whereas Zare and co-workers¹⁸ report an endothermic binding of 0.69 eV for PAc on a similar Ni[111] surface, wherein a monodentate binding configuration for PAc was determined to be preferred. We associate these differences to the structure of PAc used in the binding energy calculations (Figure 3.1). The bidentate mode in Figure 3.1(B) is clearly the most stable adsorption mode where the distance between the α -carbon hydrogen and the Ni[111] surface is measured to be 4.94 Å while the same distance for the monodentate PAc bound to Ni[111] (Figure 3.1(A)) from the reproduced structure is 2.61 Å. It is clear from this analysis that PAc bound to the surface would need to undergo significant rearrangement from the bidentate configuration

to the monodentate along with a C–C bond rotation for the α -carbon dehydrogenation to occur as the first step in the mechanism. In addition, several studies have shown more accurate binding energies of aromatic and single chain hydrocarbons on transition metals when van der Waals (vdW) correction (as described by Grimme¹⁶⁶) is applied to the DFT functional.¹⁶⁷⁻¹⁷¹ However, to maintain consistency and enable comparisons between the binding modes in this and other works,¹⁸ vdW corrections were not employed in this contribution but will be included in future studies.

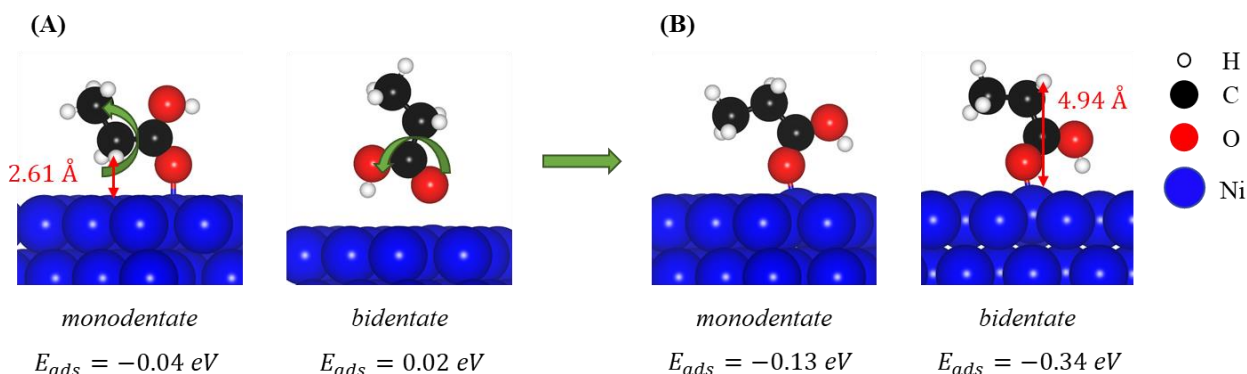


Figure 3.1 Binding modes of PAC on Ni[111] surface determined from DFT calculations with ZPE corrected adsorption energies. PAC structures in (A) was reproduced from [18]. Copyright [2020] American Chemical Society. While structures in (B) include PAC obtained from the NIST database. The difference between the two PAC structures is depicted by the green curved arrow indicating the internal C–C bond rotation of the molecule.

In view of these differing reports and the hypothesized importance of this phenomenon on the elucidation of the reaction mechanism, in situ DRIFTS measurements

were performed to elucidate the binding mode. Specifically, DRIFTS measurements were performed to study PAc adsorption on both Al_2O_3 and 20% $\text{Ni}/\text{Al}_2\text{O}_3$. These results confirm the binding mode of PAc to be predominantly bidentate in nature.

3.3.1.1 Binding energies and stable modes

As we are interested in determining the DCN reaction mechanism for PAc on $\text{Ni}[111]$, the binding configurations and adsorption energies were evaluated for several intermediates. The intermediate resulting from the dehydroxylation of PAc, $\text{CH}_3\text{CH}_2\text{CO}^*$, on $\text{Ni}[111]$ shows strong binding through both atoms in the $\text{C}=\text{O}$ group, with the carbon atom binding on a $\text{Ni}-\text{Ni}$ bridge site and the oxygen atom binding on a top Ni site, as shown in Figure 3.2(e). E_{ads} is -2.90 eV. The single dehydrogenation of the α -carbon of $\text{CH}_3\text{CH}_2\text{CO}^*$ results in CH_3CHCO^* , which has an E_{ads} of -1.82 eV. As shown in Figure 3.2(f), the α -carbon interacts in a σ -fashion with a top Ni atom while the carbon and oxygen atoms of the $\text{C}=\text{O}$ group bind to a $\text{Ni}-\text{Ni}$ bridge site and to a top Ni atom, respectively. The intermediate resulting from the α -carbon dehydrogenation of PAc is $\text{CH}_3\text{CHCOOH}^*$, which binds with E_{ads} of -1.28 eV; the binding mode is described to be via the α -carbon in a σ -fashion on top of a Ni atom, while the $\text{C}=\text{O}$ of the $-\text{COOH}$ group has a π interaction with the surface, as shown in Figure 3.2(b). The intermediate resulting from further α -carbon dehydrogenation of CH_3CHCOOH is the under-coordinated $\text{CH}_3\text{CCOOH}^*$, which binds to the surface with E_{ads} of -3.26 eV; here, the intermediate forms σ -bonds in a $\text{Ni}-\text{C}-\text{Ni}$ bridge and through an interaction between the $\text{C}=\text{O}$ group to form a $\text{Ni}-\text{O}-\text{Ni}$ bridge, as shown in Figure 3.2(c). The intermediate resulting from dehydroxylation of $\text{CH}_3\text{CCOOH}^*$ is the highly under-coordinated CH_3CCO^* , with a surface binding E_{ads} of -3.51 eV; each of the under-coordinated carbon atoms form two σ -bonds between two $\text{Ni}-\text{Ni}$ bridge sites and the $\text{C}=\text{O}$ group interacts with a top Ni atom, as shown in Figure 3.2(d). The well-known ethylidyne intermediate CH_3C^* binds strongly on the FCC-site involving three Ni atoms on the $\text{Ni}[111]$ surface as shown in Figure 3.2(h); E_{ads} of this intermediate, which is known to be responsible for coking on transition metal surfaces,¹⁷² is -5.88 eV. Other intermediates such as CH_3CH_2^* bind to a top Ni-atom, whereas $-\text{H}$, $-\text{OH}$ and $-\text{CO}$ all bind preferentially to the FCC site involving three Ni atoms on the $\text{Ni}[111]$ surface. The respective E_{ads} of these intermediates are listed in

Table 3.1.

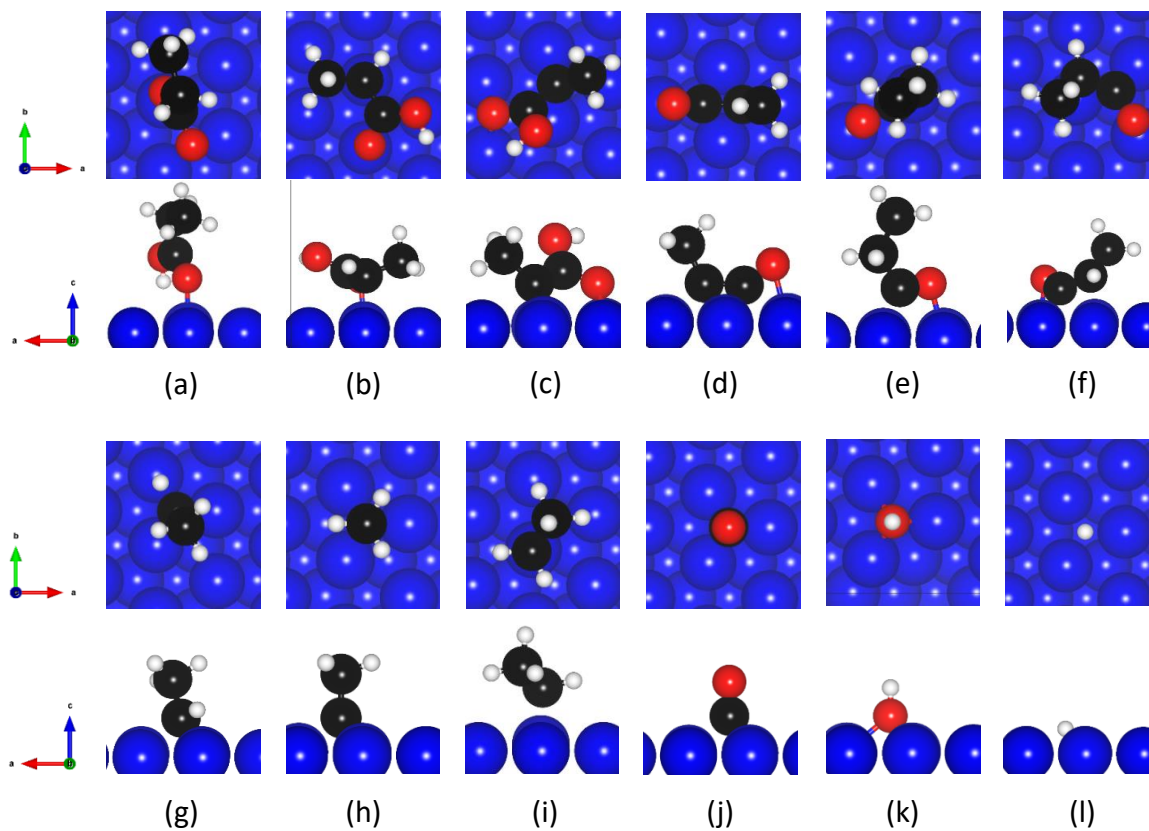


Figure 3.2 Stable binding modes of DCN intermediates on Ni[111] surface with top-view and side-view (Blue=Ni; Black=C; White=H; Red=O). (a) $\text{CH}_3\text{CH}_2\text{COOH}$ (b) CH_3CHCOOH (c) CH_3CCOOH (d) CH_3CCO (e) $\text{CH}_3\text{CH}_2\text{CO}$ (f) CH_3CHCO (g) CH_3CH (h) CH_3C (i) CH_3CH_2 (j) CO (k) OH (l) H .

Table 3.1 Adsorption energies of key DCN intermediates in the most stable binding modes, where * indicates surface intermediate.

Adsorbed Intermediates	Binding Energy, E_{ads} (eV)	
	Pd[111] ¹⁵ (GGA-PW91)	Ni[111] (GGA-PBE)
CH ₃ CH ₂ COOH*	-0.28	-0.34
CH ₃ CH ₂ CO*	-2.52	-2.90
CH ₃ CHCOOH*	-1.42	-1.28
CH ₃ CCOOH*	-3.23	-3.26
CH ₃ CHCO*	-1.22	-1.82
CH ₃ CCO*	-3.00	-3.51
CH ₃ C*	-5.61	-5.88
CH ₃ CH*	-3.65	-4.01
CH ₃ CH ₂ *	-1.68	-1.60
CH ₃ CH ₃ *	-0.11	0.30
CO*	-1.99	-2.02
OH*	-2.59	-3.06
H*	-2.70	-2.62

Free energy surface diagrams were constructed to investigate the mechanisms underpinning a DCN reaction pathway for PAc on Ni[111]. The reference state chosen was CH₃CH₂COOH_(g) + H_{2(g)} + *; where * represents the clean Ni[111] slab without any adsorbates. For each step, E_{ads} was determined for a proposed intermediate (associated with ‘*’) on the Ni[111] surface. Reaction enthalpies (ΔE_{rxn}) for each elementary step was calculated for all adsorbed species as isolated species on the surface to avoid lateral interactions between repeat units. The free energy change of each elementary step was

determined using a standard procedure described elsewhere¹⁷³, with the help of Shomate equations¹⁷⁴ to calculate the entropy of gas phase reactants and products. The entropy change of the surface intermediates were obtained using the formula,¹⁵¹

$$S_{vib} = k_B \sum_v \left[\frac{h\omega_v}{k_B T \left(e^{\frac{h\omega_v}{k_B T}} - 1 \right)} - \ln \left(1 - e^{-\frac{h\omega_v}{k_B T}} \right) \right]$$

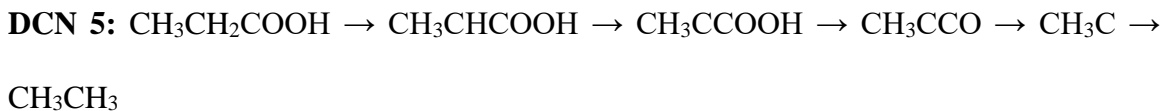
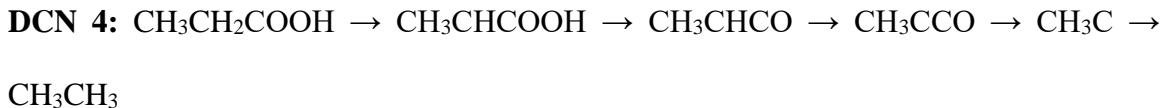
where ω_v is the vibrational frequency of surface intermediates obtained from dynamical matrix calculations using VTST tools.¹⁷⁵ Note, modes associated with vibration of surface atoms were not considered and all modes less than 200 cm^{-1} (also called ‘soft’ modes) were approximated to 200 cm^{-1} . Table 3.2 presents ΔG_{rxn} , ΔE_a and the entropy corrections of all the unique elementary steps involved in the DCN reaction mechanism from the 5 reaction pathways considered without lateral interactions.

Table 3.2 Reaction free energy, Activation barrier and Entropy correction terms for each elementary step without lateral interaction effect. All energies are in eV.

Elementary steps	Reaction free energy (ΔG_{rxn} ; eV)	Activation barrier (ΔE_a ; eV)	Entropy correction ($T\Delta S$; eV)
$\text{CH}_3\text{CH}_2\text{COOH}_{(g)} + * \rightarrow \text{CH}_3\text{CH}_2\text{COOH}^*$	-0.34	0.00	-0.001
$\text{CH}_3\text{CH}_2\text{COOH}^* + * \rightarrow \text{CH}_3\text{CH}_2\text{CO}^* + \text{OH}^*$	-0.14	0.61	0.065
$\text{CH}_3\text{CH}_2\text{CO}^* + * \rightarrow \text{CH}_3\text{CH}_2^* + \text{CO}^*$	-0.58	0.74	0.142
$\text{CH}_3\text{CH}_2\text{CO}^* + * \rightarrow \text{CH}_3\text{CHCO}^* + \text{H}^*$	-0.31	0.29	0.198
$\text{CH}_3\text{CHCO}^* + * \rightarrow \text{CH}_3\text{CCO}^* + \text{H}^*$	-0.74	0.14	0.182
$\text{CH}_3\text{CCO}^* + * \rightarrow \text{CH}_3\text{C}^* + \text{CO}^*$	-1.20	0.08	0.078
$\text{CH}_3\text{C}^* + \text{H}^* \rightarrow \text{CH}_3\text{CH}^* + *$	0.86	0.86	-0.152
$\text{CH}_3\text{CH}^* + \text{H}^* \rightarrow \text{CH}_3\text{CH}_2^* + *$	0.80	0.86	-0.165
$\text{CH}_3\text{CH}_2^* + \text{H}^* \rightarrow \text{CH}_3\text{CH}_3^* + *$	0.08	0.48	-0.171
$\text{CH}_3\text{CHCO}^* \rightarrow \text{CH}_3\text{CH}^* + \text{CO}^*$	-1.07	0.35	0.109
$\text{CO}_{(g)} + * \rightarrow \text{CO}^*$	-2.01	0.00	-0.005
$\text{CH}_3\text{CH}_3_{(g)} + * \rightarrow \text{CH}_3\text{CH}_3^*$	0.27	0.00	0.035
$\text{OH}^* + \text{H}^* \rightarrow \text{H}_2\text{O}^* + *$	0.56	1.14	-0.084
$\text{H}_2\text{O}_{(g)} + * \rightarrow \text{H}_2\text{O}^*$	-0.09	0.00	-0.097
$\text{H}_2^* + * \rightarrow \text{H}^* + \text{H}^*$	-0.98	0.31	0.152
$\text{H}_{2(g)} + * \rightarrow \text{H}_2^*$	-0.63	0.00	0.431

PAC DCN on Ni[111] can proceed through the following five reaction pathways:

DCN 1: $\text{CH}_3\text{CH}_2\text{COOH} \rightarrow \text{CH}_3\text{CH}_2\text{CO} \rightarrow \text{CH}_3\text{CH}_2 \rightarrow \text{CH}_3\text{CH}_3$



In turn, the five pathways above include several elementary steps, all of which were examined.

$\text{CH}_3\text{CH}_2\text{COOH}^* \rightarrow \text{CH}_3\text{CH}_2\text{CO}^* + \text{OH}^*$: The direct dehydroxylation of PAc is thermoneutral with ΔG_{rxn} of -0.14 eV. A transition state with an energy barrier (ΔG_a) of 0.61 eV and a single imaginary frequency of $240i$ cm^{-1} was identified. In other works on Pd[111], this step was reported to be endothermic by 0.42 eV with a barrier of 0.92 eV,¹⁵ which implies that this step is both thermodynamically and kinetically more favorable on Ni[111]. Zare and co-workers reported a similar activation barrier of 0.60 eV on Ni[111] from a monodentate PAc binding mode with a ΔG_{rxn} of -0.25 eV.¹⁸

$\text{CH}_3\text{CH}_2\text{COOH}^* \rightarrow \text{CH}_3\text{CHCOOH}^* + \text{H}^*$: Since recent computational and experimental studies concerning PAc adsorption suggest a bidentate binding mode while some theoretical studies suggest a *cis* mode (*vide supra*), both α -carbon dehydrogenation scenarios were considered. In the bidentate adsorption scenario, where the α -carbon hydrogens are relatively far away (4.94 Å) from the surface (Figure 3.1), the dehydrogenation step is deemed unviable since the cNEB and dimer calculations never

converged to a saddle and, as noted earlier, the structure would need to undergo significant rearrangement on the surface. In the less stable *cis* mode of PAc adsorption, the dehydrogenation step on Ni[111] is endothermic by 0.31 eV, whereas Zare and co-workers¹⁸ reported it to be thermoneutral by -0.05 eV on Ni[111] and Lu and co-workers¹⁵ reported it is thermoneutral by -0.10 eV with a barrier of 0.62 eV on Pd[111]. This distinction is likely due to the starting configuration of PAc used in these studies, which is less stable (by 0.05 eV) when compared to the PAc configuration presented in this work. Although this may be a small difference, as stated earlier, the C-COOH rotation barrier is significant and cannot be neglected.³⁵ In addition, experimental evidence suggests a bidentate adsorption mode. These results highlight the importance of the PAc binding mode, and the value of the in situ DRIFTS measurements, which confirm that PAc predominantly binds to the Ni surface in a bidentate configuration. In view of the latter, efforts to elucidate the DCN mechanism focused on routes that start with PAc adsorbed on Ni[111] in a bidentate configuration (in which an α -carbon dehydrogenation of PAc is unlikely to occur).

$\text{CH}_3\text{CH}_2\text{CO}^* \rightarrow \text{CH}_3\text{CH}_2^* + \text{CO}^*$: The direct $-\text{CO}$ abstraction of the $\text{CH}_3\text{CH}_2\text{CO}^*$ intermediate is exothermic on Ni[111] with ΔG_{rxn} of -0.58 eV. Zare and co-workers report similar ΔG_{rxn} with an activation barrier of 0.78 eV;¹⁸ in this work, the activation energy was determined to be 0.74 eV with the transition state identified with an imaginary frequency of $418i$ cm^{-1} . This similarity suggests that the binding mode, which differs in this work and in that of Zare and co-workers, only impacts some elementary steps within the DCN mechanism.

$\text{CH}_3\text{CH}_2\text{CO}^* \rightarrow \text{CH}_3\text{CHCO}^* + \text{H}^*$: As shown by Lu and co-workers¹⁵, the α -carbon dehydrogenation steps likely lead to the surface formation of ethylidyne (CH_3C^*), which is a well-known coking precursor.¹⁷⁶⁻¹⁷⁸ Here, this step is exothermic on Ni[111] with a ΔG_{rxn} of -0.31 eV, an activation barrier ΔG_a of 0.29 eV, and a transition state with an imaginary frequency of $821i$ cm^{-1} . Notably, this α -carbon dehydrogenation step is more feasible than previous reports of ΔG_{rxn} and ΔG_a values on Ni[111] (0.19 eV and 0.49 eV, respectively)¹⁸.

$\text{CH}_3\text{CHCO}^* \rightarrow \text{CH}_3\text{CCO}^* + \text{H}^*$: The α -carbon dehydrogenation of CH_3CHCO^* is exothermic with a ΔG_{rxn} of -0.74 eV and a ΔG_a of 0.14 eV. The transition state has an imaginary frequency of $271i$ cm^{-1} . Zare and co-workers¹⁸ report a very similar ΔG_{rxn} and ΔG_a .

$\text{CH}_3\text{CCO}^* \rightarrow \text{CH}_3\text{C}^* + \text{CO}^*$: The decarbonylation of CH_3CCO^* to form ethylidyne on Ni[111] is highly exothermic (-1.20 eV) and, hence, thermodynamically favorable. However, the energetics involved in all prior steps required to form CH_3CCO^* need to be taken into consideration as they indicate that alternative pathways are more favorable. The activation barrier ΔG_a was 0.08 eV with the transition state identified at $322i$ cm^{-1} .

$\text{CH}_3\text{CHCO}^* \rightarrow \text{CH}_3\text{CH}^* + \text{CO}^*$: Since the formation of CH_3CHCO^* on Ni[111] is exothermic with a relatively low barrier, and the decarbonylation of CH_3CHCO^* is also exothermic (by -1.07 eV on Ni[111]), the formation of CH_3CH^* (a transition state with an imaginary frequency of $456i$ cm^{-1}) appears to be a favorable pathway for the DCN reaction

to proceed. However, an activation barrier ΔG_a of 0.35 eV, which is more than double a previously reported barrier,¹⁸ suggests a thermodynamically driven step.

Hydrogenation steps: Hydrogenation is key to the propensity for coke precursor formation on the catalyst surface. Both the hydrogenation of ethylidyne (CH_3C^*) to afford CH_3CH^* as well as the hydrogenation of the latter to form CH_3CH_2^* are endothermic on Ni[111] (0.86 and 0.80 eV, respectively). The activation barriers for both hydrogenation steps are 0.86 eV, suggesting that these steps are unfavorable. Lastly, the hydrogenation of CH_3CH_2^* to yield ethane is thermoneutral (0.08 eV) with a barrier of 0.48 eV, which suggests that this step is thermodynamically viable. It is important to note that ethylene formation competes with ethane formation; however, the latter is more thermodynamically driven than the former, as shown by Zare and co-workers.¹⁸ Albeit this is not critical in studies probing and striving to elucidate the DCN mechanism, it could be addressed in future works focused on coking.

Considering we could not obtain a converged saddle point for the transition state concerning the α -carbon dehydrogenation of PAc, we reduce the DCN mechanism to consist of only **DCN1**, **DCN2** and **DCN3**. The resulting free energy diagram with the respective reaction free energies and activation barriers are shown in Figure 3.3.

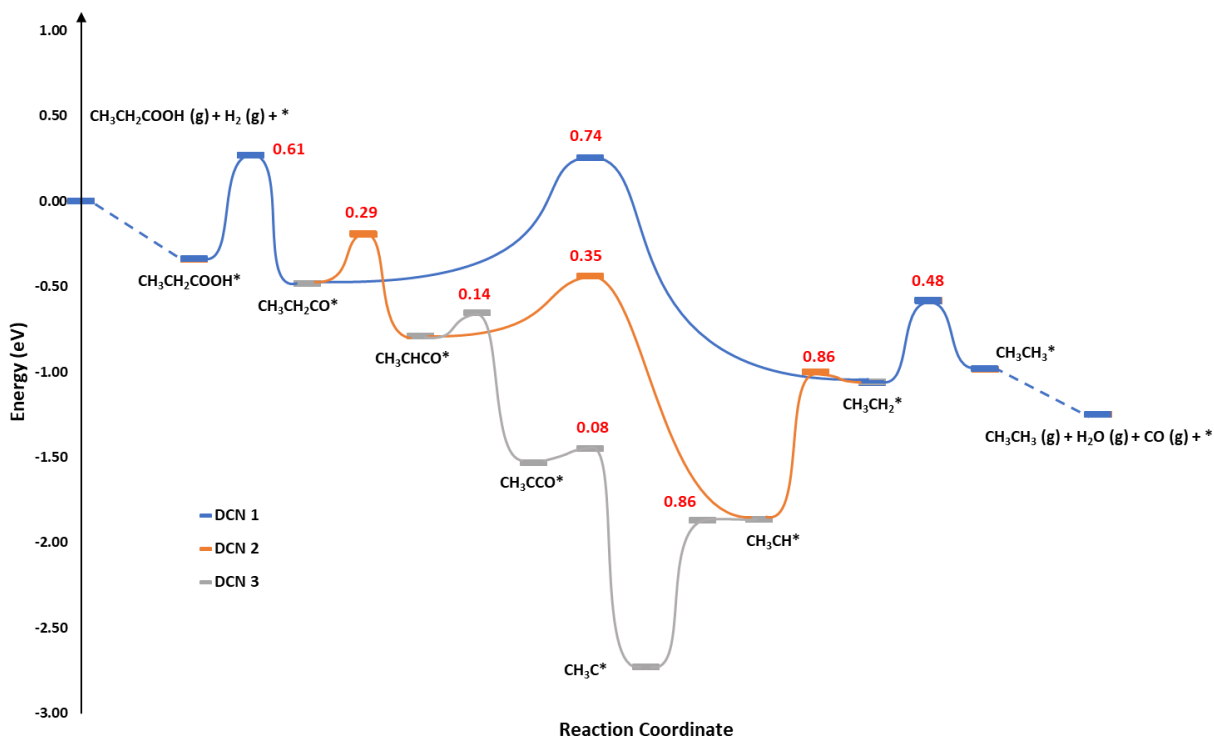


Figure 3.3 Free energy surface diagrams for three DCN reaction pathways on a Ni[111] surface with $\text{CH}_3\text{CH}_2\text{COOH}(\text{g}) + \text{H}_2(\text{g}) + *$ as the reference state (transition states with an activation barrier are shown in red for each elementary step).

3.3.2 Microkinetic modeling

Microkinetic modeling is widely used to study reaction mechanisms under experimental conditions using parameters derived from DFT calculations.¹⁷³ This approach can be used to analyze the role of key intermediates in a reaction mechanism in ways that are typically beyond the reach of experimental measurements. Here, the methods described by Dumesic and co-workers¹⁷³ were employed. Admittedly, stepped facets have been demonstrated to facilitate DCN/DCX pathways more readily than the [111] facet on transition metal surfaces.^{18, 36, 179} However, the study of key intermediates and likely

DCN/DCX pathways on the Ni[111] facet represents a necessary first step preceding studies involving other surfaces, since Ni[111] is a stable (lower energy) surface on which to perform binding energy and transition state calculations.

Against this backdrop, a simple mean-field microkinetic model¹⁸⁰ was used to study the DCN mechanisms of PAc on the Ni[111] surface. The experimental conditions reported for the DCN of PAc over Ni-based catalyst^{17, 181} – namely, a temperature of 573 K and a total pressure of 1 bar ($p_{\text{PAc}} = 0.01$ bar; $p_{\text{H}_2} = 0.20$ bar; rest inert balance) – were used to construct the model. It is important to note that the experimental work reported a very low activity (<1% conversion) at 473K for deoxygenation of PAc on a Ni catalyst and observed highest activity at 623K, which presents a strong case for the use of higher reaction temperatures in the microkinetic model.^{17, 181} Otyuskaya and co-workers also suggest that higher H₂ partial pressure results in increased propanol formation.¹⁷ For these reasons, the partial pressure of PAc used was small enough to model a low conversion transient continuous stirred tank reactor (CSTR) with the ratio of PAc:H₂ set to 1:20. Rate expressions for all the elementary steps were written as follows:

$$r_i = k_i^+ \prod_{\text{reactant}} \theta_{\text{reactant}} - k_i^- \prod_{\text{product}} \theta_{\text{product}}$$

where for the elementary step 'i', k_i^+ is the forward rate constant, k_i^- is the reverse rate constant, p is the partial pressure and θ is the fractional surface coverage of the reactant or product.

The set of rate expression can be expressed as,

$$r_0 = k_0^+ p_A \theta_* - k_0^- \theta_A$$

$$r_1 = k_1^+ \theta_A \theta_* - k_1^- \theta_L \theta_{OH}$$

$$r_2 = k_2^+ \theta_A \theta_* - k_2^- \theta_B \theta_H$$

$$r_3 = k_3^+ \theta_L \theta_* - k_3^- \theta_J \theta_{CO}$$

$$r_4 = k_4^+ \theta_L \theta_* - k_4^- \theta_D \theta_H$$

$$r_5 = k_5^+ \theta_B \theta_* - k_5^- \theta_D \theta_{OH}$$

$$r_6 = k_6^+ \theta_B \theta_* - k_6^- \theta_F \theta_H$$

$$r_7 = k_7^+ \theta_D \theta_* - k_7^- \theta_I \theta_{CO}$$

$$r_8 = k_8^+ \theta_D \theta_* - k_8^- \theta_E \theta_H$$

$$r_9 = k_9^+ \theta_E \theta_* - k_9^- \theta_G \theta_{CO}$$

$$r_{10} = k_{10}^+ \theta_G \theta_H - k_{10}^- \theta_I \theta_*$$

$$r_{11} = k_{11}^+ \theta_I \theta_H - k_{11}^- \theta_J \theta_*$$

$$r_{12} = k_{12}^+ \theta_J \theta_H - k_{12}^- \theta_K \theta_*$$

$$r_{13} = k_{13}^+ p_K \theta_* - k_{13}^- \theta_K$$

$$r_{14} = k_{14}^+ \theta_F \theta_* - k_{14}^- \theta_E \theta_{OH}$$

$$r_{15} = k_{15}^+ p_{CO} \theta_* - k_{15}^- \theta_{CO}$$

$$r_{16} = k_{16}^+ \theta_{OH} \theta_H - k_{16}^- \theta_{H_2O} \theta_*$$

$$r_{17} = k_{17}^+ p_{H_2O} \theta_* - k_{17}^- \theta_{H_2O}$$

$$r_{18} = k_{18}^+ \theta_{H_2} \theta_* - k_{18}^- \theta_H^2$$

$$r_{19} = k_{19}^+ p_{H_2} \theta_* - k_{19}^- \theta_{H_2}$$

where, the shorthand notations are listed in Table 3.3

Table 3.3 Shorthand notation of DCN reaction intermediates

Intermediate	Notation
CH ₃ CH ₂ COOH	A
CH ₃ CHCOOH	B
CH ₃ CH ₂ CO	L
CH ₃ CHCO	D
CH ₃ CCO	E
CH ₃ CCOOH	F
CH ₃ C	G
CH ₃ CH	I
CH ₃ CH ₂	J
CH ₃ CH ₃	K
CO	CO
OH	OH
H	H

The elementary steps and their designated numbers are provided in

Table 3.4

Table 3.4 List of all elementary steps in the DCN mechanism

Step #	Elementary Step
0	$\text{CH}_3\text{CH}_2\text{COOH}(\text{g}) + * \rightarrow \text{CH}_3\text{CH}_2\text{COOH}^*$
1	$\text{CH}_3\text{CH}_2\text{COOH}^* + * \rightarrow \text{CH}_3\text{CH}_2\text{CO}^* + \text{OH}^*$
2	$\text{CH}_3\text{CH}_2\text{COOH}^* + * \rightarrow \text{CH}_3\text{CHCOOH}^* + \text{H}^*$
3	$\text{CH}_3\text{CH}_2\text{CO}^* + * \rightarrow \text{CH}_3\text{CH}_2^* + \text{CO}^*$
4	$\text{CH}_3\text{CH}_2\text{CO}^* + * \rightarrow \text{CH}_3\text{CHCO}^* + \text{H}^*$
5	$\text{CH}_3\text{CHCOOH}^* + * \rightarrow \text{CH}_3\text{CHCO}^* + \text{OH}^*$
6	$\text{CH}_3\text{CHCOOH}^* + * \rightarrow \text{CH}_3\text{CCOOH}^* + \text{H}^*$
7	$\text{CH}_3\text{CHCO}^* + * \rightarrow \text{CH}_3\text{CH}^* + \text{CO}^*$
8	$\text{CH}_3\text{CHCO}^* + * \rightarrow \text{CH}_3\text{CCO}^* + \text{H}^*$
9	$\text{CH}_3\text{CCO}^* + * \rightarrow \text{CH}_3\text{C}^* + \text{CO}^*$
10	$\text{CH}_3\text{C}^* + \text{H}^* \rightarrow \text{CH}_3\text{CH}^* + *$
11	$\text{CH}_3\text{CH}^* + \text{H}^* \rightarrow \text{CH}_3\text{CH}_2^* + *$
12	$\text{CH}_3\text{CH}_2^* + \text{H}^* \rightarrow \text{CH}_3\text{CH}_3^* + *$
13	$\text{CH}_3\text{CH}_3(\text{g}) + * \rightarrow \text{CH}_3\text{CH}_3^*$
14	$\text{CH}_3\text{CCOOH}^* + * \rightarrow \text{CH}_3\text{CCO}^* + \text{OH}^*$
15	$\text{CO}(\text{g}) + * \rightarrow \text{CO}^*$
16	$\text{OH}^* + \text{H}^* \rightarrow \text{H}_2\text{O}^* + *$
17	$\text{H}_2\text{O}(\text{g}) + * \rightarrow \text{H}_2\text{O}^*$
18	$\text{H}_2^* + * \rightarrow \text{H}^* + \text{H}^*$
19	$\text{H}_2(\text{g}) + * \rightarrow \text{H}_2^*$

Applying the pseudo-steady state approximation and rearranging for the surface concentration for each intermediate, we arrive at:

$$\frac{d\theta_A}{dt} = r_0 - r_1 = 0 \Rightarrow k_0^+ p_A \theta_* - k_0^- \theta_A - k_1^+ \theta_A \theta_* + k_1^- \theta_L \theta_{OH} = 0$$

$$\frac{d\theta_L}{dt} = r_1 - r_3 - r_4 = 0$$

$$\Rightarrow k_1^+ \theta_A \theta_* - k_1^- \theta_L \theta_{OH} - k_3^+ \theta_L \theta_* + k_3^- \theta_j \theta_{CO} - k_4^+ \theta_L \theta_* + k_4^- \theta_D \theta_H$$

$$= 0$$

$$\frac{d\theta_D}{dt} = r_4 - r_7 - r_8 = 0$$

$$\Rightarrow k_4^+ \theta_L \theta_* - k_4^- \theta_D \theta_H - k_7^+ \theta_D \theta_* + k_7^- \theta_I \theta_{CO} - k_8^+ \theta_D \theta_* + k_8^- \theta_E \theta_H$$

$$= 0$$

$$\frac{d\theta_E}{dt} = r_8 - r_9 = 0 \Rightarrow k_8^+ \theta_D \theta_* - k_8^- \theta_E \theta_H - k_9^+ \theta_E \theta_* + k_9^- \theta_G \theta_{CO} = 0$$

$$\frac{d\theta_G}{dt} = r_9 - r_{10} = 0 \Rightarrow k_9^+ \theta_E \theta_* - k_9^- \theta_G \theta_{CO} - k_{10}^+ \theta_G \theta_H + k_{10}^- \theta_I \theta_* = 0$$

$$\frac{d\theta_I}{dt} = r_7 + r_{10} - r_{11} = 0$$

$$\Rightarrow k_7^+ \theta_D \theta_* - k_7^- \theta_I \theta_{CO} + k_{10}^+ \theta_G \theta_H - k_{10}^- \theta_I \theta_* - k_{11}^+ \theta_I \theta_H + k_{11}^- \theta_j \theta_*$$

$$= 0$$

$$\frac{d\theta_j}{dt} = r_3 + r_{11} - r_{12} = 0$$

$$\Rightarrow k_3^+ \theta_L \theta_* - k_3^- \theta_j \theta_{CO} + k_{11}^+ \theta_I \theta_H - k_{11}^- \theta_j \theta_* - k_{12}^+ \theta_j \theta_H + k_{12}^- \theta_K \theta_*$$

$$= 0$$

$$\frac{d\theta_K}{dt} = r_{12} + r_{13} = 0 \Rightarrow k_{12}^+ \theta_J \theta_H - k_{12}^- \theta_K \theta_* + k_{13}^+ p_K \theta_* - k_{13}^- \theta_K = 0$$

$$\frac{d\theta_{CO}}{dt} = r_3 + r_7 + r_9 + r_{15} = 0$$

$$\Rightarrow k_3^+ \theta_L \theta_* - k_3^- \theta_J \theta_{CO} + k_7^+ \theta_D \theta_* - k_7^- \theta_I \theta_{CO} + k_9^+ \theta_E \theta_* - k_9^- \theta_G \theta_{CO} + k_{15}^+ p_{CO} \theta_*$$

$$-k_{15}^- \theta_{CO} = 0$$

$$\frac{d\theta_{OH}}{dt} = r_1 - r_{16} = 0 \Rightarrow k_1^+ \theta_A \theta_* - k_1^- \theta_L \theta_{OH} - k_{16}^+ \theta_{OH} \theta_H + k_{16}^- \theta_{H_2O} \theta_* = 0$$

$$\frac{d\theta_H}{dt} = r_4 + r_8 - r_{10} - r_{11} - r_{12} - r_{16} + r_{18} = 0$$

$$\begin{aligned} \Rightarrow k_4^+ \theta_L \theta_* - k_4^- \theta_D \theta_H + k_8^+ \theta_D \theta_* - k_8^- \theta_E \theta_H - k_{10}^+ \theta_G \theta_H + k_{10}^- \theta_I \theta_* - k_{11}^+ \theta_I \theta_H + k_{11}^- \theta_J \theta_* \\ - k_{12}^+ \theta_J \theta_H + k_{12}^- \theta_K \theta_* - k_{16}^+ \theta_{OH} \theta_H + k_{16}^- \theta_{H_2O} \theta_* + k_{18}^+ \theta_{H_2} \theta_* - k_{18}^- \theta_H^2 \\ = 0 \end{aligned}$$

$$\frac{d\theta_{H_2}}{dt} = -r_{18} + r_{19} = 0 \Rightarrow -k_{18}^+ \theta_{H_2} \theta_* + k_{18}^- \theta_H^2 + k_{19}^+ p_{H_2} \theta_* - k_{19}^- \theta_{H_2}$$

$$\frac{d\theta_{H_2O}}{dt} = r_{16} + r_{17} = 0 \Rightarrow k_{16}^+ \theta_{OH} \theta_H - k_{16}^- \theta_{H_2O} \theta_* + k_{17}^+ p_{H_2O} \theta_* - k_{17}^- \theta_{H_2O} = 0$$

$$\begin{aligned}
\frac{d\theta_*}{dt} &= -r_9 + r_{10} + r_{11} + r_{12} - r_{13} - r_{15} + r_{16} - r_{17} - r_{18} - r_{19} - r_0 - r_1 - r_4 - r_8 = 0 \\
&\Rightarrow -k_9^+ \theta_E \theta_* + k_9^- \theta_G \theta_{CO} + k_{11}^+ \theta_I \theta_H - k_{11}^- \theta_J \theta_*^3 + k_{10}^+ \theta_G \theta_H - k_{10}^- \theta_I \theta_* \\
&+ k_{12}^+ \theta_J \theta_H - k_{12}^- \theta_K \theta_* - k_{13}^+ p_K \theta_* + k_{13}^- \theta_K - k_{15}^+ p_{CO} \theta_* + k_{15}^- \theta_{CO} \\
&+ k_{16}^+ \theta_{OH} \theta_H - k_{16}^- \theta_{H_2O} \theta_* - k_{17}^+ p_{H_2O} \theta_* + k_{17}^- \theta_{H_2O} - k_{18}^+ \theta_{H_2} \theta_* + k_{18}^- \theta_H^2 \\
&- k_{19}^+ p_{H_2} \theta_* + k_{19}^- \theta_{H_2} - k_0^+ p_A \theta_*^2 + k_0^- \theta_A - k_1^+ \theta_A \theta_* + k_1^- \theta_L \theta_{OH} \\
&- k_4^+ \theta_L \theta_*^2 + k_4^- \theta_D \theta_H - k_8^+ \theta_D \theta_* + k_8^- \theta_E \theta_H = 0
\end{aligned}$$

The site balance equation can be written such that the mass conservation rule applies:

$$\theta_* + \theta_A + \theta_L + \theta_D + \theta_E + \theta_G + \theta_I + \theta_J + \theta_K + \theta_{CO} + \theta_{OH} + \theta_H + \theta_{H_2O} = 1$$

The set of ordinary differential equations were solved to obtain the steady-state fractional coverage of each intermediate.

3.3.2.1 Lateral interaction effect

Our transient CSTR model showed a 0.5 ML coverage of H* on the surface under steady state conditions. To account for the lateral interaction effect of H* on the binding energy of key reaction intermediates on the catalyst surface, we carried out a simple first order approximated co-adsorption calculations of one H-atom co-adsorbed with the intermediate on the surface. Considering the TOF (net rate) for all elementary steps shown in Table 3.5, the dominant pathway identified in this work starts with the dehydroxylation of PAc ($\text{CH}_3\text{CH}_2\text{COOH}^* \rightarrow \text{CH}_3\text{CH}_2\text{CO}^*$) followed by two α -carbon dehydrogenation steps ($\text{CH}_3\text{CH}_2\text{CO}^* \rightarrow \text{CH}_3\text{CHCO}^* \rightarrow \text{CH}_3\text{CCO}^*$) then, the decarbonylation of CH_3CCO^* to ethylidyne (CH_3C^*) and finally, the hydrogenation of ethylidyne to yield ethane. In the

co-adsorbed state, the binding energy of PAc was lowered to (-0.49 eV). All other key intermediates also showed stronger binding in the presence of H* co-adsorbed on the surface (see Table 3.2 and Table 3.5). However, the activation barriers calculated using Bragg-Williams approximation^{16, 182} for key reaction intermediates showed an increase in E_a for all elementary steps in the dominant pathway due to the interaction with co-adsorbed H* (see Table 3.2 and Table 3.5).

Including the lateral interaction effects on key intermediates, the adsorption of PAc (competes with H₂ (g) adsorption) is reversible with a TOF of $1.70 \times 10^{-6} \text{ s}^{-1}$ favorable in the reverse direction followed by the elementary step of PAc dehydroxylation on the Ni[111] surface with a TOF of $2.75 \times 10^{-11} \text{ s}^{-1}$ and is irreversible, while the decarbonylation of CH₃CH₂CO* has a TOF of $3.71 \times 10^{-14} \text{ s}^{-1}$ (also irreversible). The decarbonylation of CH₃CH₂CO* is slower than the α -carbon dehydrogenation ($2.75 \times 10^{-11} \text{ s}^{-1}$) step by three orders of magnitude and hence it is likely that PAc dehydroxylation is followed by α -carbon dehydrogenation of CH₃CH₂CO* instead of the direct decarbonylation. The steps including and following the α -carbon dehydrogenation of CH₃CH₂CO* are all in steady state with the irreversible dehydroxylation of PAc and for this reason, we believe that dehydroxylation of PAc is the rate determining step in the dominant pathway. The overall TOF is $2.75 \times 10^{-11} \text{ s}^{-1}$ at 573K under the given reaction conditions, which is much slower than the experimental¹⁸¹ TOF of $1.50 \times 10^{-4} \text{ s}^{-1}$. This could be attributed to the Ni[111] facet being less active to deoxygenation than other nickel surfaces.

Table 3.5 Zero-point energy corrected activation energy barrier, reaction free energy change, and turnover frequency for each elementary step involved in the DCN mechanism of PAc on Ni[111] with lateral interaction effects included.

Elementary step	Activation Barrier (E_a ; eV)	Reaction free energy (ΔG_{rxn} ; eV)	TOF (s^{-1})	Forward rate (s^{-1})	Reverse rate (s^{-1})
$\text{CH}_3\text{CH}_2\text{COOH}_{(g)} + * \rightarrow \text{CH}_3\text{CH}_2\text{COOH}^*$	0.00	-0.49	-1.70×10^{-6}	9.22×10^2	9.22×10^2
$\text{CH}_3\text{CH}_2\text{COOH}^* + * \rightarrow \text{CH}_3\text{CH}_2\text{CO}^* + \text{OH}^*$	0.65	-0.30	2.75×10^{-11}	2.75×10^{-11}	6.41×10^{-26}
$\text{CH}_3\text{CH}_2\text{CO}^* + * \rightarrow \text{CH}_3\text{CH}_2^* + \text{CO}^*$	0.85	-0.49	3.71×10^{-14}	3.71×10^{-14}	3.35×10^{-28}
$\text{CH}_3\text{CH}_2\text{CO}^* + * \rightarrow \text{CH}_3\text{CHCO}^* + \text{H}^*$	0.38	-0.33	2.75×10^{-11}	3.35×10^{-10}	3.08×10^{-10}
$\text{CH}_3\text{CHCO}^* + * \rightarrow \text{CH}_3\text{CCO}^* + \text{H}^*$	0.23	-0.70	2.52×10^{-11}	2.56×10^{-11}	4.48×10^{-13}
$\text{CH}_3\text{CCO}^* + * \rightarrow \text{CH}_3\text{C}^* + \text{CO}^*$	0.11	-1.31	2.52×10^{-11}	2.52×10^{-11}	1.45×10^{-23}
$\text{CH}_3\text{C}^* + \text{H}^* \rightarrow \text{CH}_3\text{CH}^* + *$	0.86	0.86	2.52×10^{-11}	4.71×10^{-8}	4.71×10^{-8}
$\text{CH}_3\text{CH}^* + \text{H}^* \rightarrow \text{CH}_3\text{CH}_2^* + *$	0.86	0.80	2.75×10^{-11}	2.76×10^{-11}	8.35×10^{-14}
$\text{CH}_3\text{CH}_2^* + \text{H}^* \rightarrow \text{CH}_3\text{CH}_3^* + *$	0.48	0.08	2.75×10^{-11}	2.75×10^{-11}	1.33×10^{-26}
$\text{CH}_3\text{CHCO}^* \rightarrow \text{CH}_3\text{CH}^* + \text{CO}^*$	0.44	-1.00	2.30×10^{-12}	2.30×10^{-12}	8.05×10^{-25}
$\text{CO}_{(g)} + * \rightarrow \text{CO}^*$	0.00	-2.09	-2.75×10^{-11}	0	2.75×10^{-11}
$\text{CH}_3\text{CH}_{3(g)} + * \rightarrow \text{CH}_3\text{CH}_3^*$	0.00	0.27	-2.75×10^{-11}	0	2.75×10^{-11}
$\text{OH}^* + \text{H}^* \rightarrow \text{H}_2\text{O}^* + *$	1.14	0.56	2.75×10^{-11}	2.75×10^{-11}	4.28×10^{-23}
$\text{H}_2\text{O}_{(g)} + * \rightarrow \text{H}_2\text{O}^*$	0.00	-0.09	-2.75×10^{-11}	0	2.75×10^{-11}
$\text{H}_2^* + * \rightarrow \text{H}^* + \text{H}^*$	0.31	-0.98	-1.89×10^{-7}	1.25×10^2	1.25×10^2
$\text{H}_{2(g)} + * \rightarrow \text{H}_2^*$	0.00	-0.63	-2.68×10^{-3}	2.24×10^6	2.24×10^6

Campbell reported a method to identify the rate determining step in a reaction mechanism based on the reversibility of elementary steps, viz. the ratio of the reverse rate to the forward rate.¹⁸³ Using this approach, the adsorption of PAc on Ni[111] is determined to be a reversible step, while the dehydroxylation step is irreversible, and the α -carbon dehydrogenation of $\text{CH}_3\text{CH}_2\text{CO}^*$ has a reversibility of 0.92. From this analysis, dehydroxylation of PAc can be confirmed to be the rate determining step with a TOF of $2.75 \times 10^{-11} \text{ s}^{-1}$.

Campbell also reported that by changing the energy of a transition state and keeping the energies of all other intermediates and transition states constant, the importance of a particular transition state to the overall reaction rate can be ascertained.¹⁸³⁻¹⁸⁴ It should be noted that in this analysis, the equilibrium constant remains unchanged while the forward and reverse rate constants change. The degree of rate control for step ‘*i*’ is written as follows:

$$X_{RC,i} = \frac{\vec{k}_i}{r} \left(\frac{\partial r}{\partial \vec{k}_i} \right)_{K_{i,eq}; k_{j \neq i}}$$

where \vec{k}_i is the forward rate constant and r is the overall reaction rate. The degree of rate control analysis suggests that $\text{CH}_3\text{CH}_2\text{COOH}^*$ dehydroxylation to $\text{CH}_3\text{CH}_2\text{CO}^*$ is the rate controlling step ($X_{RC,i} = 1.0$), while all other steps had $X_{RC,i} = 0$. This is expected due to the irreversible nature of the step and all following steps were in steady state.

Since the apparent activation energy (E_{app}) depends on the reaction conditions, microkinetic modeling can be used to probe the influence of these conditions on E_{app} . In

addition, the reaction order with respect to the partial pressure of the reactants can also be estimated. Moreover, the changes in these parameters caused by variations in the reaction conditions can be employed to obtain the overall rate equation. With the aid of the Arrhenius plot in Figure 3.4, E_{app} is found to be 1.15 eV or (111.08 *kJ/mol*) for the temperature range between 473 and 673 K. For the reaction conditions used in this model, Otyuskaya and co-workers report an E_{app} of 118 *kJ/mol* (1.22 eV) which is in agreement with our model.¹⁷ A higher $E_{app} = 2.38$ eV was reported by Zare and co-workers¹⁸ on Ni[111], which could be attributed to different conditions used for microkinetic modeling and the different reaction pathway proposed by these authors. Although these results suggest an area amenable to more detailed investigation, the latter is beyond the scope of this study.

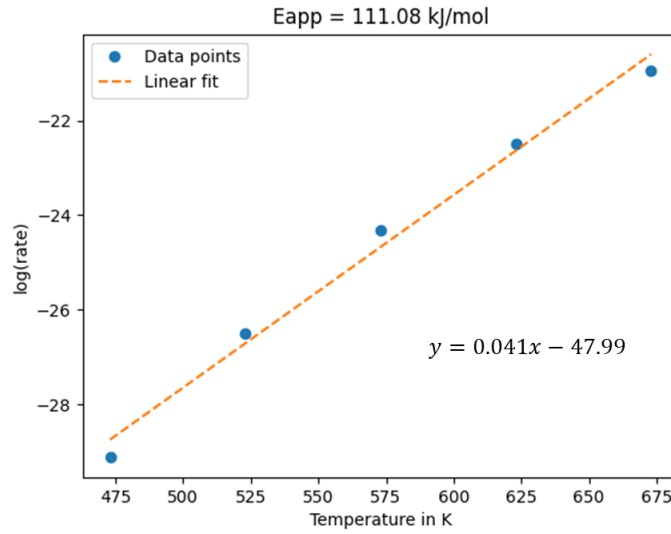


Figure 3.4 Arrhenius plot built to determine the apparent activation energy for the overall rate of the PAc DCN reaction in the 473 to 673 K temperature range.

The apparent activation energy from Campbell's degree of rate control for a reaction with two rate determining steps can be determined using the following relation:¹⁸⁵

$$E_{app} = X_{RC,1}E_1^\ddagger + X_{RC,2}E_2^\ddagger - n\theta_{MASI}H_{MASI}^g$$

where X_{RC} is the degree of rate control for the two rate determining steps, E_1^\ddagger and E_2^\ddagger are the enthalpy of formation of the transition states for the two steps, n is the number of sites involved in the elementary steps, θ_{MASI} is the fractional coverage of the most abundant surface intermediate (*MASI*) and H_{MASI}^g is the enthalpy of formation of the *MASI* from the gas phase ($X_{RC,2} = 0$ in this model). According to this relation, E_{app} for the DCN of PAc was calculated to be 0.92 eV, which is comparable to 1.15 eV calculated from the Arrhenius plot. The reaction rate with respect to H₂ and PAc partial pressure is calculated by relating the changes to the overall rate of the reaction when small changes are made to

the partial pressure of either PAc or H₂, keeping the other constant. The reaction rate with respect to H₂ partial pressure drops with an inverse order of $a_{H_2} = -2.0$ when p_{H_2} is varied from 0.1925 bar to 0.2125 bar. The reaction rate increases with PAc partial pressure with a positive order of $a_{PAc} = 2.0$ when the pressure is varied from 0.0096 bar to 0.0106 bar.

For the most dominant pathway identified in this work, the overall rate equation was derived analytically by considering the dehydroxylation step to be rate determining and all other steps as quasi-equilibrated using Langmuir–Hinshelwood-based kinetic equation.¹⁵¹ Equilibrium rate expressions for PAc and H₂ adsorption can be written as,

$$K_A = \frac{\theta_A}{p_A \theta_*}; K_{H_2} = \frac{\theta_{H_2}}{p_{H_2} \theta_*}$$

The overall rate equation can be written as the forward rate of the elementary step 3 since it is the rate determining step.

$$r_{overall} = k_1^+ \theta_* \theta_A$$

Using the site balance equation, for a transient condition where product and surface intermediates' concentrations are all zero,

$$\theta_* + \theta_A + \theta_{H_2} = 1$$

and rearranging the equilibrium constant expressions to get θ_A and θ_* in terms of partial pressures of the respective reactants and products, we obtain the overall rate expression as,

$$r_{overall} = \frac{k_1^+ K_A p_A}{(1 + K_A p_A + K_{H_2} p_{H_2})^2}$$

From the analytical expression, the reaction order with respect to surface concentration of PAc was $a_{PAc} = (1 - 2\theta_{PAc})$ and with respect to surface H_2^* is $a_{H_2} = -(2\theta_{H_2})$. This shows, under low surface concentration of PAc, the reaction is first order and at high surface concentration of H_2^* we see an inverse second order. However, using the above rate expression, the analytically determined order was $a_{PAc} = 0.99$ and $a_{H_2} = -1.51$. The deviation in the a_{PAc} from the microkinetic model to the analytical expression could be due to competitive adsorption. The expression for E_{app} determined analytically is,

$$E_{app} = E_a^{dehydroxylation} + \Delta H_{PAc}(1 - 2\theta_{PAc}) + \Delta H_{H_2}(-2\theta_{H_2})$$

where, $E_a^{dehydroxylation}$ is the activation barrier for the dehydroxylation step, ΔH_{PAc} is the enthalpy change in binding of PAc, θ_{PAc} is the surface coverage of PAc, ΔH_{H_2} is the enthalpy change in binding of H_2 , and θ_{H_2} is the surface coverage of H_2 . Note, the terms in the round brackets represent the analytical expression for the respective orders. Using this expression and the orders determined above, the analytical E_{app} was 1.10 eV, which agrees with the microkinetic model. This equation also confirms the contribution of binding energies to the apparent activation energy of the overall reaction and highlights the importance of determining the most stable binding mode of the reactant molecule. In future work, it would be warranted to include van der Waals correction to the functional used for binding energy predictions since vdW forces can influence the preferred adsorption mode of reactant molecules.¹⁶⁶⁻¹⁷⁰

3.4 Conclusion

Inexpensive Ni-based catalysts have been reported to display comparable performance to costly Pt- and Pd-based formulations in the deoxygenation of fatty acids and their derivatives to fuel-like hydrocarbons via DCN/DCX. In this contribution, a model carboxylic acid (PAC) is used as a surrogate for fatty acids to investigate the DCN reaction mechanism over a Ni[111] surface. Notably, both first-principles electronic structure calculations and *in situ* DRIFTS measurements establish that PAC predominantly adopts a bidentate binding mode on Ni[111]. Microkinetic modeling making use of DFT-determined parameters shows that PAC dehydroxylation followed by two α -carbon dehydrogenation steps of $\text{CH}_3\text{CH}_2\text{CO}^*$ intermediate to CH_3CCO^* , then the $-\text{CO}$ abstraction and ultimately hydrogenation to ethane as the dominant pathway at 573 K. The lateral interaction effect with first order approximated H^* coverage on the reaction mechanism shows an increase in the activation barriers of key elementary steps. The model also provides valuable insights on the reaction orders of the gas phase species. The pathway proposed in this contribution has a TOF of $2.75 \times 10^{-11} \text{s}^{-1}$, which is slower than the reported experimental value although, the E_{app} of 1.15 eV (0.92 eV if the value is estimated using Campbell's degree of rate control) is in reasonable agreement with experiment. The key differences between the conclusions of this contribution and those from previous reports^{15, 18-19} mainly stem from – and highlight the importance of – the agreement between DFT and experimental identification of the binding mode of reagents on transition metal surfaces. Indeed, the bidentate adsorption mode of PAC on Ni[111] spectroscopically observed in this work afforded valuable insights vis-à-vis the accessibility of α -carbon

hydrogen atoms, which in turn informed the mechanistic pathways that could possibly follow.

CHAPTER 4. IMPACT OF FLUORINATED ANILINIUM-BASED LIGANDS ON THE SURFACE ELECTRONIC PROPERTIES OF FORMAMIDINIUM TIN IODIDE (FASnI₃) PEROVSKITE

4.1 Introduction

As discussed in Chapter 1, perovskites are promising materials for a wide range of semiconducting applications, including as the active materials in solar cells, transistors, and lighting, as one can tune the material properties through modification of the bulk perovskite chemistry and structure and the surface chemistry. Here, we employ density functional theory (DFT) calculations to investigate how surface ligands impact the electronic properties of FASnI₃, with focus on the [110] surface. We are particularly interested in anilinium-based ligands that vary by the number of fluorine atoms appended to the phenyl ring. Similar ligands have been shown to offer wide variability in the surface electronic properties of indium tin oxides (ITOs)¹⁸⁶⁻¹⁹¹ and graphene oxides (GOs)¹⁹²⁻¹⁹⁴ as a function of the degree of fluorination and/or variability in self-assembled monolayers (SAMs).

We set as a baseline the structural and electronic properties of the high-temperature cubic phase of FASnI₃ (Figure 4.1 (A)) and proceed to model a clean FASnI₃[110] surface with FA-I termination. We then investigate the influence of five anilinium (An)-based ligands (An⁺, 4-FAn⁺, 2,6-FAn⁺, 3,4,5-FAn⁺, 2,3,4,5,6-FAn⁺) (see Figure 4.1 (B)) on the surface energy, relative binding energy, surface charge density difference, and work function. It was hypothesized that with changing the net dipole moment of the ligand due to fluorination of the phenyl ring of anilinium that we would observe a change in the work function, as seen for ITOs and GOs. A key finding is that the anilinium ligands with varying

degree of fluorination, in-line with similar ligands on other systems, show a correlation with the FASnI_3 -ligand surface electronic properties.

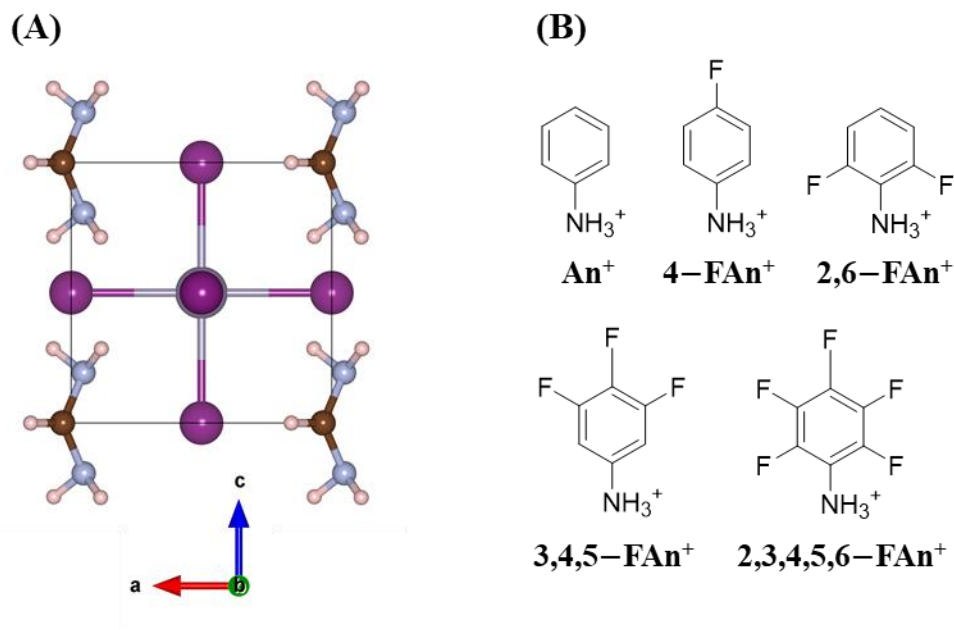


Figure 4.1 The bulk cubic structure of FASnI_3 perovskite (A) and the proposed surface ligands (B)

4.2 Methods

All DFT calculations for bulk and slab systems were carried out with the Vienna Ab-initio Simulation Package (VASP),^{157, 195} using plane-wave basis sets to solve the Kohn-Sham equations. To describe the electron-ion interactions, the projector-augmented wave (PAW) method was used, and the PBE functional within the generalized gradient approximation (GGA) was used to calculate the exchange-correlation energies.¹⁴⁵⁻¹⁴⁶ For ionic relaxations, the conjugate gradient algorithm was employed.¹⁹⁶ To account for the deficiencies in local and semi-local exchange-correlations, we used Dudarev's rotationally

invariant, simplified approach¹⁹⁷ of the DFT+U, where the Hubbard parameter (U) was empirically determined to be 6.52 eV by fitting the band gap of a periodic orthorhombic FASnI₃ unit cell to the experimentally determined band gap of 1.4 eV.^{82, 198-200} The optimized U-parameter was used in all the subsequent calculations. On-site interactions were turned on for all the *p*-orbitals of Sn. DFT-D3 dispersion corrections from Grimme's method with Becke-Johnson damping function was adopted to account for the improper description of van Der Waals interactions due to the hybrid nature of exchange-correlation functionals.²⁰¹⁻²⁰² Spin-orbit coupling (SOC) effects were considered to further account for the interaction of the electron spin with its orbital motion.²⁰³ The plane-wave energy cut-off was set to 520 eV and structures were optimized until the residual forces were smaller than 0.001 eV/Å.

We first optimized a cubic bulk structure as it provides the high temperature surface observed experimentally at 298 K.²⁰⁴⁻²⁰⁵ A (2x2) cubic, FA-I terminated FASnI₃ [110] surface consisting of four layers was constructed from the cubic bulk structure to study the surface electronic properties. The bottom two layers consisting of FA and Sn-I₃ were constrained to represent the bulk nature of the surface with the top two layers allowed to relax. A K-point mesh of 4 x 4 x 1 was used for all surface calculations. A vacuum layer of 15 Å was applied to avoid interactions between repeating units in the periodic calculations. Since the slabs generated are asymmetric, dipole corrections were applied to counteract the finite-size errors in the potential and forces. We note that attempts to use a larger vacuum space for determining the work function did not converge as they required considerable computational cost.

The ligands used for slab calculations were first optimized using the Gaussian16 (Revision A.03)²⁰⁶ software suite. The M06 functional was used for all calculations as it was developed for use with both transition metals and non-metals.²⁰⁷ The 6-31G(d,p) Pople basis set²⁰⁸⁻²¹¹ was used for all elements with an ultrafine grid for energy calculations. All ligands were optimized with a net +1 charge (except for the calculation of the net dipole moment) and normal mode analyses were carried out to ensure that no negative frequencies were present for the optimized geometries. These ligands were then used for surface calculations.

4.3 Results and Discussion

To set the stage to understand the electronic properties of An-based ligand-terminated FASnI_3 [110] surfaces, we start with a description of the bulk cubic FASnI_3 structure; we are primarily interested in the cubic (space group $Pm\bar{3}m$) phase as it is the high-temperature phase (298 K) where PSC operate.²⁰⁴⁻²⁰⁵ The lattice constant of the bulk structure was determined empirically to be 6.35 Å, which is similar to recent reports.²⁰⁴⁻²⁰⁵ A slightly indirect bandgap of 1.37 eV (see Figure 4.2) is likely due to Rashba or Dresselhaus effects, where spin-splitting occurs due to SOC.²¹²⁻²¹³ The experimental bandgap is 1.41 eV.²⁰⁰ Literature reports^{205, 212} also show via partial density of states (pDOS) that the valence band maximum (VBM) and the conduction band minimum (CBM) are predominantly dominated by the I(p) and Sn(p) states respectively, which aligns with our findings from the DOS of the bulk cubic structure of FASnI_3 as shown in Figure 4.2.

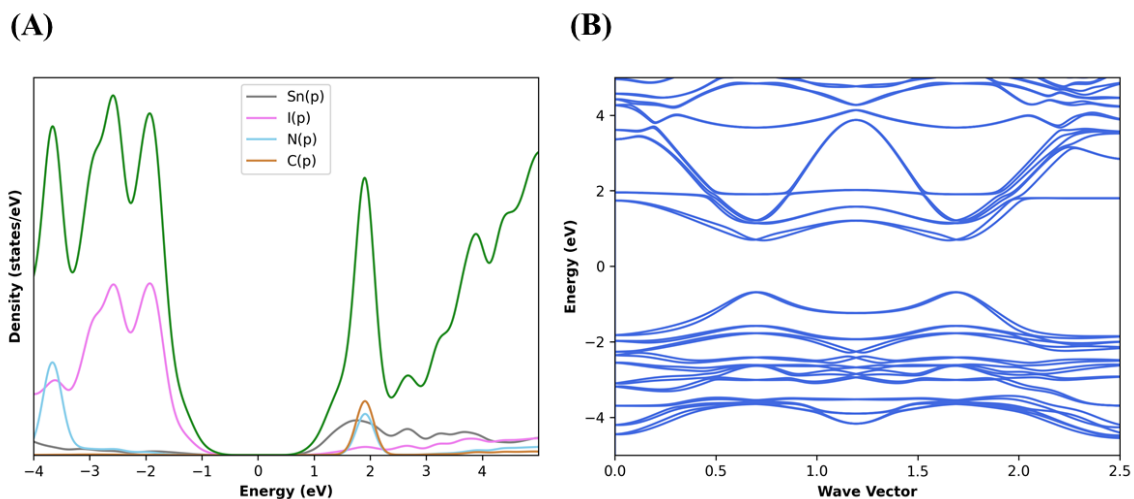


Figure 4.2 The electronic density of states (DOS) (A) and the band structure (B) of the bulk cubic FASnI₃ perovskite determined at PBE+U level of theory. The DOS shows the nature of VBM and CBM with a slight indirect bandgap of 1.37 eV shown via the band structure.

Phenyl-based ligands with varying degrees fluorination and patterns of fluorine substitution around the phenyl ring offer the ability to tune the dipole moment of the individual ligand molecules that, when aligned on a surface as a SAM, can be used to alter the material (here perovskite) work function. To explore this phenomenon, we started with the DFT determined net dipole moments for each ligand under consideration. To avoid issues with determining the dipole moments of the protonated (charged) anilinium-based ligands, we used neutral amine-based ligands as a proxy to evaluate how fluorination impacted the molecular dipole moment, shown in Figure 4.1(B). It is quite clear that the *p*-substituted aniline (An) ligands (4-FAn and 3,4,5-FAn) show the largest dipole moments (see Figure 4.3), with the 2,3,4,5,6-FAn ligand possessing a nearly identical magnitude of the net dipole moment as the 4-FAn ligand. The 2,6-FAn ligand (*m*-substituted) shows a decrease in the magnitude of the net dipole moment when compared to An.

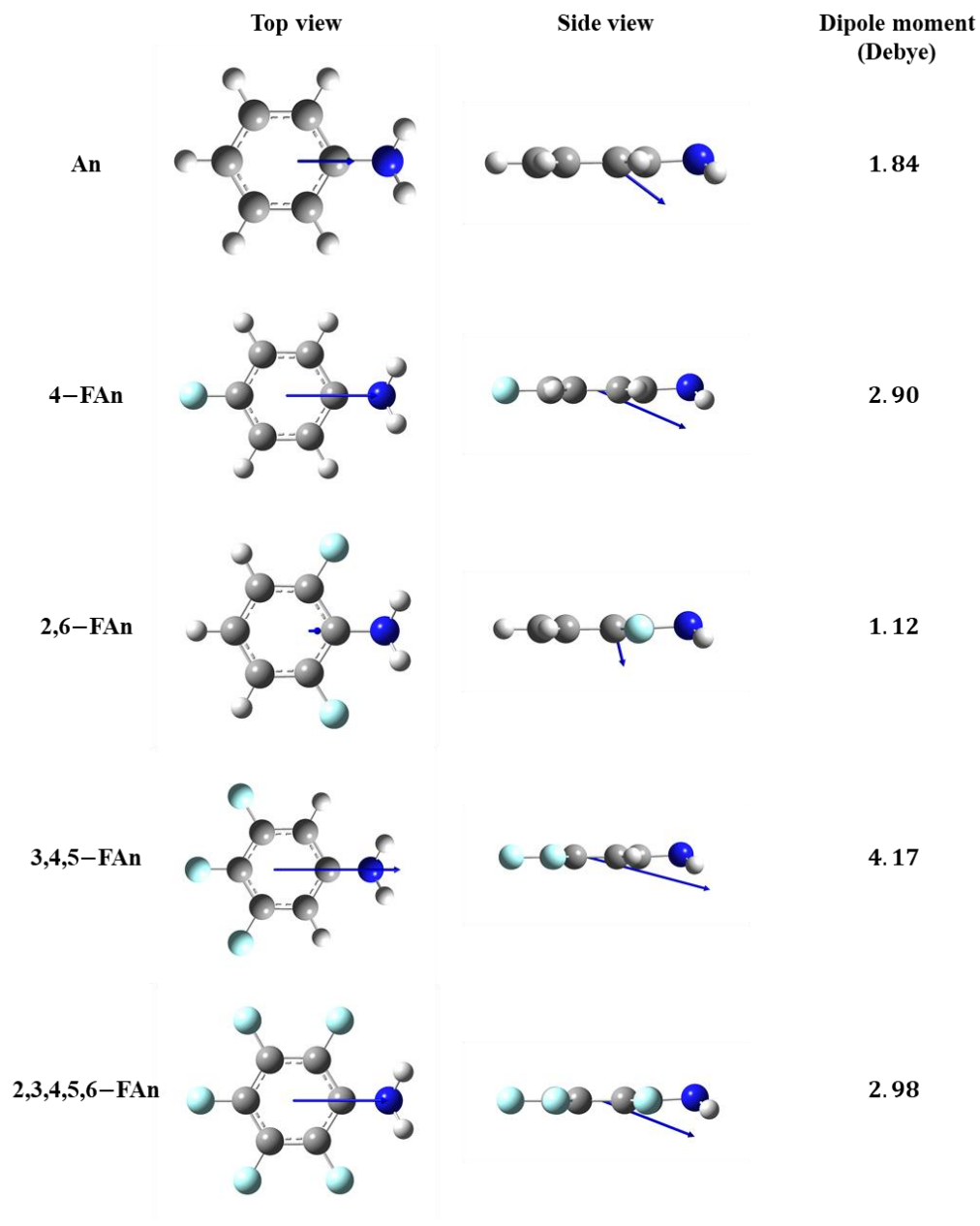


Figure 4.3 Net dipole moments of fluorine substituted Aniline (An) based ligands calculated at M06L/6-31g(d,p) level of theory.

For each ligand considered (Figure 4.1 (B)), the [110] surface was covered by one monolayer (1ML) of ligand, as shown in Figure 4.4. Several orientations for each ligand were considered, with results from the most stable configurations reported here.

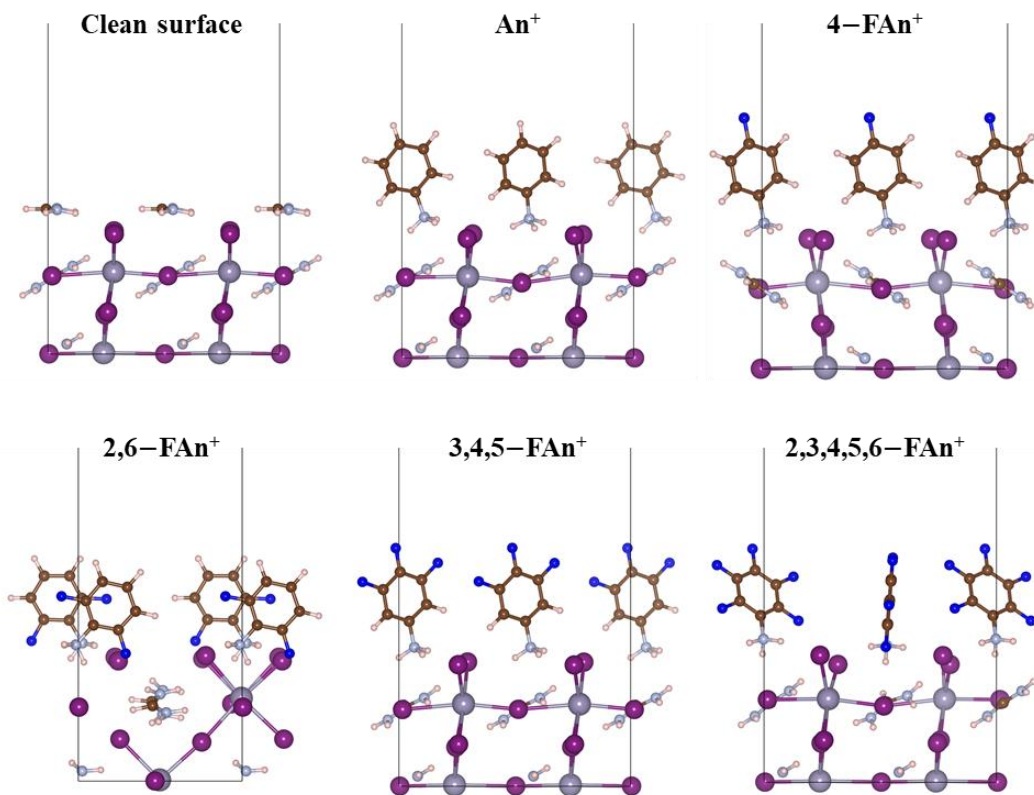


Figure 4.4 Periodic DFT optimized surfaces (side view) with 1ML coverage of each ligands. The surface structures shown here are the most stable modes.

The relative binding energy of one ion on the surface was determined in accordance with the work from Shu and co-workers⁶⁴

$$E_{ads} = \frac{(E_{perovskite/ion} - E_{perovskite} - 2E_{ion})}{2} \quad (4.1)$$

where $E_{perovskite/ion}$ is the total DFT energy of the perovskite surface with 1 ML of the respective ion on the surface, $E_{perovskite}$ is the total DFT energy of the clean perovskite surface, E_{ion} is the DFT energy of the isolated ion in the gasphase, and the normalizing factor 2 accounts for per ion basis of the adsorption energy. An^+ and its derivatives bind strongly when compared to the surface FA^+ cations with the exception of 2,3,4,5,6- FAn^+ . The result for 2,3,4,5,6- Fan^+ , which has a binding energy similar to FA^+ , is likely due to strong and repulsive intermolecular F-F interactions among the closely packed ligands on the surface. We hypothesize that this result may also be in part due to the over-penetration of the 2,3,4,5,6- FAn^+ ligands into the surface. To investigate this, we examined the geometric effects of ligand binding on the surface of the perovskite. Although there is some distortion in the $\angle I-Sn-I$ $\angle Sn-I-Sn$ angles, a direct correlation to the relative binding energy cannot be made. The distance between the N-atom of the amine group and the I-atom underneath on the surface of the perovskite suggests excessive penetration of the 2,3,4,5,6- FAn^+ ligand, which has been shown to destabilize the $MAPbI_3$ perovskite surface.⁶³ Further investigation is needed to better understand this behavior.

The surface energy (in eV/Å), which is a metric to understand surface stabilities, is determined by

$$\gamma = \frac{(E_{DFT}^{slab} - nE_{DFT}^{bulk})}{2S} \quad (4.2)$$

where E_{DFT}^{slab} is the total DFT energy (in eV) of the slab, n is the number of repeat units (four unit cell repeats to construct the slab), E_{DFT}^{bulk} is the DFT energy (in eV) of the bulk structure, S is the total area of the surface in \AA and the normalizing factor as it provides energy per surface since the slab termination has two surfaces along the z-axis.

Table 4.1 Surface energy, relative binding energy, work function, N–I distance, $\angle\text{I–Sn–I}$ and $\angle\text{Sn–I–Sn}$ of periodic surfaces at PBE+U level of theory.

Surface	Surface energy (γ) (eV/ \AA)	Relative Binding energy ($\Delta\text{B.E.}$) (eV)	Relative Work function ($\Delta\Phi$) (eV)	N–I distance (\AA)	$\angle\text{I–Sn–I}$	$\angle\text{Sn–I–Sn}$
Clean	−0.14	0.00	0.00	3.81	92.7°	170.3°
An ⁺	−0.98	−0.47	−0.56	3.54	89.5°	164.4°
4–FAn ⁺	−0.98	−0.48	0.19	3.55	87.2°	164.6°
2,6–FAn ⁺	−0.98	−0.46	−0.73	3.42	87.1°	158.7°
3,4,5–FAn ⁺	−0.98	−0.25	0.86	3.46	87.7°	168.6°
2,3,4,5,6–FAn ⁺	−0.97	0.07	0.40	3.40	91.4°	162.4°

Hydrophobic materials have lower surface energy (γ) than hydrophilic materials, and when two materials with different γ are mixed to form a layer, the material with low γ tends to be distributed at the surface.²¹⁴ It should be noted that the surface energy calculation is not straightforward for asymmetric slabs where the chemical characteristics

of the top and bottom surfaces differ, which is the case here. To circumvent this problem, we first calculated the surface energy of the clean slab (γ_{surf}) using equation (4.2) and used equation (4.3) to calculate the surface energy at the top of the slab for all the surfaces with 1ML coverage of An^+ and its derivatives.

$$\gamma = \left[\frac{(E_{DFT}^{slab} - nE_{DFT}^{bulk})}{S} \right] - \gamma_{surf} \quad (4.3)$$

The first term in the bracket is the total surface energy of the slab consisting of two (top and bottom) surfaces, which is subtracted by the surface energy of the bottom surface which is equivalent to the clean slab.

We note that lower surface energies due to the presence of SAM on perovskite surfaces has been shown to increase hydrophobicity and improve PCEs.^{64, 68-69} Qualitatively, the results presented here are in line with literature precedent. However, negative surface energies indicate that the bulk system would spontaneously disintegrate. There are several reasons that can lead to negative surface energies, such as the reference chosen to calculate the surface energy likely does not account for the asymmetric nature of the bottom and top surfaces of the slab. Although the γ_{surf} is subtracted in the equation (4.3), the calculation of γ_{surf} is based on the relaxed surface while the bottom surface of the slab models in Figure 4.4 are constrained for bulk representation. Another problematic aspect could be due to the nature of the bulk calculation, where it is likely that the structure resides at a local minima and not the global minima on the potential energy surface. It is imperative to further investigate these concerns and efforts are underway.

The work function can be used to understand the influence of ligands on the electronic properties of perovskites. The work function represents the photon energy needed to displace an electron from the bulk of a crystal to the vacuum region where the influence from the crystal surface is negligible.²¹⁵ The work function is calculated as

$$\phi = E_{vac} - E_{fermi} \quad (4.4)$$

where, E_{vac} is the vacuum potential, E_{fermi} is the Fermi energy.

From Table 4.1, we see that the substitution of surface FA⁺ with An⁺ reduces the work function by -0.56 eV, where the relative work function is with respect to the work function of the clean slab (FA-I terminated). Further, the subsequent fluorination of the phenyl ring to 4-FAn⁺ increases the work function substantially by -0.19 eV relative to the clean slab. Notably, fluorinating the phenyl ring at the 2,6-position decreases the relative work function substantially, while 3,4,5-FAn and 2,3,4,5,6-FAn substitutions increases the relative work function (see Table 4.1 and Figure 4.5). This behavior is in-line with observations of similar ligands on ITO and graphene that show a change in work function of up to 1.2 eV.^{186, 188} However, it should be noted that the mechanism of surface modification in those studies were either through physisorption or chemisorption while this work pertains to surface substitutions.

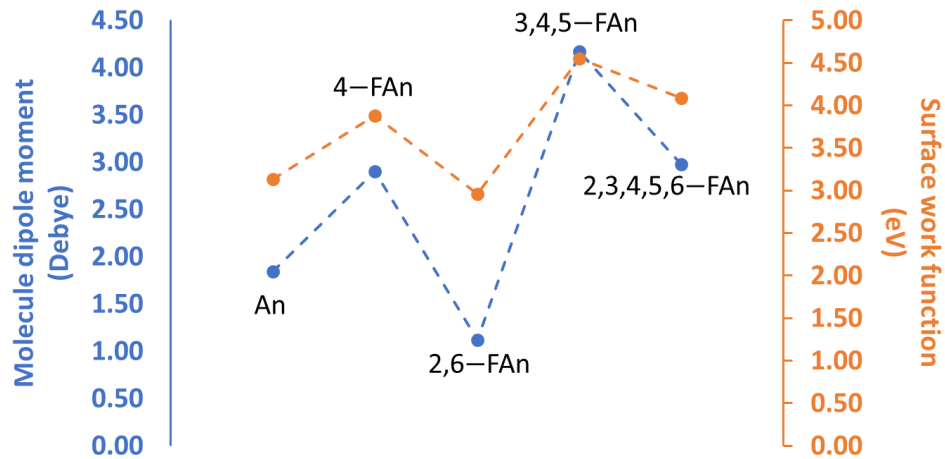


Figure 4.5 Correlation diagram of net molecular dipole moment and the surface work function.

Since the work function depends on the Fermi energy of the surface and the vacuum potential, it is worthwhile to understand their dependence on the net dipole moment of the isolated ligands (see Figure 4.6). Although it should be noted that the surface dipoles can vary from the net dipole moment of isolated ligands and a direct correlation cannot be made, we can make observations on the dependence of E_{vac} and E_{fermi} on the surface orientation of ligands (in particular, the fluoride pointing towards or away from the surface).

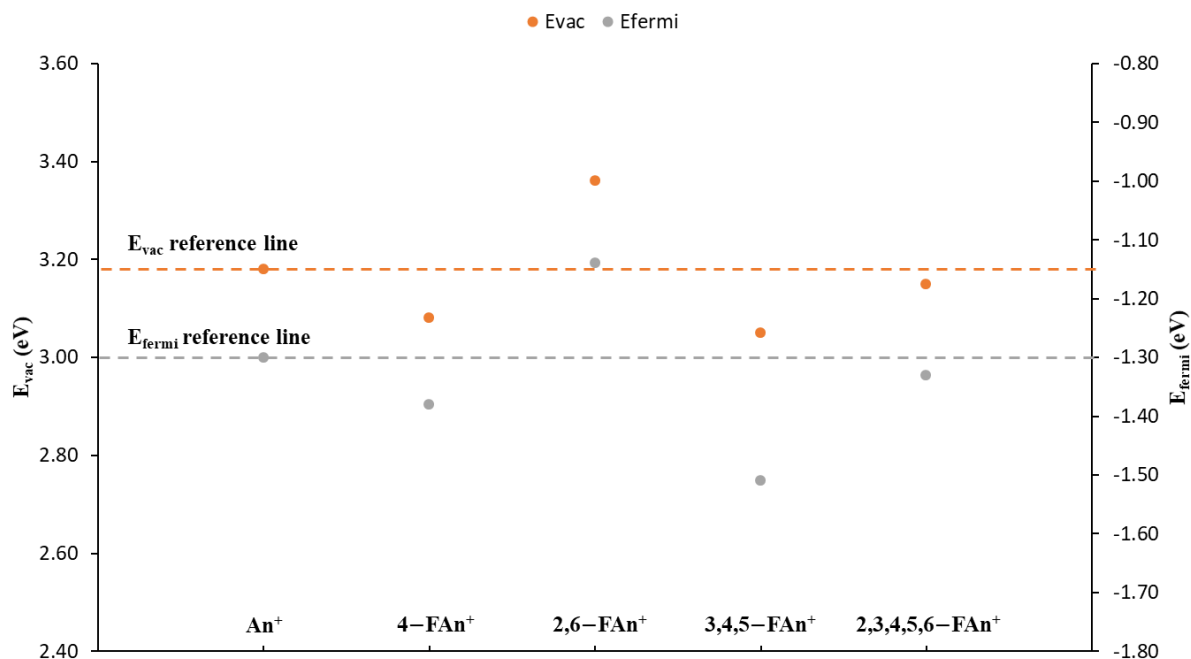


Figure 4.6 Vacuum potential and the fermi energy for 1ML coverage of An^+ and its fluorinated derivatives. The reference line chosen is with respect to An^+ on the surface.

From Figure 4.6, we observe that the E_{vac} and E_{fermi} are almost linearly dependent with respect to fluorination of the An^+ ligand for a monolayer. We do observe changes in E_{fermi} and E_{vac} show a reasonable dependence on the ‘net’ direction of $-F$ on the surface monolayer. For the case of 2,6-F An^+ , we see from Figure 4.4 that the F atoms point towards the surface and is the only case where there are no F atoms pointing away from the surface, which results in an increase in the E_{fermi} and E_{vac} . Whereas for all other fluorinated An^+ cases, we observe a decrease in E_{fermi} and E_{vac} with respect to 1ML An^+ on the surface. This result shows the effect of surface geometry on the Fermi energy and vacuum potential are correlated and it is reflected in the change of work function as a function of net molecular dipole moments.

Charge density difference ($\Delta\rho$) plots were examined to study the interaction of the ligands with the perovskite surface where, the $\Delta\rho$ was determined by⁶⁴

$$\Delta\rho = \rho_{slab}^{interface} - \rho_{slab}^{ions} - \rho_{slab}^{perovskite}$$

where, $\rho_{slab}^{interface}$, ρ_{slab}^{ions} , $\rho_{slab}^{perovskite}$ is the charge density of the perovskite–ion interface, ions on the slab and the bare perovskite respectively. Several works on metal HPs (ABX_3) have shown that the bandgap and in-turn, the work function, can be tuned by varying the ionic character of the $B-X$ bond.^{77, 216-219} From these works, it is evident that the electronegativity of the metal ($B=Sn$) shows a correlation with the respective perovskite work function.

The charge density difference plots are shown in Figure 4.7, where the yellow region shows charge accumulation and the blue region shows charge depletion. Interestingly, the interaction between the ligand and the perovskite surface is stronger for the case of An^+ and its derivatives, which is shown by the increased volume of charge accumulation and depletion regions for these surfaces when compared to the clean surface. Prior studies have demonstrated stronger interaction and higher surface stability with increasing volume of charge accumulation and depletion regions.^{64, 220} This behavior is in line with the N–I distance observed for each ligand on the surface (see Table 4.1) where stronger interactions result in shorter N–I distance. A closer look at the charge density difference (Figure 4.8) reveals the nature of the interaction to be very similar for all ligands regardless of the extent of fluorination. The amine group of the ligand shows considerable charge depletion. To balance the charge distribution, we observe accumulation on the

phenyl ring and the surface iodine atoms. Due to charge accumulation on the iodine atoms, a small region of charge depletion is observed between the Sn–I bond that results in charge accumulation on the Sn atom. This behavior is consistent with all the surfaces under consideration, regardless of the type of ligand on the surface. The charge accumulation on Sn makes it more electronegative, resulting in lowering of the ionic character of the Sn–I bond with stonger antibonding coupling. Shi and co-workers⁸⁰ studied this behavior in MASnI₃ and FASnI₃ where they observed a higher antibonding coupling between Sn(5s) and I(5p) in MASnI₃, which resulted in lower PV performance when compared to FASnI₃. Therefore, it is necessary to change the ionic character of the *B* metal by increasing or decreasing the antibonding coupling of the metal-halide bond in the perovskite structure to significantly change the work function of the material. Since An⁺ and its fluorinated derivatives interact strongly with the perovskite surface, the likely change in the ionic character of the Sn atom remains more or less the same for all the surfaces and is likely responsible for changes in the work function (as shown by the charge density difference plots in Figure 4.7 and Figure 4.8).

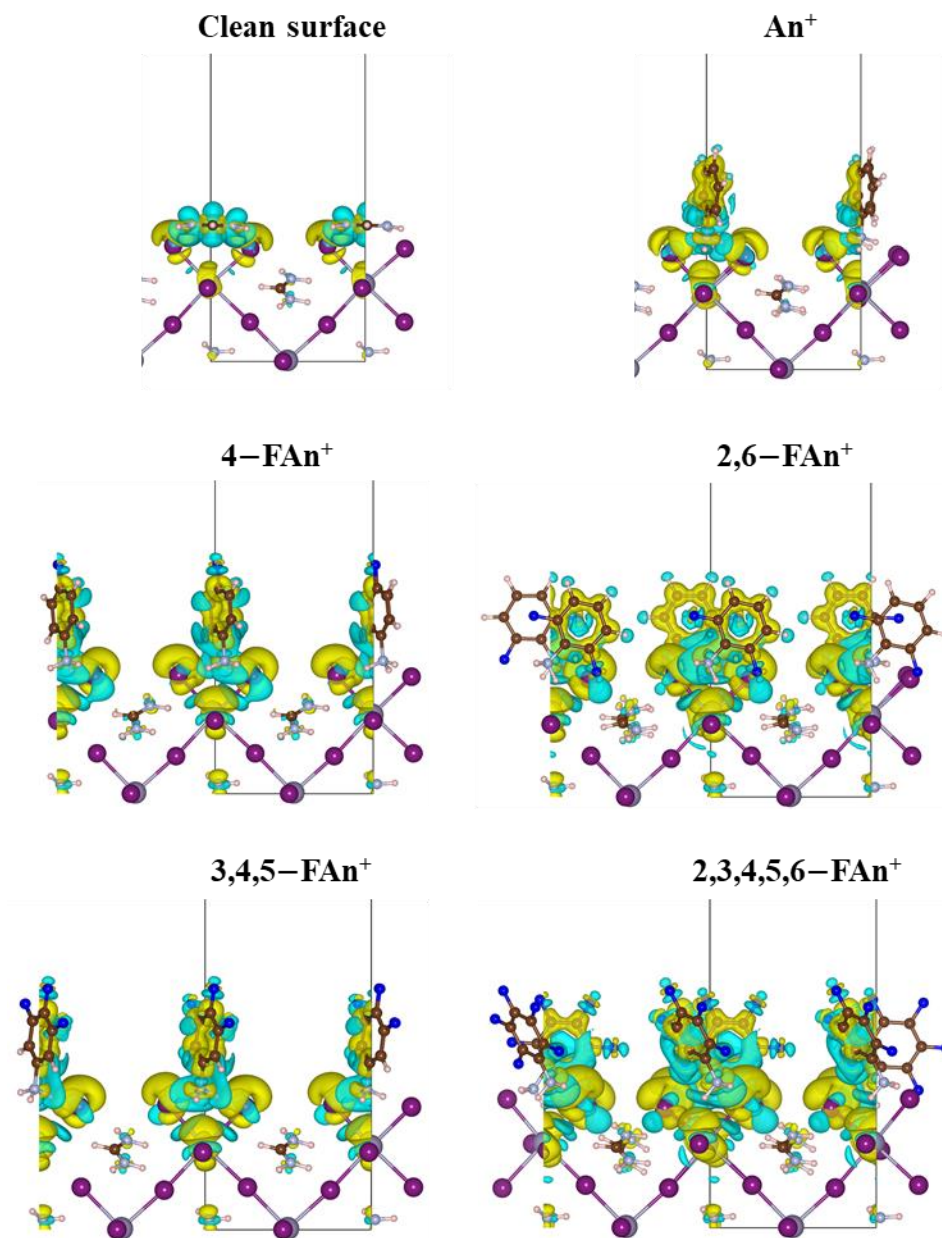


Figure 4.7 Charge density difference plots (side view) of periodic surfaces at PBE+U level of theory where, the yellow and blue regions represent charge accumulation and depletion respectively.

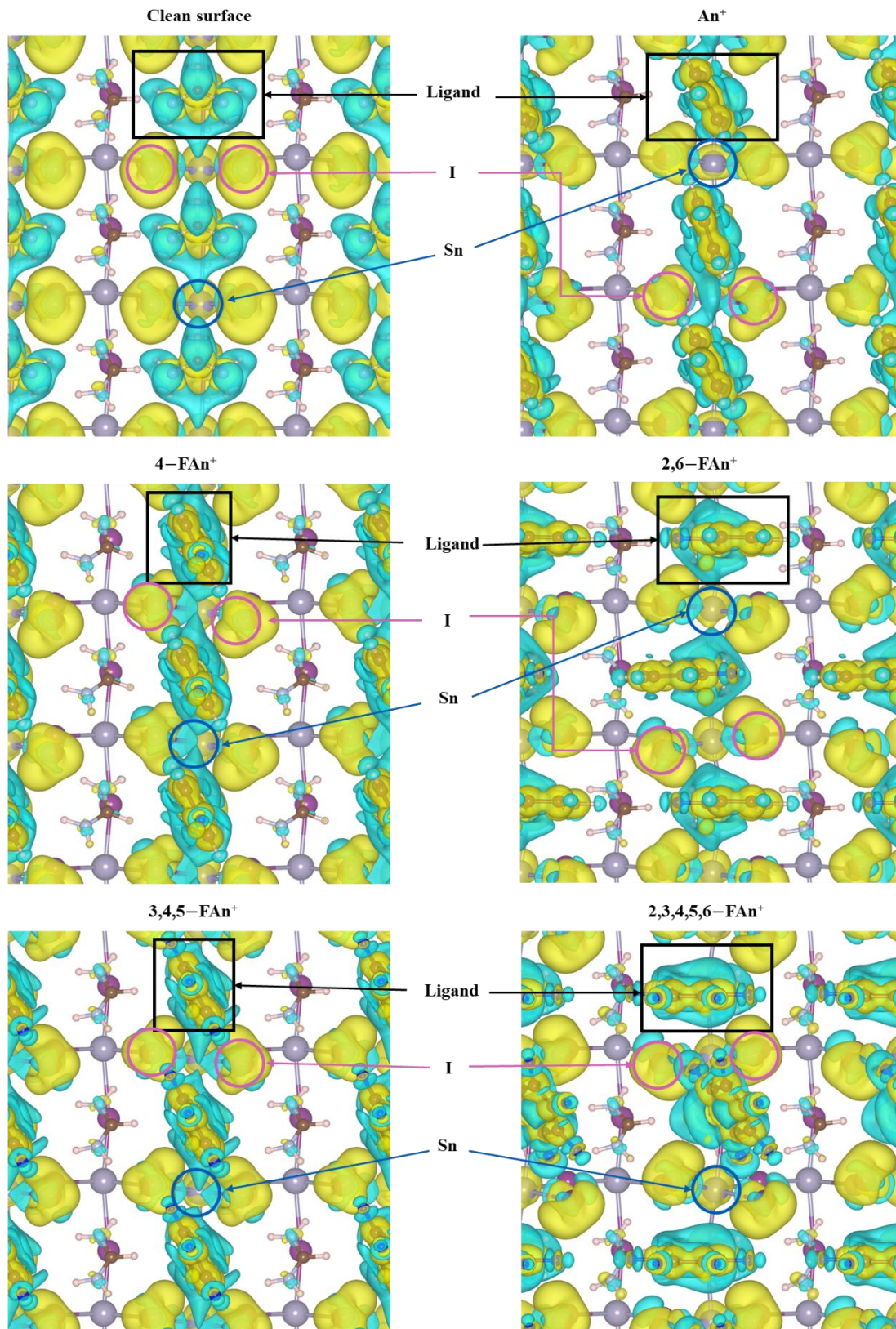


Figure 4.8 Charge density difference plots (top) view of clean surface and 1ML of An^+ and its fluorinated derivatives. The figure depicts the regions of charge accumulation (yellow) and depletion (blue) on the ligands, Sn and I atoms.

4.4 Conclusion

Perovskites demonstrate immense potential as alternatives to silicon for semiconductor applications. Due to their chemical structure and composition, they possess drawbacks that limit large-scale application. In this work, we employed DFT calculations to explore some of the proposed ligands that are known to passivate the oxidation of the Sn^{2+} to Sn^{4+} in the perovskite structure. In particular, we studied the bulk properties of cubic FASnI_3 perovskite and surface electronic properties of [110] FA–I terminated perovskite slab. The geometric structure calculations showed that substitution of surface FA^+ cations with An^+ and its fluorinated derivatives greatly reduced the surface energy of formation, indicating a more stable surface structure. An^+ and its fluorinated derivatives bind stronger than FA^+ cations to the perovskite surface except for 2,3,4,5,6– FA^+ cation, likely due to the extent of ligand penetration. Since the net dipole moment of An^+ can be varied via fluorination of the phenyl ring, its effect on the work function was studied. A clear correlation was established between the change in the net molecular dipole moment and the work function of the surface structures. The charge density difference plots showed larger volume of charge accumulation and depletion regions that explain the stronger binding of these ligands to the perovskite surface making them more hydrophobic. Understanding this behavior can lead to effective design of the perovskite surface to tune the work function and control the surface electronic properties.

CHAPTER 5. DFT STUDIES OF CO₂ REDUCTION USING N-ANNULATED PERYLENE DIIMIDE RHENIUM BIPYRIDINE DYADS

5.1 Introduction

In Chapter 1, the need for a theoretical understanding of the role of a chromophore in the electrocatalytic reduction of CO₂ was presented. Dr. Gregory Welch's group at the University of Calgary, studied the properties of N-annulated perylene diimide (PDI) and demonstrated the stability of these films in polar and non-polar solvents due to π - π stacking and suggested its function as an electron transport layer.²²¹ They also observed lowering of CO₂ reduction overpotentials when the Re(bpy) catalyst is tethered to PDI.¹¹²

The computational work presented in this chapter was carried out in collaboration with Dr. Welch's group and is published.^{112, 221} Here, we will focus on examining the frontier molecular orbitals (FMOs) of PDI and discuss its applicability to CO₂ reduction catalysts. We will then proceed to study the geometric and electronic properties of the Re(bpy-C2-PDI) catalyst. In particular, the FMOs and spin densities of each reduced specie are examined to elucidate the role of PDI tethered to the catalyst. The active intermediate in the catalytic cycle is identified and its presence and influence are demonstrated at high and low overpotentials using the FMOs.

5.2 Methods

Density functional theory (DFT) and time-dependent DFT (TDDFT) calculations were carried with in the Gaussian16 (Revision A.03)²⁰⁶ software suite. The M06 functional was used for all calculations as it was developed for use with both transition metals and non-metals.²⁰⁷ The 6-31G(d,p) Pople basis set²⁰⁸⁻²¹¹ was used for all non-metal elements,

and the LANL2DZ basis set²²²⁻²²⁴ was used for Re, with 60 core electrons subsumed into the effective core potentials. For all optimized geometries, normal mode analyses were carried out to ensure that no negative frequencies were present. To reduce computational cost, all terminal N-alkyl groups were truncated to methyl groups. For highly charged species, full convergence was first obtained by using the loose criteria for convergence, followed by the tighter, default grid. In addition to this, the NoSymm tag was used for initial convergence of the -3 charged species and then removed to attain full convergence. Molecular orbitals and spin densities were visualized using GaussView 5.0.9.²²⁵

The SMD implicit solvation model²²⁶ was used to compute the fixed concentration free energies of solvation of PDI and PDI^- in 1-propanol. The combination of computed free energies and gas phase energies were employed to determine the pK_a using methods described by others.²²⁷⁻²³² TDDFT calculations provided the excited-state transitions up to 10 states and the simulated absorption spectrum of PDI and PDI^- .

5.3 Results and discussion

PDI molecules are known to self-assemble into strongly overlapping π -stacks which makes this chromophore appropriate for electron transport materials.²³³⁻²³⁵ In addition to its well explored transport properties, understanding its ability to solubilize when deprotonated can render this material as synthetically versatile for a potential chromophore tethered to $\text{Re}(\text{bpy})$ catalysts.¹²³⁻¹²⁶

5.3.1 Electronic and optical properties of PDI and PDI⁻

Select frontier molecular orbitals (MOs) for PDI and the deprotonated PDI⁻ anion are shown in Figure 5.1. The highest-occupied MO (HOMO) and lowest-unoccupied MO (LUMO) for both species maintain similar spatial distribution, as expected. The pyrrolic N-atom of the PDI molecule is depicted in Figure 5.2. Deprotonation of PDI to form the PDI⁻ anion results in a considerable energetic destabilization of both the HOMO (from -6.17 eV in PDI to -2.84 eV in PDI⁻) and LUMO (from -3.11 eV in PDI to +0.03 eV in PDI⁻). Notably, the HOMO-LUMO gap of PDI⁻ is 0.19 eV smaller than that of PDI.

The smaller HOMO-LUMO gap for PDI⁻ correlates well with the smaller S₀→S₁ vertical transition for PDI⁻ (2.32 eV) compared to PDI (2.61 eV) as determined by TDDFT calculations at the M06/6-31G(d,p) level of theory. Both S₀→S₁ transitions are described by a one-electron excitation from HOMO→LUMO (95% electronic configuration for PDI⁻, and 98% electronic configuration for PDI). The simulated absorption spectra based on the TDDFT calculations correlate well with the experimental UV/vis spectra (Figure 5.3) suggesting dissolution of the deprotonated PDI⁻ which adds a lone pair of electrons to the pyrrolic N-atom, subsequently destabilizing the HOMO and LUMO energies.²²¹

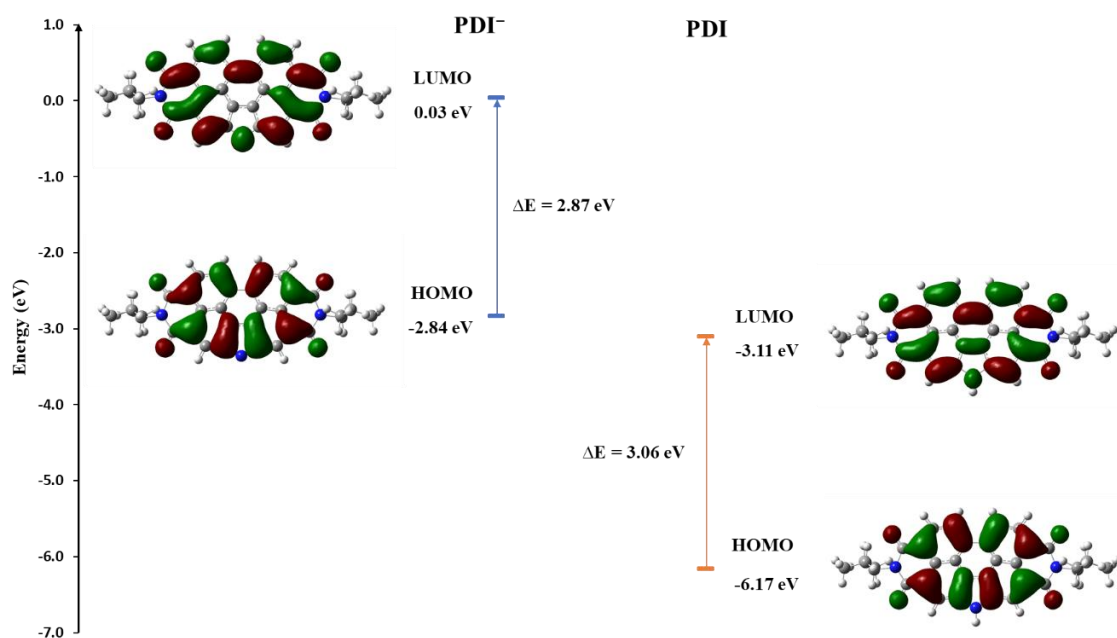


Figure 5.1 Pictorial representations of select frontier molecular orbitals (MO) for PDI⁻ and PDI as determined at the M06/6-31G(d,p) level of theory.

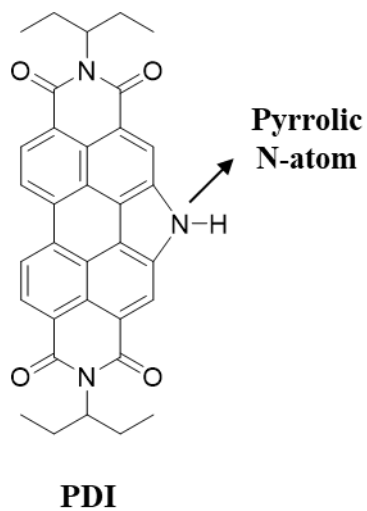


Figure 5.2 Pyrrolic N-atom of the PDI molecule.

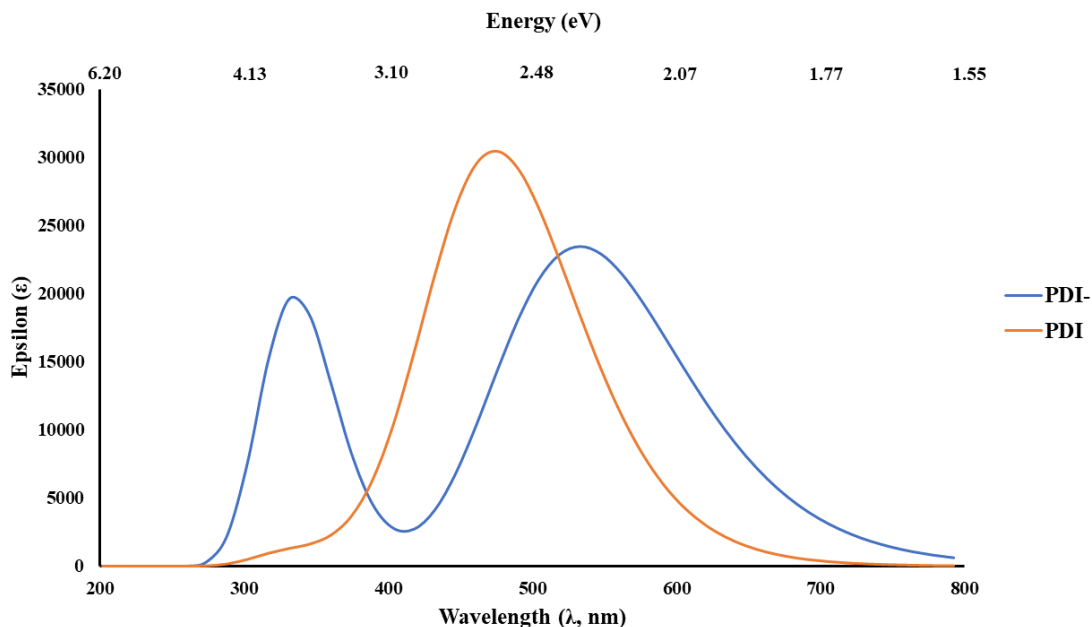


Figure 5.3 Simulated absorption spectra for PDI⁻ and PDI as determined via TDDFT calculations at the M06/6-31G(d,p) level of theory. The full width at half-maximum (fwhm) used in the gaussian convolution of the vertical excited states was 0.33 eV.

These results show that the FMO energy levels of PDI upon deprotonation is slightly destabilized which improves the energetic match with the FMOs of Re(bpy) moiety and allows for tethering the PDI to the Re(bpy) catalyst.^{112, 126, 221} In addition, the DFT predicted *pKa* of the PDI molecule in the implicit solvent 1-propanol was estimated to be 19.70, which confirms deprotonation of the molecule in basic medium as suggested by experiments.²²¹ And, as stated in Chapter 1, the deprotonated pyrrolic N-atom is well explored to tether PDI to organic solar cells and OFETs and has been explored for the Re(bpy) catalyst in this study.^{112, 123-126, 221}

5.3.2 Investigation of CO₂ reduction mechanism using Re(bpy-C2-PDI)

All optimized geometries described herein were determined to be minima on the potential energy surface through normal mode analyses. The DFT-optimized structure of neutral-state Re(bpy-C2-PDI) (see Figure 5.4) showed excellent correlation with the single-crystal X-ray diffraction connectivity map.¹¹² A molecular orbital (MO) diagram of Re(bpy-C2-PDI) (Figure 5.5), constructed using the optimized geometries of Re(bpy-TAz) and PDI, also correlated well to the electrochemically determined redox events.¹¹² The localized nature of the frontier MOs revealed that the two fragments were nearly electronically isolated, which is reasonable considering the system is not conjugated through π -orbitals. We note that in the optimized ground-state geometry of the complex that the PDI and Re(bpy-TAz) were near each other, with the alkyl arm folded to bring the moieties in proximity. All attempts to optimize the geometry of Re(bpy-C2-PDI) starting from an extended conformation were unable to deliver an optimized structure, confirming intramolecular folding is important to this system.

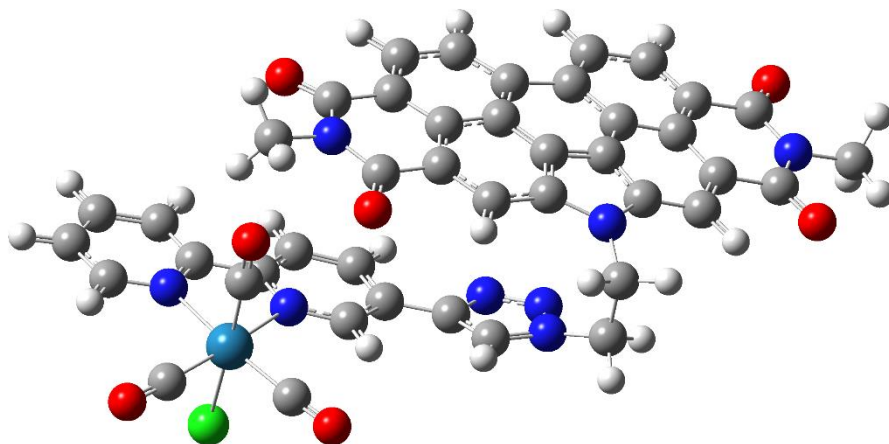


Figure 5.4 DFT-optimized structure of ground-state Re(bpy-C2-PDI) determined at M06/6- 31G(d,p)/LANL2DZ level of theory.

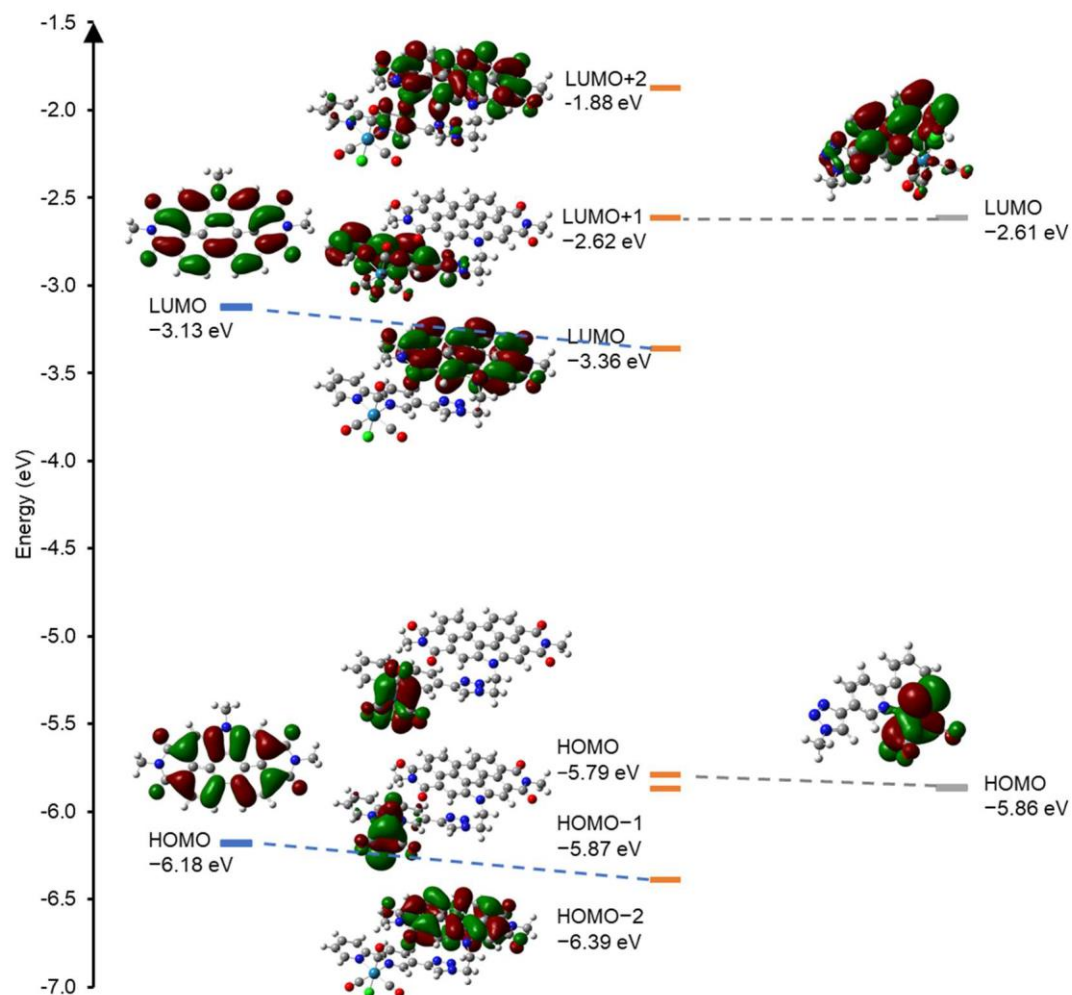


Figure 5.5 Molecular orbital diagram of Re(bpy-C2-PDI) (center), comprised of N-annulated PDI (left) and Re(bpy-TAz) (right) as determined at the M06/6-31G(d,p)/LANL2DZ level of theory.

We next turned our attention to the nature of the electronic states to propose a catalytic cycle (Figure 5.6). Emphasis was placed on the optimized geometries, frontier MOs, and spin-density maps to demonstrate the distributions of the electron spin in open-shell states. From the ground-state $\text{Re}^{\text{I}}(\text{bpy-C2-PDI})^0$ (Figure 5.6A), two electrons can be added to the system without significantly affecting the molecular geometry of the complex

(Figure 5.7 to Figure 5.11). While both the singlet $\text{Re}^{\text{I}}(\text{bpy-C2-PDI}^{2-})$ and triplet $\text{Re}^{\text{I}}(\text{bpy}^{\bullet-}\text{-C2-PDI}^{\bullet-})$ states were considered, it was found that an unrestricted open-shell calculation for doubly reduced dyad converged with all electrons paired on PDI. Given that the doubly reduced product was diamagnetic and no $\Delta\nu_{\text{CO}}$ was observed in the FTIR SEC experiments,¹¹² it is highly likely that singlet state $\text{Re}^{\text{I}}(\text{bpy-C2-PDI}^{2-})$ is favored. This notion was further substantiated by comparing the MOs of the singlet and triplet states, where $\text{Re}^{\text{I}}(\text{bpy-C2-PDI}^{2-})$ exhibited no $\text{Re-C}\equiv\text{O}$ anti-bonding character (Figure 5.11) and $\text{Re}^{\text{I}}(\text{bpy}^{\bullet-}\text{-C2-PDI}^{\bullet-})$ showed significant $\text{Re-C}\equiv\text{O}$ anti-bonding interactions (Figure 5.10).

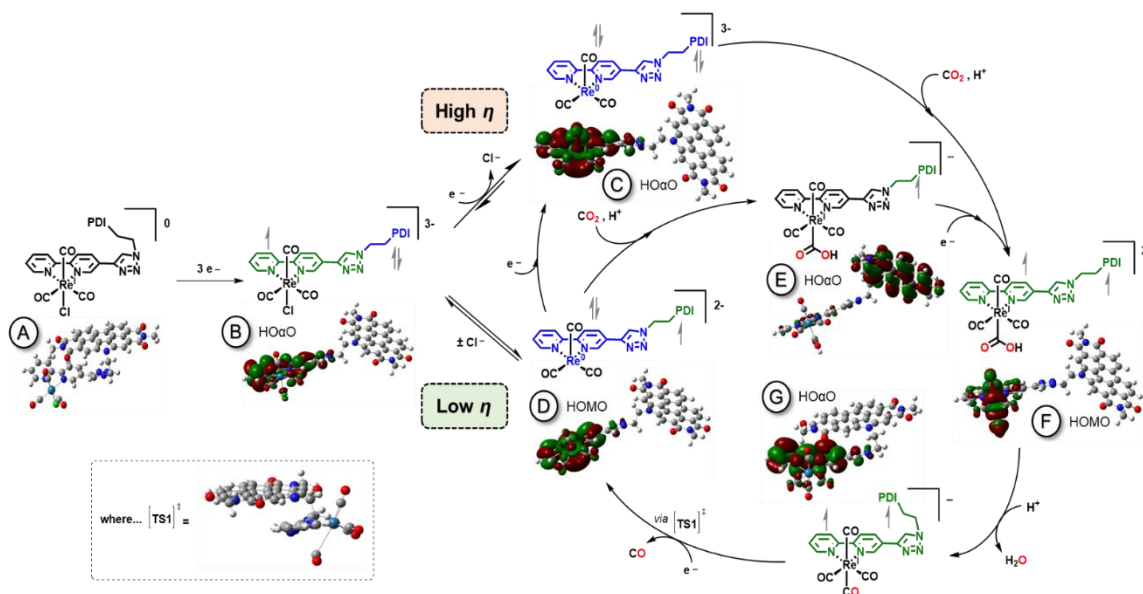


Figure 5.6 Proposed electrocatalytic CO_2 reduction cycle of $\text{Re}(\text{bpy-C2-PDI})$. Optimized geometries and relevant HOMO or $\text{HO}\alpha\text{O}$ calculations were determined at the M06/6-31G(d,p)/LANL2DZ level of theory. Black, green, or blue coloration of the $\text{Re}(\text{bpy-TAz})$ and PDI structural moieties indicate the presence of zero, one, or two electrons, respectively.

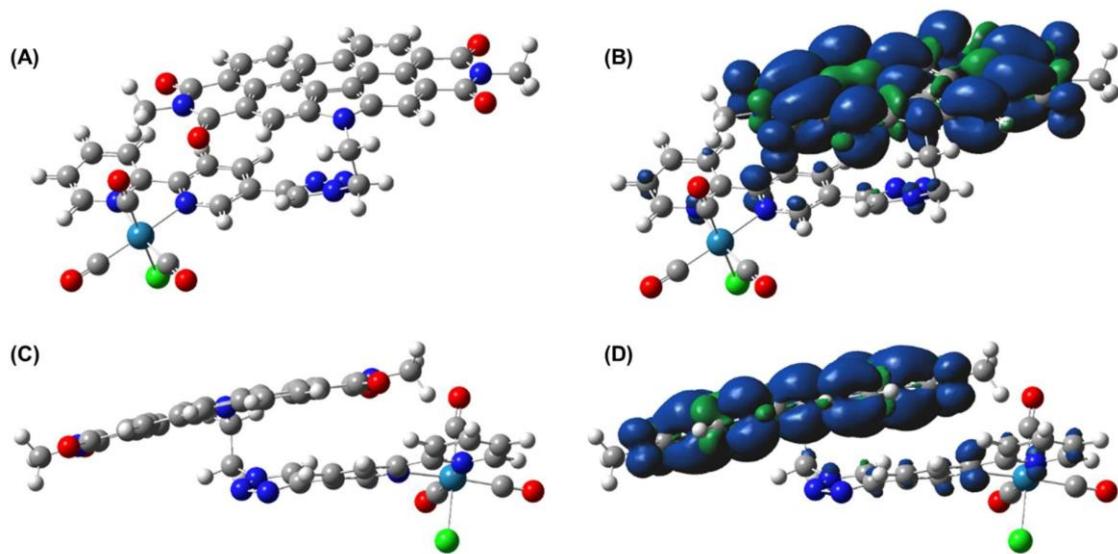


Figure 5.7 Face-on and side-on perspectives of the optimized geometry (A & C) and spin density map (B & D) for the doublet state of $\text{Re}^{\text{I}}(\text{bpy-C2-PDI}^{\bullet-})$ as determined at the M06/6- 31G(d,p)/LANL2DZ level of theory.

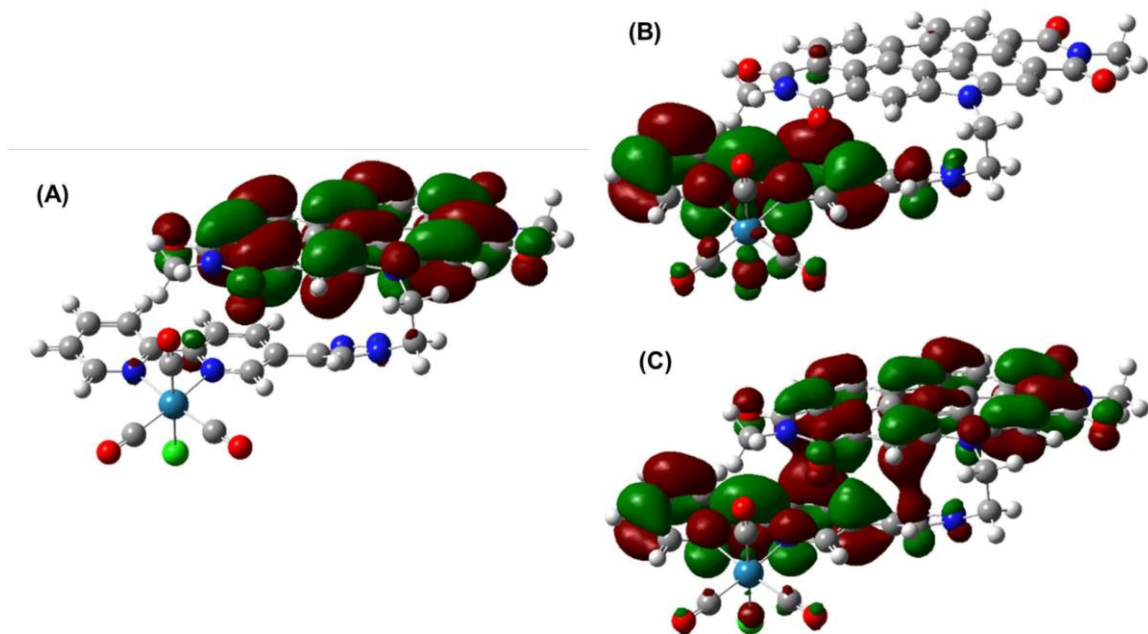


Figure 5.8 Frontier molecular orbitals of the doublet state of $\text{Re}^{\text{I}}(\text{bpy-C2-PDI}^{\bullet-})$ at the M06/6-31G(d,p)/LANL2DZ level of theory, where (A) represents $\text{HO}\alpha\text{O}$ and (B & C) represent the $\text{LU}\alpha\text{O}$ and $\text{LU}\beta\text{O}$ with α - and β -spins, respectively.

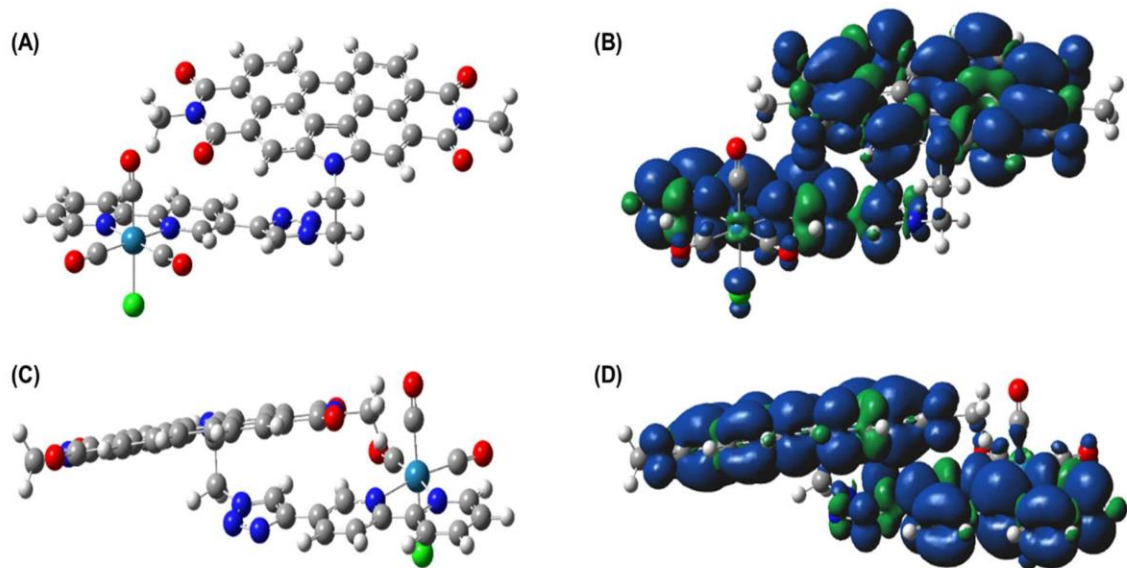


Figure 5.9 Face-on and side-on perspectives of the optimized geometry (A & C) and spin density map(B & D) for the triplet state of $\text{Re}^1(\text{bpy-C2-PDI}^{2-})$ as determined at the M06/6-31G(d,p)/LANL2DZ level of theory.

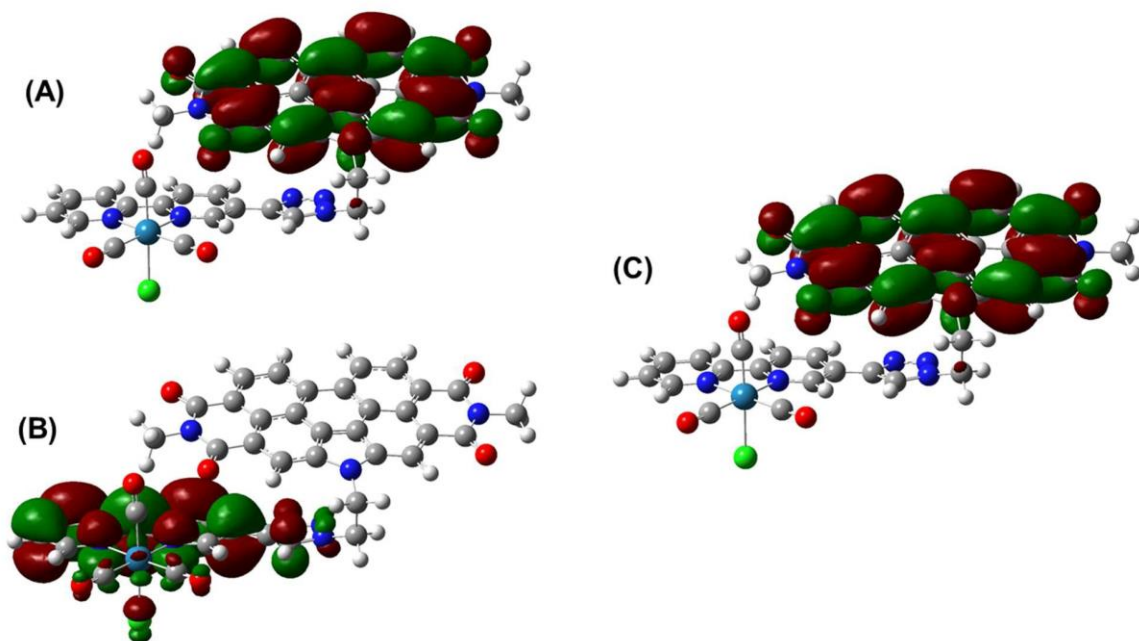


Figure 5.10 Frontier molecular orbitals of the triplet state of $\text{Re}^{\text{I}}(\text{bpy-C2-PDI}^{2-})$ at the M06/6-31G(d,p)/LANL2DZ level of theory, where (A & B) represent the $\text{HO}\alpha\text{O-1}$ and $\text{HO}\alpha\text{O}$ with α -spins, respectively, and (C) is the $\text{LU}\beta\text{O}$ with β -spin.

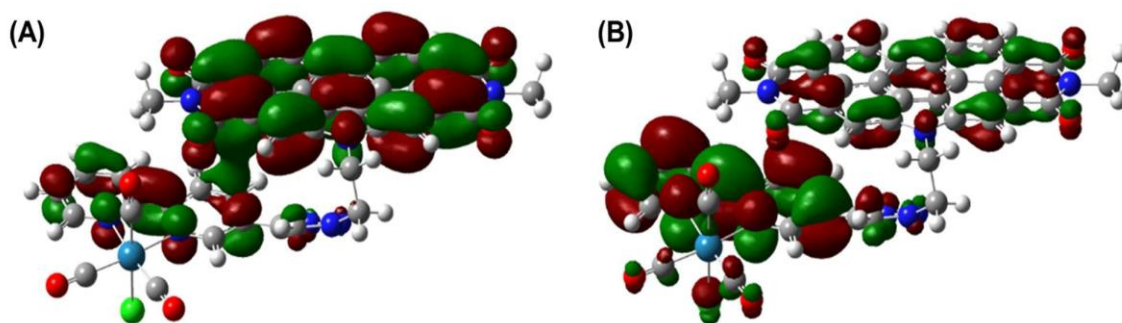


Figure 5.11 Frontier molecular orbitals of the singlet state of $\text{Re}^{\text{I}}(\text{bpy-C2-PDI}^{2-})$ at the M06/6-31G(d,p)/LANL2DZ level of theory, where (A) represents the HOMO and (B) is the LUMO.

Subsequent one-electron reduction of the complex to $\text{Re}^{\text{I}}(\text{bpy}^{\bullet-}\text{-C2-PDI}^{2-})$ resulted in a substantial geometric rearrangement (Figure 5.6B and Figure 5.12). Instead of PDI being folded over the $\text{Re}(\text{bpy-TAz})$ -moiety, the alkyl arm extended to separate the PDI and $\text{Re}(\text{bpy-TAz})$ moieties. Looking at the MOs of the doublet state of $\text{Re}^{\text{I}}(\text{bpy}^{\bullet-}\text{-C2-PDI}^{2-})$, the highest occupied molecular orbital (HOMO) was PDI-localized, while the highest occupied α -spin orbital ($\text{HO}\alpha\text{O}$) was exclusively $\text{Re}(\text{bpy-TAz})$ in character (Figure 5.13). The extended geometry of the $\text{Re}^{\text{I}}(\text{bpy}^{\bullet-}\text{-C2-PDI}^{2-})$ likely resulted from electrostatic repulsion between the negatively charged PDI^{2-} and $\text{Re}(\text{bpy-TAz})^{\bullet-}$ moieties.

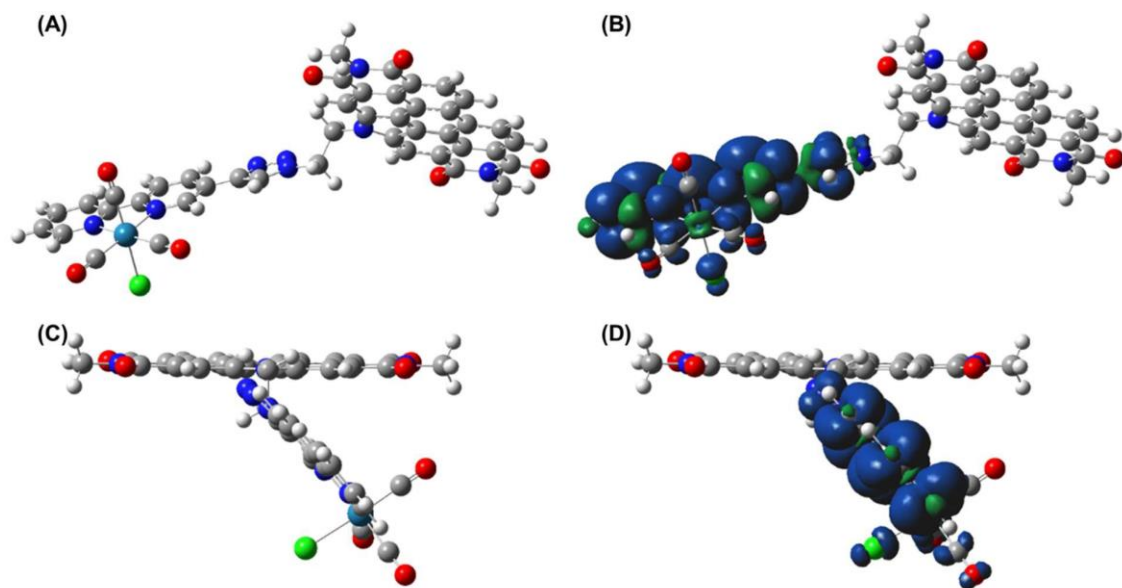


Figure 5.12 Face-on and side-on perspectives of the optimized geometry (A & C) and spin density map (B & D) for the doublet state of $\text{Re}^{\text{I}}(\text{bpy}^{\bullet-}\text{-C2-PDI}^{2-})$ as determined at the M06/6- 31G(d,p)/LANL2DZ level of theory.

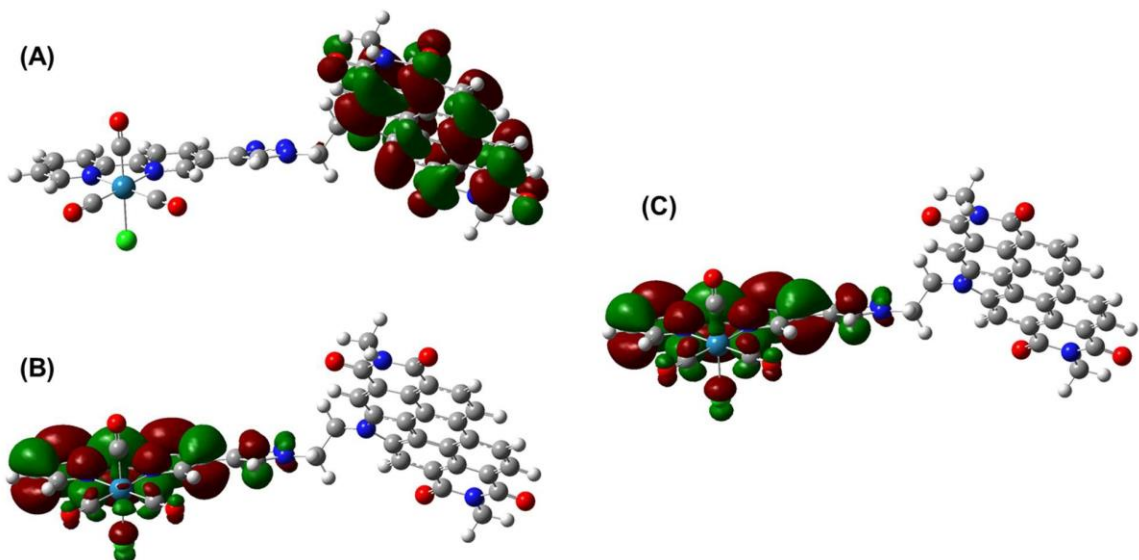


Figure 5.13 Frontier molecular orbitals of the doublet state of $\text{Re}^1(\text{bpy}^{\bullet-}\text{-C2-PDI}^{2-})$ at the M06/6-31G(d,p)/LANL2DZ level of theory, where (A) represents the HOMO with electrons paired on PDI, while (B & C) represent the $\text{HO}\alpha\text{O}$ and $\text{LU}\beta\text{O}$ with α - and β -spins, respectively.

At high overpotentials, $\text{Re}^1(\text{bpy}^{\bullet-}\text{-C2-PDI}^{2-})$ would be reduced once more, causing the displacement of the axial chloride-ligand and generating highly nucleophilic $\text{Re}^0(\text{bpy}^{\bullet-}\text{-C2-PDI}^{2-})$ (Figure 5.6C). Geometry optimization calculations performed on this 5-coordinate $\text{Re}^0(\text{bpy}^{\bullet-}\text{-C2-PDI}^{2-})$ species showed that PDI was still in an extended state relative to the $\text{Re}(\text{bpy-TAz})$ -moiety (Figure 5.14 and Figure 5.15). The MO diagram of this triplet species (Figure 5.16) revealed that the HOMO was exclusively PDI in character and that the overall energy level was unaltered relative to the $\text{Re}^1(\text{bpy}^{\bullet-}\text{-C2-PDI}^{2-})$ precursor (Figure 5.17), while the $\text{HO}\alpha\text{O-1}$ and $\text{HO}\alpha\text{O}$ for $\text{Re}^0(\text{bpy}^{\bullet-}\text{-C2-PDI}^{2-})$ was delocalized over the $\text{Re}(\text{bpy-TAz})$ -moiety only (Figure 5.15). We note that the calculated $\text{HO}\alpha\text{O-1}$ and

HO α O of $\text{Re}^0(\text{bpy}^{\bullet-}\text{-C2-PDI}^{2-})$ were nearly identical to the system reported by Kubiak and co-workers.²³⁶

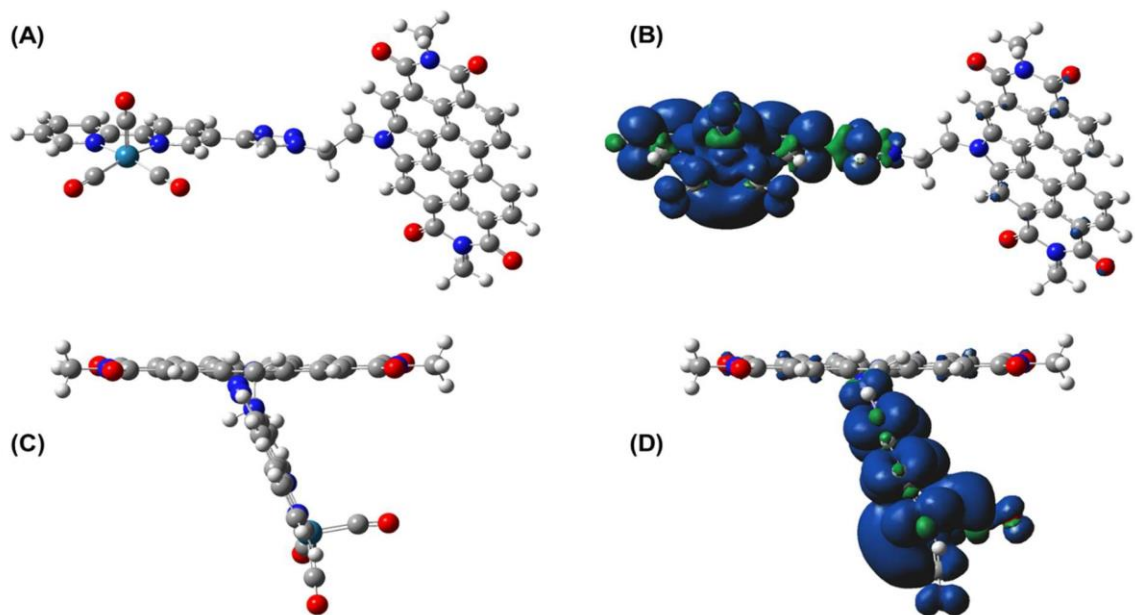


Figure 5.14 Face-on and side-on perspectives of the optimized geometry (A & C) and spin density map (B & D) for the triplet state of $\text{Re}^0(\text{bpy}^{\bullet-}\text{-C2-PDI}^{2-})$ as determined at the M06/6-31G(d,p)/LANL2DZ level of theory.

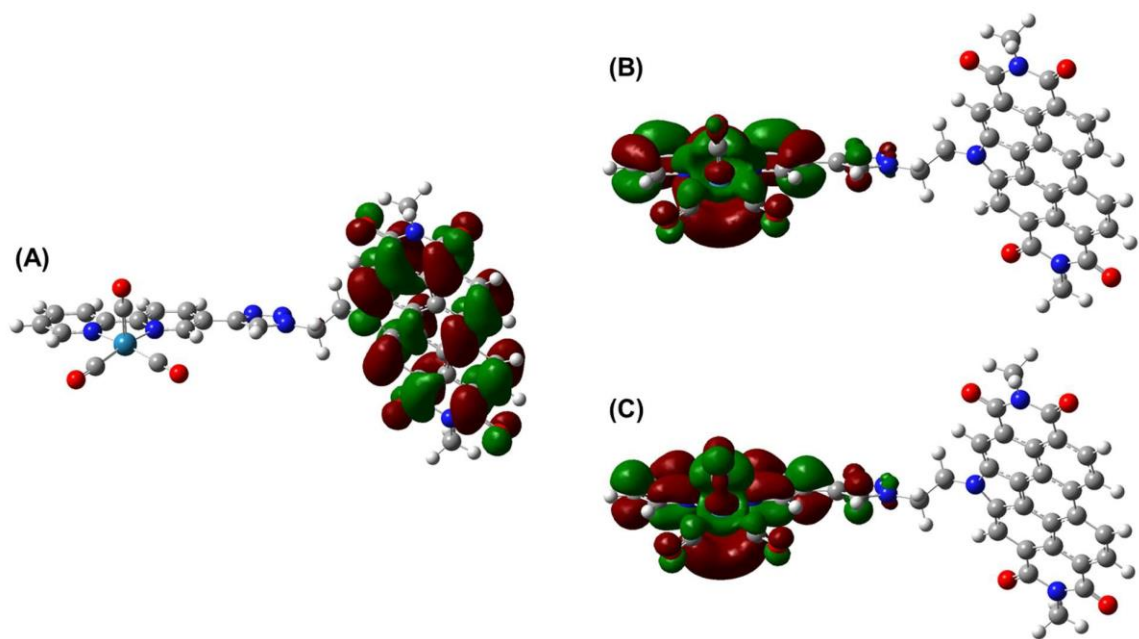


Figure 5.15 Frontier molecular orbitals of the triplet state of $\text{Re}^0(\text{bpy}^{\bullet-}\text{-C2-PDI}^{2-})$ at the M06/6-31G(d,p)/LANL2DZ level of theory, where (A) represents the HOMO with paired electrons on PDI, and (B & C) are the α -spin $\text{HO}\alpha\text{O-1}$ and $\text{HO}\alpha\text{O}$, respectively.

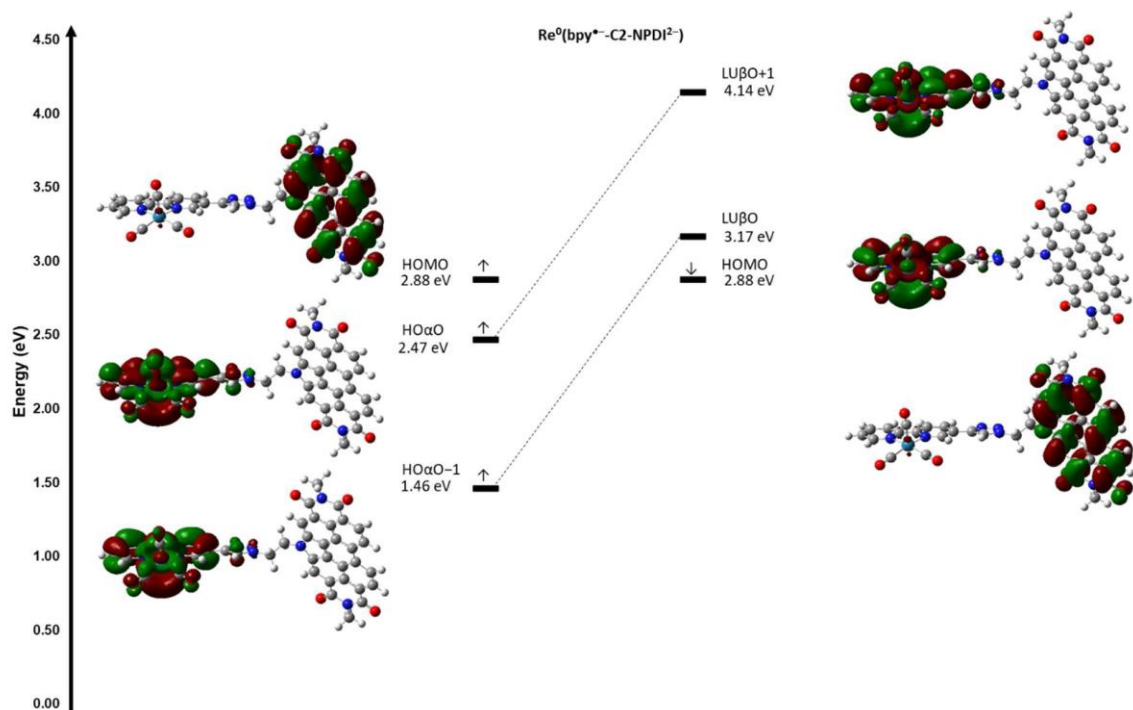


Figure 5.16 Molecular orbital diagram of $\text{Re}^0(\text{bpy}^{\bullet-}\text{-C}_2\text{-PDI}^{2-})$ showing HOMO-1, HOMO, HO α O, LU β O, and LUMO+1 as determined at the M06/6-31G(d,p)/LANL2DZ level of theory.

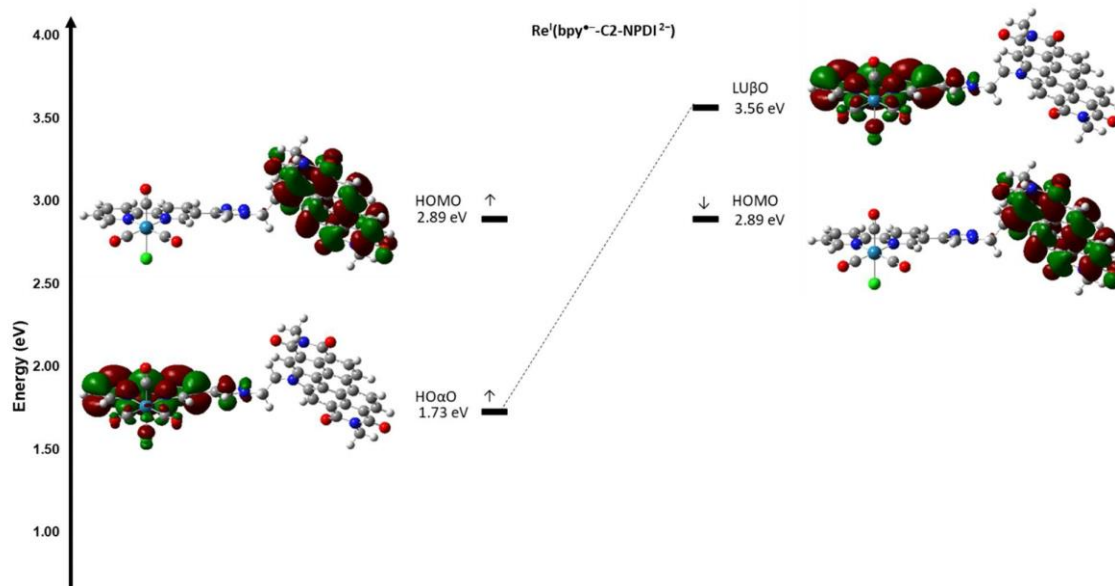


Figure 5.17 Molecular orbital diagram of $\text{Re}^{\text{I}}(\text{bpy}^{\bullet-}\text{-C2-PDI}^{2-})$ showing HOMO, HO α O and LU β O as determined at the M06/6-31G(d,p)/LANL2DZ level of theory.

With FTIR SEC experiments¹¹², it was observed that $\text{Re}^{\text{I}}(\text{bpy}^{\bullet-}\text{-C2-PDI}^{2-})$ could undergo chloro-dissociation to generate a 5-coordinate $\text{Re}^0(\text{bpy}^{\bullet-}\text{-C2-PDI}^{\bullet-})$ species at lower overpotentials (Figure 5.6D). The optimized geometry of $\text{Re}^0(\text{bpy}^{\bullet-}\text{-C2-PDI}^{\bullet-})$ showed that PDI was once again extended away from the $\text{Re}(\text{bpy-TAz})$ -moiety (Figure 5.18). Examining the MOs of doublet state $\text{Re}^0(\text{bpy}^{\bullet-}\text{-C2-PDI}^{\bullet-})$, the HO α O was PDI-centered, while the HOMO was distributed over the $\text{Re}(\text{bpy-TAz})$ -moiety (Figure 5.19). These MOs imply that an electron was transferred from the PDI^{2-} electron-reservoir to the 5-coordinate $\text{Re}(\text{bpy-TAz})$ catalyst center and can be observed in the MO diagram of $\text{Re}^0(\text{bpy}^{\bullet-}\text{-C2-PDI}^{\bullet-})$ (Figure 5.20). Since $\text{Re}(\text{bpy-C2-PDI})$ is not through-conjugated, the electron transfer process likely occurred *via* either a through-bond mechanism similar to $\text{Ru}^{\text{II}}\text{-Re}^{\text{I}}$ systems^{136-137, 237} or a through-space mechanism that was facilitated by the orientation of the chromophore.²³⁸

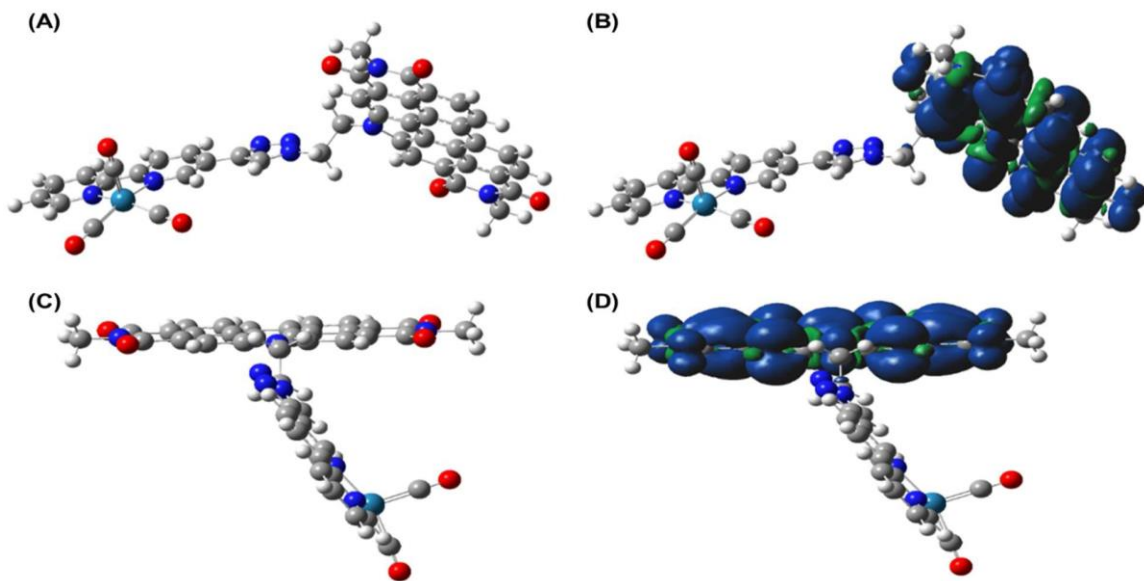


Figure 5.18 Face-on and side-on perspectives of the optimized geometry (A & C) and spin density map (B & D) for the doublet state of $\text{Re}^0(\text{bpy}^{\bullet-}\text{-C2-PDI}^{\bullet-})$ as determined at the M06/6-31G(d,p)/LANL2DZ level of theory.

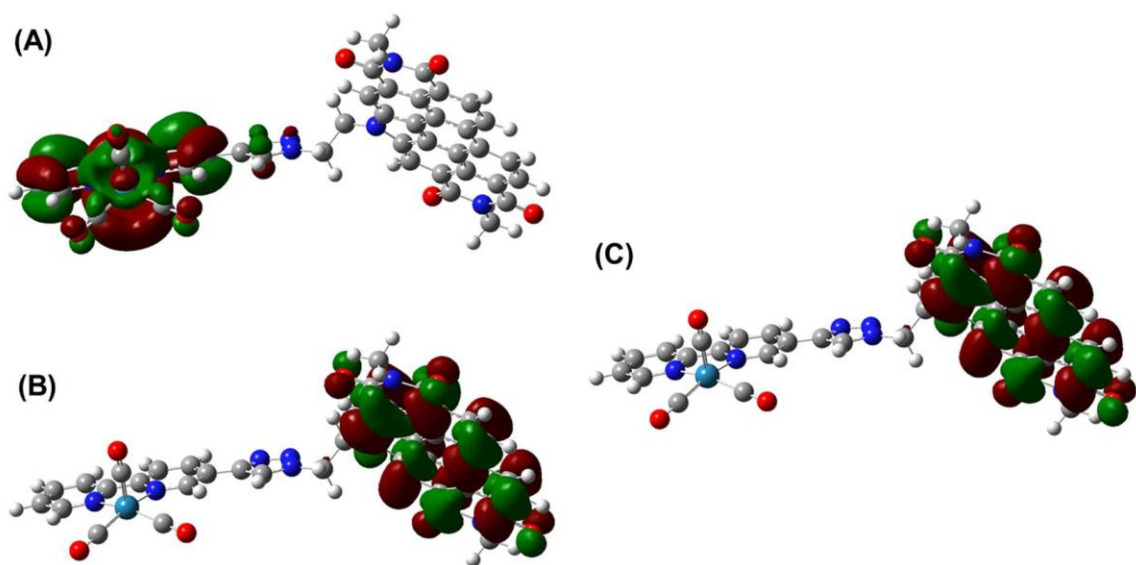


Figure 5.19 Frontier molecular orbitals of the doublet state of $\text{Re}^0(\text{bpy}^{\bullet-}\text{-C2-PDI}^{\bullet-})$ at the M06/6-31G(d,p)/LANL2DZ level of theory, where (A) represents the HOMO with paired electrons on $\text{Re}(\text{bpy})$, and (B & C) are the $\text{HO}\alpha\text{O}$ and $\text{LU}\beta\text{O}$ with α - and β -spins, respectively.

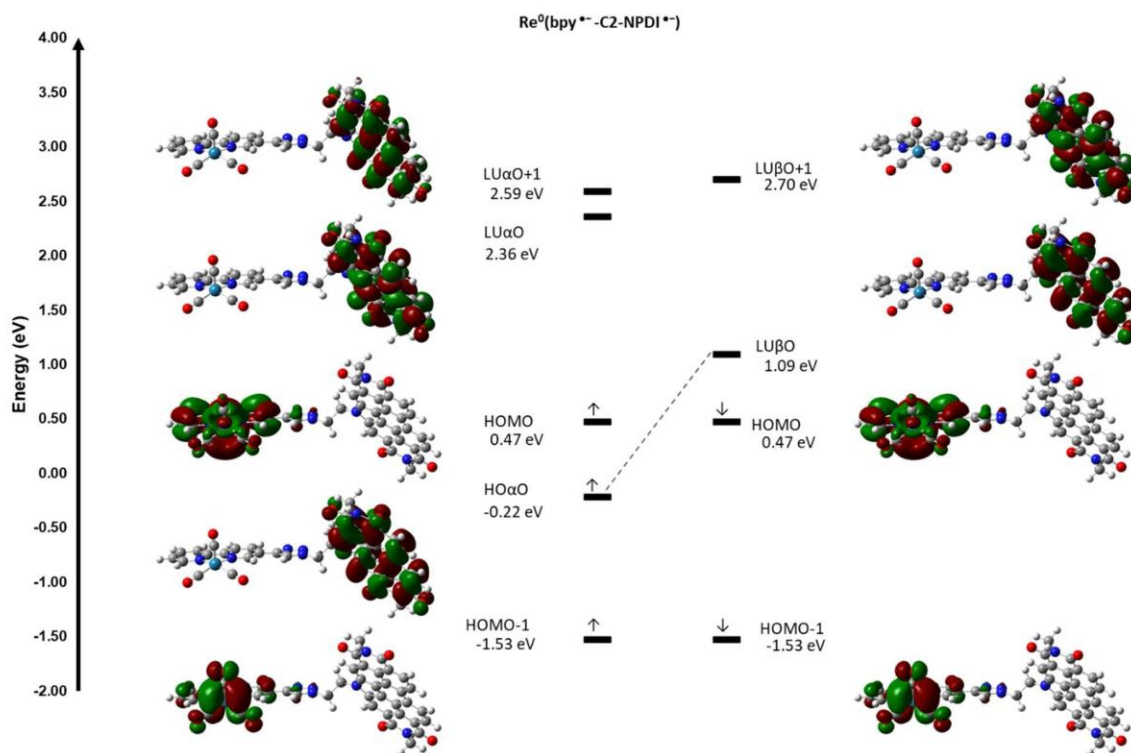


Figure 5.20 Molecular orbital diagram of $\text{Re}^0(\text{bpy}^{\bullet-}-\text{C2-PDI}^{\bullet-})$ showing HOMO-1, HOMO, $\text{HO}\alpha\text{O}$, $\text{LU}\beta\text{O}$, and LUMO+1 as determined at the M06/6-31G(d,p)/LANL2DZ level of theory.

Experimentally there was minimal direct evidence of $\text{Re}(\text{bpy}-\text{C2-PDI})$ adopting either a $\text{Re}^0(\text{bpy}-\text{Taz}^{\bullet-})$ or a Re^{-1} conformation.^{140, 239-241} We note that attempts to reconcile theoretical data on $\text{Re}^0(\text{bpy}^{\bullet-}-\text{C2-PDI}^{\bullet-})$ via calculations with the SMD implicit solvation model,²⁴² explicit inclusion of DMF in the coordination sphere of $\text{Re}(\text{bpy}-\text{Taz})$ (Figure 5.21) or explicit protonation of the PDI^{2-} imide oxygens (Figure 5.22) each resulted in the same MO and spin-density descriptions. While the electronic configuration for the calculated $\text{Re}^0(\text{bpy}^{\bullet-}-\text{C2-PDI}^{\bullet-})$ species was not detected experimentally,¹¹² the possibility of an electron-transfer that results in a $\text{Re}^0(\text{bpy}-\text{Taz}^{\bullet-})$ conformation cannot be

excluded either. It is important to note that a similar electron-transfer process was observed

by Li and co-workers during a DFT analysis of their nanographene-appended rhenium diimine complex.²⁴³ It was elucidated that losing the axial chloride resulted in the hybridization of the Re d_{z^2}/p_z orbitals, whereby the energy level of this hybrid orbital was low enough to facilitate electron-transfer from the ligand. In a direct comparison of the MO diagrams of $\text{Re}^{\text{I}}(\text{bpy}^{\bullet-}\text{-C2-PDI}^{2-})$ and $\text{Re}^0(\text{bpy}^{\bullet-}\text{-C2-PDI}^{\bullet-})$, it was revealed that the displacement of the axial chloride not only altered the symmetry of the Re(bpy-TAz)-based MOs, but also stabilized these MOs such that an electron-transfer from PDI to the Re(bpy-TAz)-moiety could be facilitated under appropriate conditions (Figure 5.23). Based on the HOMO symmetry of $\text{Re}^0(\text{bpy}^{\bullet-}\text{-C2-PDI}^{\bullet-})$ being appropriate for a proton-mediated, two-electron nucleophilic attack on CO_2 , this species is considered a key intermediate in the catalytic cycle.²³⁶

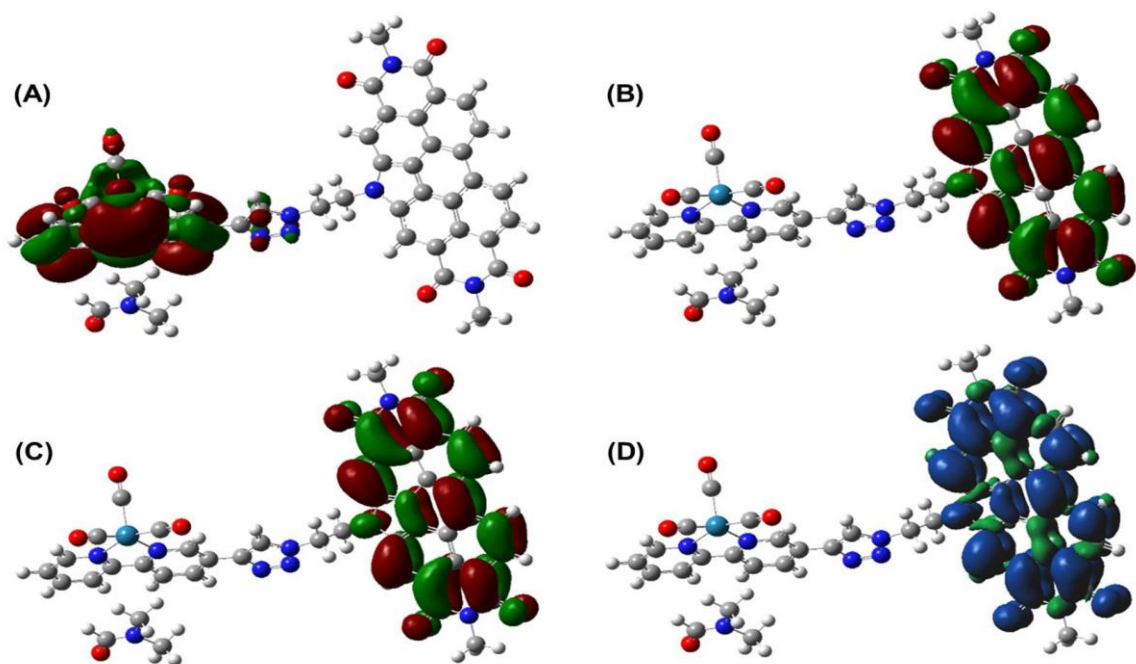


Figure 5.21 Frontier molecular orbitals and spin density mapping at the M06/6-31G(d,p)/LANL2DZ level of theory for the doublet state of $\text{Re}^0(\text{bpy}^{\bullet-}\text{-C2-PDI}^{\bullet-})$ stabilized by an explicit molecule of DMF, where (A) represents the HOMO with paired electrons on $\text{Re}(\text{bpy})$, and (B & C) are the $\text{HO}\alpha\text{O}$ and $\text{LU}\beta\text{O}$ with α - and β -spins, respectively, and (D) is the spin density map.

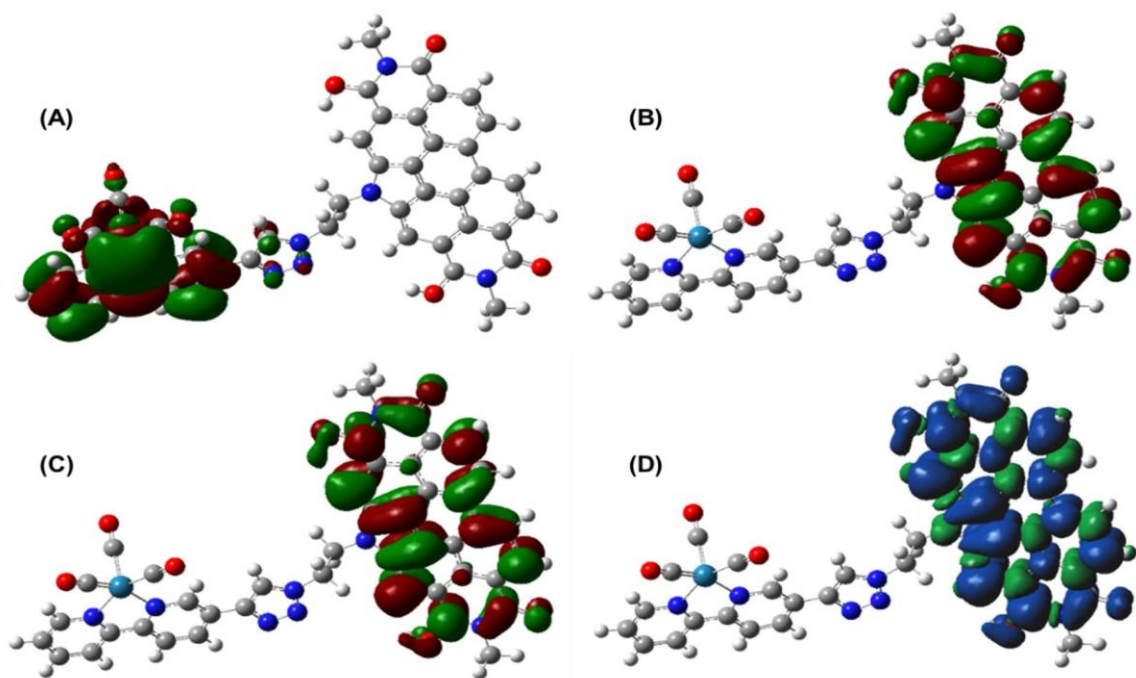


Figure 5.22 Frontier molecular orbitals and spin density mapping at the M06/6-31G(d,p)/LANL2DZ level of theory for the doublet state of $\text{Re}^0(\text{bpy}^{\bullet-}\text{-C2-PDI}^{\bullet-})$ stabilized by explicit protonation of PDI imide oxygens, where (A) represents the HOMO with paired electrons on $\text{Re}(\text{bpy})$, and (B & C) are the $\text{HO}\alpha\text{O}$ and $\text{LU}\beta\text{O}$ with α - and β -spins, respectively, and (D) is the spin density map.

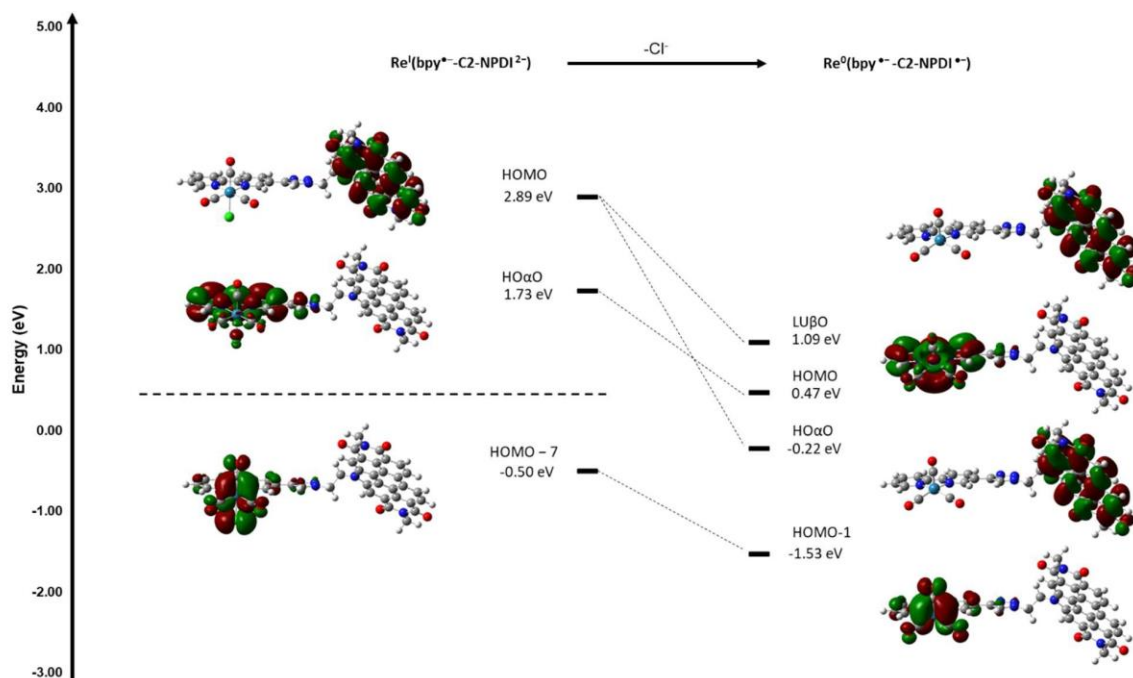


Figure 5.23 Molecular orbital diagram showing the transition from $\text{Re}^{\text{I}}(\text{bpy}^{\bullet-}\text{-C2-PDI}^{2-})$ to $\text{Re}^{\text{0}}(\text{bpy}^{\bullet-}\text{-C2-PDI}^{\bullet-})$ as determined at the M06/6-31G(d,p)/LANL2DZ level of theory. Loss of axial chloride leads to significant stabilization of relative energy levels.

Since CO was the major product of CPE experiments,¹¹² $\text{HOOC-Re}^{\text{I}}(\text{bpy-C2-PDI}^{\bullet-})$ was most likely formed following CO_2 activation by $\text{Re}^{\text{0}}(\text{bpy}^{\bullet-}\text{-C2-PDI}^{\bullet-})$ (Figure 5.6E). The optimized geometry of this intermediate still demonstrated an extended bpy-C2-PDI ligand and the spin-density for the doublet state was largely located on PDI (Figure 5.24). A proton-coupled electron-transfer was invoked in this first catalytic step because the unprotonated $^-\text{OOC-Re}^{\text{I}}(\text{bpy-C2-PDI}^{\bullet-})$ species was found to be much higher in energy. Moreover, the calculated Re-CO_2^- bond length (3.91 Å) can be described as nonbonding as it exceeds the sum of the van der Waals radii (Figure 5.25 to Figure 5.27). Subsequent reduction of the protonated intermediate would yield $\text{HOOC-Re}^{\text{I}}(\text{bpy}^{\bullet-}\text{-C2-PDI}^{\bullet-})$ (Figure 5.6F and Figure 5.28). Coincidentally, this same species would also result

from the proton-coupled activation of CO_2 by $\text{Re}^0(\text{bpy}^{\bullet-}\text{-C2-PDI}^{2-})$ at higher overpotentials. While both the singlet and triplet states of $\text{HOOC-Re}^{\text{I}}(\text{bpy}^{\bullet-}\text{-C2-PDI}^{\bullet-})$ were considered, the triplet state was ~ 0.4 eV more stable. The triplet state of $\text{HOOC-Re}^{\text{I}}(\text{bpy}^{\bullet-}\text{-C2-PDI}^{\bullet-})$ displayed an extended conformation, with significant delocalization across both the $\text{HO}\alpha\text{O-1}$ and the $\text{HO}\alpha\text{O}$ orbitals (Figure 5.29). Moreover, appreciable back-bonding interactions were observed between Re and COOH, which could facilitate the proton-assisted displacement of H_2O , en route to forming $\text{OC-Re}^{\text{I}}(\text{bpy}^{\bullet-}\text{-C2-PDI}^{\bullet-})$.²⁴⁰

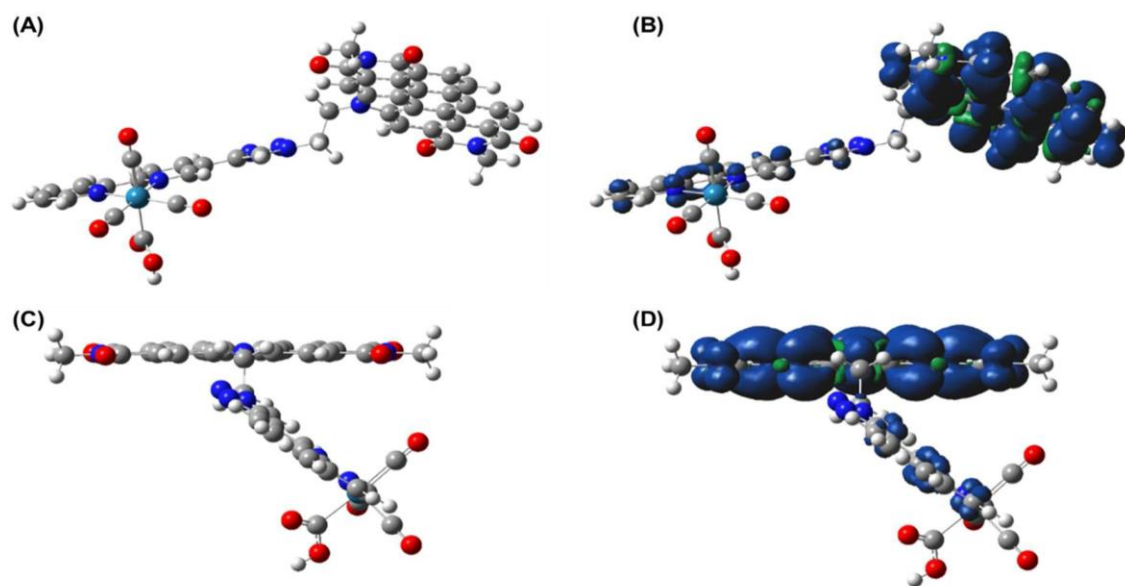


Figure 5.24 Face-on and side-on perspectives of the optimized geometry (A & C) and spin density map (B & D) for the doublet state of $\text{HOOC-Re}^{\text{I}}(\text{bpy-C2-PDI}^{\bullet-})$ as determined at the M06/6-31G(d,p)/LANL2DZ level of theory.

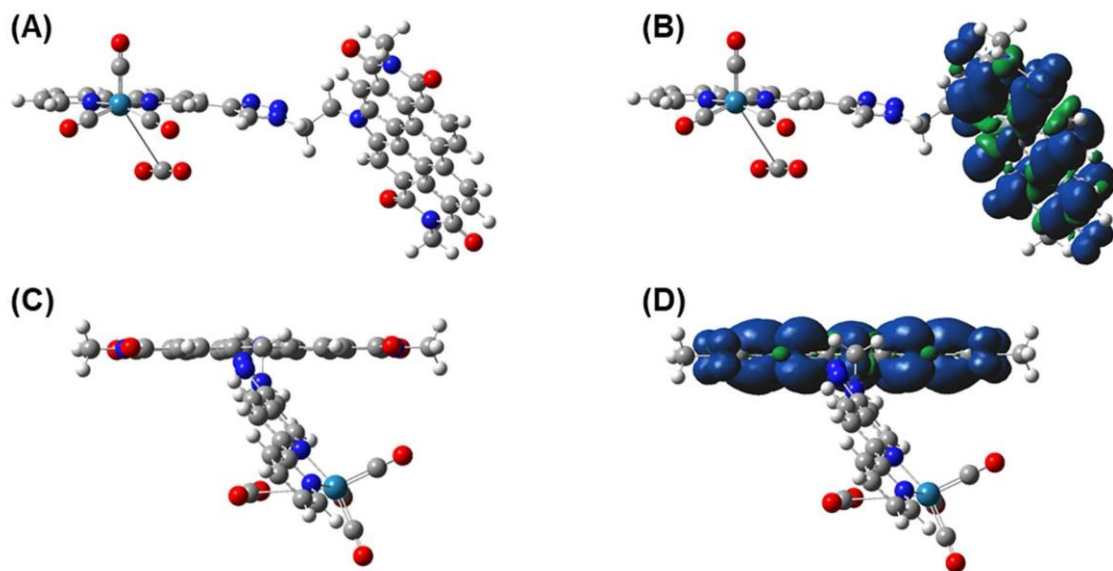


Figure 5.25 Face-on and side-on perspectives of the optimized geometry (A & C) and spin density map (B & D) for the triplet state of $^-OOC-Re^I(bpy-C2-PDI^{\bullet-})$ as determined at the M06/6-31G(d,p)/LANL2DZ level of theory.

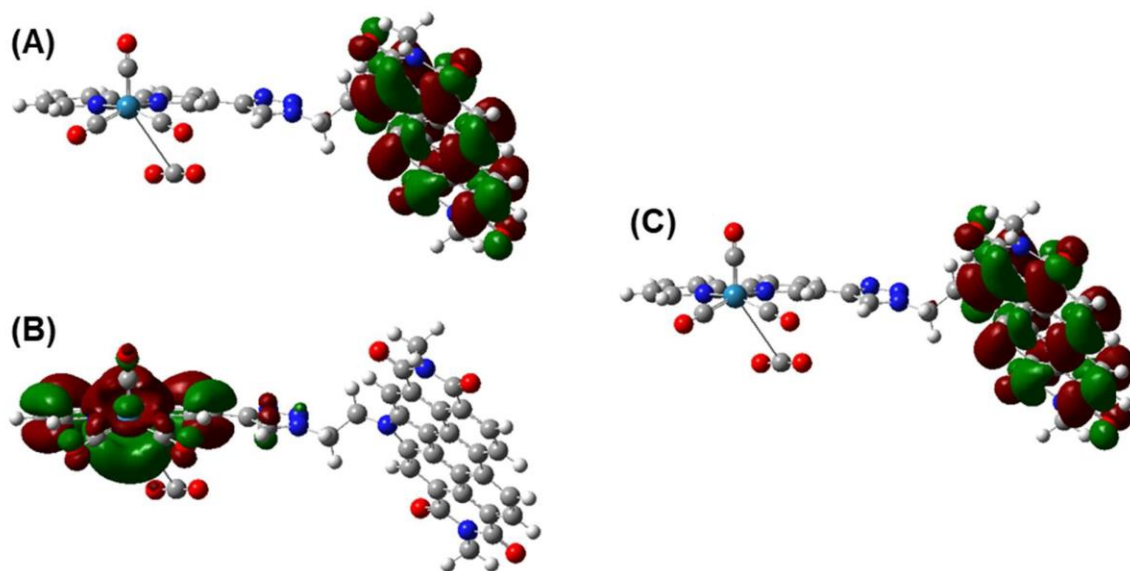


Figure 5.26 Frontier molecular orbitals of the triplet state of ${}^{-}\text{OOC-ReI}(\text{bpy-C2-PDI}^{\bullet-})$ at the M06/6-31G(d,p)/LANL2DZ level of theory, where (A) represents the HOMO, and (B & C) are the $\text{HO}\alpha\text{O}$ and $\text{LU}\beta\text{O}$ with α - and β -spins, respectively.

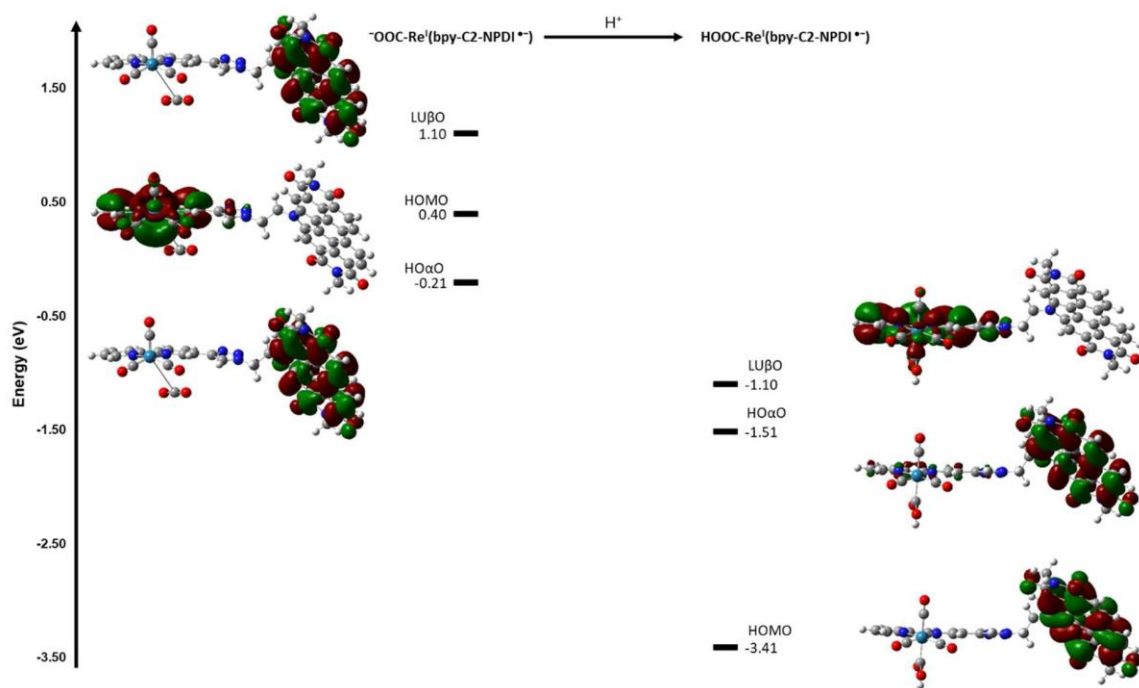


Figure 5.27 Molecular orbital diagram showing the transition from $^-OOC-Re^I(bpy-C2-PDI^{\bullet-})$ to $HOOC-Re^I(bpy-C2-PDI^{\bullet-})$ as determined at the M06/6-31G(d,p)/LANL2DZ level of theory. Addition of proton leads to significant stabilization of relative energy levels.

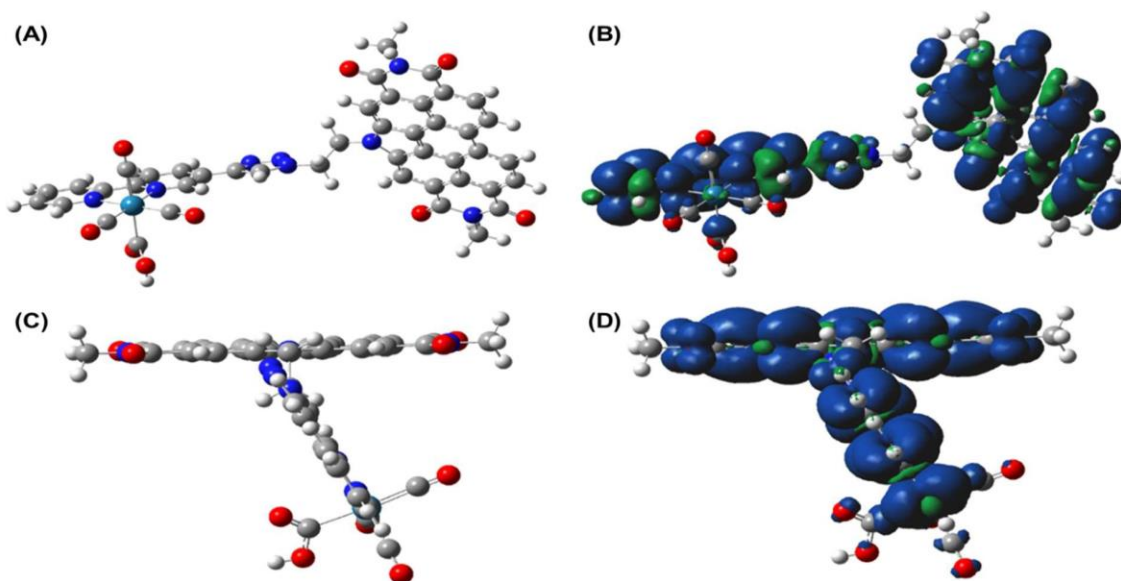


Figure 5.28 Face-on and side-on perspectives of the optimized geometry (A & C) and spin density map (B & D) for the triplet state of $\text{HOOC-Re}^{\text{I}}(\text{bpy}^{\bullet-}\text{-C2-PDI}^{\bullet-})$ as determined at the M06/6-31G(d,p)/LANL2DZ level of theory.

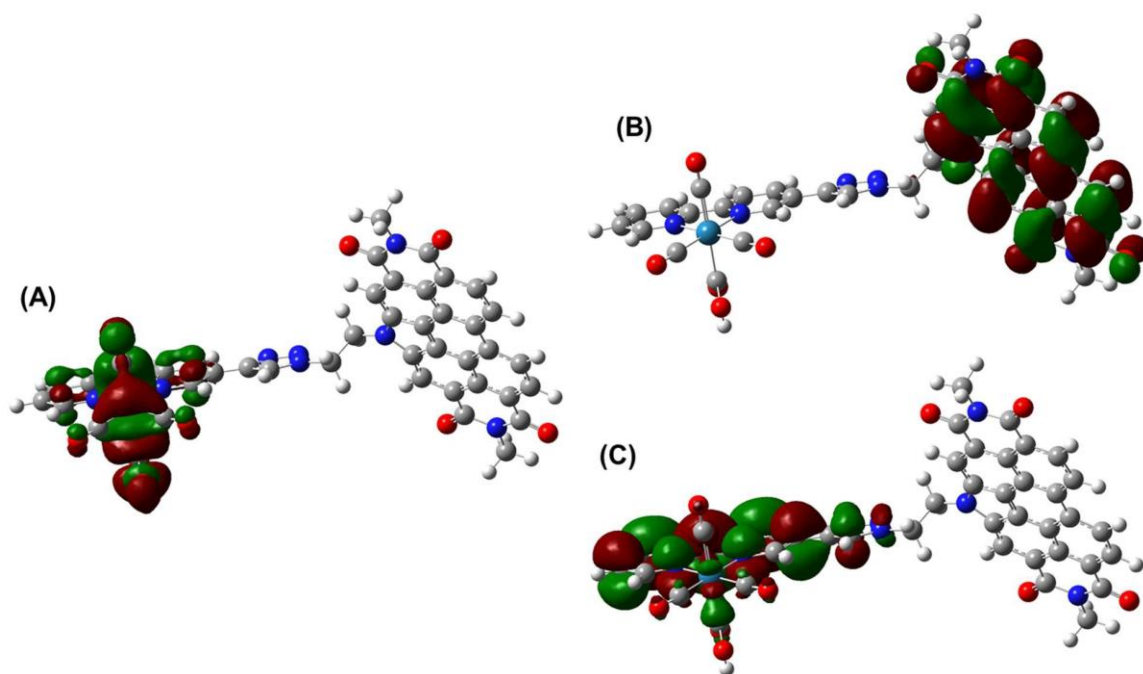


Figure 5.29 Frontier molecular orbitals of the triplet state of $\text{HOOC-Re}^{\text{I}}(\text{bpy}^{\bullet-}\text{-C2-PDI}^{\bullet-})$ at the M06/6-31G(d,p)/LANL2DZ level of theory, where (A) represents the HOMO, and (B & C) are the $\text{HO}\alpha\text{O-1}$ and $\text{HO}\alpha\text{O}$ with α -electrons, respectively.

The optimized geometry of $\text{OC-Re}^{\text{I}}(\text{bpy}^{\bullet-}\text{-C2-PDI}^{\bullet-})$ showed that PDI folds back over the $\text{Re}(\text{bpy-TAz})$ -moiety (Figure 5.6G and Figure 5.30). Here, the triplet state was more energetically favorable (by ~ 0.5 eV) than the corresponding spin-paired singlet state. The spin-density map of the triplet state, containing both $\text{HO}\alpha\text{O-1}$ and $\text{HO}\alpha\text{O}$ character (Figure 5.31), indicated extensive electron delocalization. Moreover, there were still back-bonding interactions between Re-CO in the $\text{HO}\alpha\text{O}$, which would assist with the displacement of CO. Adding another electron to the system, generating transition-state $\text{OC}\cdots\text{Re}^0(\text{bpy}^{\bullet-}\text{-C2-PDI}^{\bullet-})$, dramatically impacted the molecular geometry (Figure 5.6 and Figure 5.32). Not only was twisting observed in the bpy-TAz ligand, but there was also a distinct lengthening in one of the axial Re-CO bonds that became essentially non-bonding

(at 3.22 Å). The spin density of this *pseudo*-5-coordinate species was entirely on PDI, signifying the electron was added to the lowest unoccupied β -spin orbital (Lu β O) of the preceding species. Furthermore, the spin density of OC \cdots Re⁰(bpy^{•-}-C2-PDI^{•-}) was reminiscent of 5-coordinate Re⁰(bpy^{•-}-C2-PDI^{•-}), indicating the regeneration of this active species for the low overpotential catalytic cycle. At high overpotentials, Re⁰(bpy^{•-}-C2-PDI^{•-}) would likely undergo a one-electron reduction to regenerate the Re⁰(bpy^{•-}-C2-PDI²⁻) species.

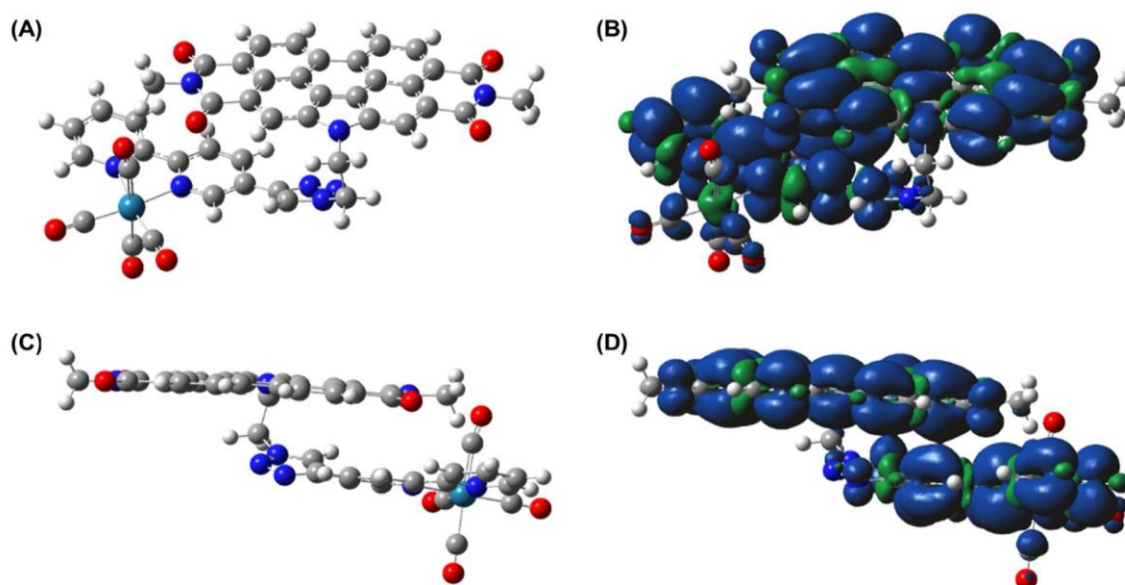


Figure 5.30 Face-on and side-on perspectives of the optimized geometry (A & C) and spin density map (B & D) for the triplet state of OC-Re^I(bpy^{•-}-C2-PDI^{•-}) as determined at the M06/6-31G(d,p)/LANL2DZ level of theory.

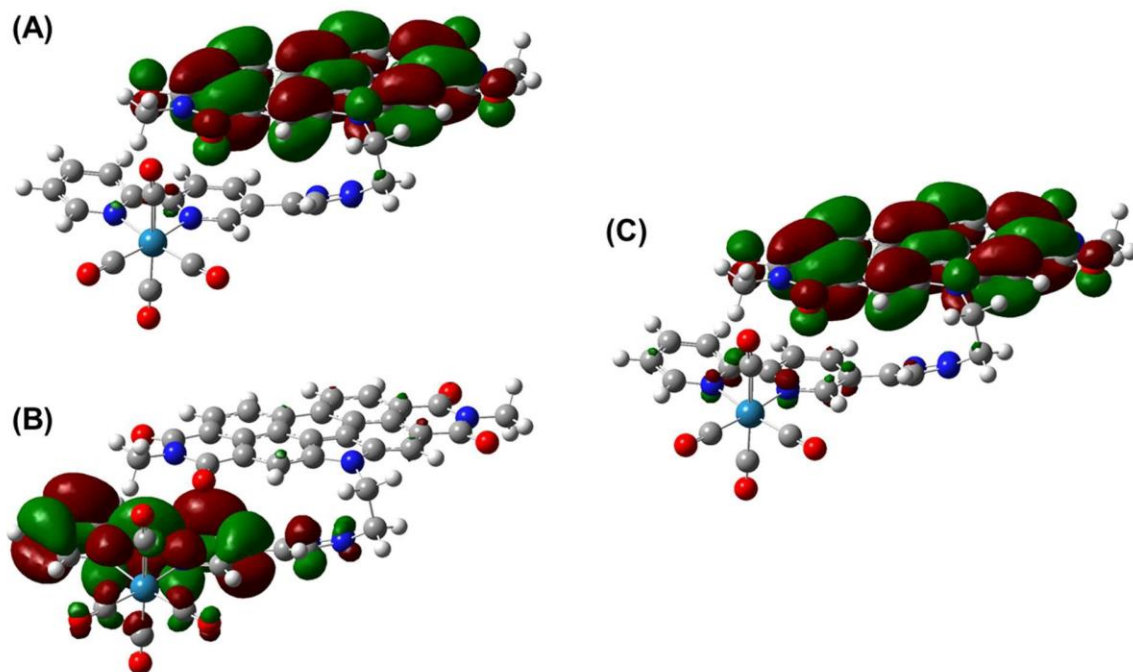


Figure 5.31 Frontier molecular orbitals of the triplet state of $\text{OC-Re}^{\text{I}}(\text{bpy}^{\bullet-}\text{-C2-PDI}^{\bullet-})$ at the M06/6-31G(d,p)/LANL2DZ level of theory, where (A & B) represent the $\text{HO}\alpha\text{O-1}$ and $\text{HO}\alpha\text{O}$ with α -electrons, and (C) is the $\text{LU}\beta\text{O}$ with β -spin.

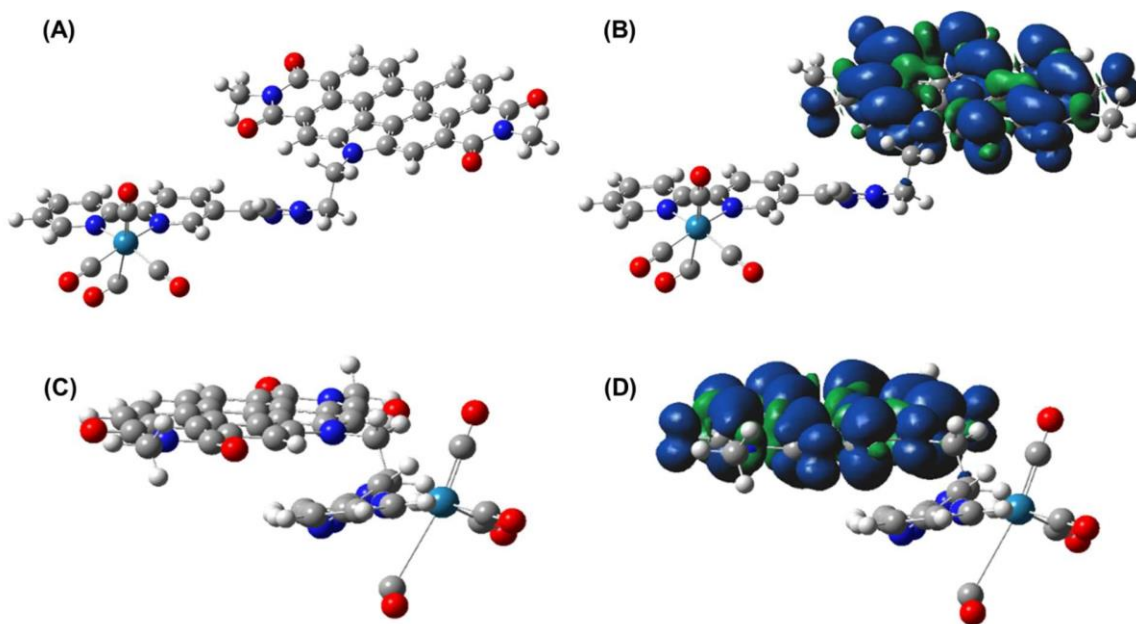


Figure 5.32 Face-on and side-on perspectives of the optimized geometry (A & C) and spin density map (B & D) for the doublet state of $\text{OC}\cdots\text{Re}0(\text{bpy}^{\bullet-}\text{-C2-PDI}^{\bullet-})$ as determined at the M06/6-31G(d,p)/LANL2DZ level of theory.

5.4 Conclusions

Lowering the overpotential of the electrochemical reduction of CO_2 is vital to improve the efficiency of the organometallic catalyst. From the electronic properties, we observe the narrowing of the HOMO-LUMO gap of the deprotonated PDI^- and destabilization of the HOMO and LUMO when compared to PDI and this allows the energetic match with the FMOs of the $\text{Re}(\text{bpy})$ catalyst and as such, facilitates the tethering of PDI to the catalyst. Tethering the PDI chromophore to the catalyst is initially perceived to lower the overpotential due to unique properties of the PDI molecule.

With a dissection of all the data from our comprehensive studies, information relevant to the electrocatalytic CO₂ reduction mechanism may be summarized as follows. Using first principles DFT calculations, we showed that geometric orientation between PDI and Re(bpy)-moiety is important to the electron-transfer dynamics during CO₂ reduction where an extended conformation was favorable. We also showed the PDI works cooperatively with the Re(bpy)-moiety to manage electrons for the reduction of CO₂. The 5-coordinated complex of Re⁰(bpy^{•-}-C2-PDI²⁻) was identified as the active complex in the catalytic cycle that facilitated the proton-coupled electron-mediated reduction of CO₂. It was further elucidated that the PDI can act as an electron reservoir for the Re(bpy)-moiety at low overpotentials as indicated by the MO diagram of the 5-coordinated complex. This electron reservoir effect allowed for enhanced CO₂ reduction activity at low overpotentials observed in experiments.¹¹² These results could help guide future molecular design by thoughtfully tailoring of both the chromophore (electron reservoir) and the metal–ligand complex.

This work clearly demonstrates the utility of organic chromophore electron reservoirs to effectively lower the overpotential required for CO₂ reduction for Re(bpy) complexes. Operation of these molecular electrocatalysts at lower overpotentials not only decreases the required energetic input but also may improve system longevity.^{114, 133} Moreover, these chromophores may serve as useful electrode anchoring units (i.e., through π -stacking), a strategy that is well-known to simultaneously increase catalyst activity and longevity.^{58, 244-249} A combination of these concepts of diminished overpotential and improved catalyst stability together may afford the prospect of developing industrially

feasible devices.^{129, 250-253} Given the abundance of photoactive π -conjugated chromophores, an opportunity exists to systematically synthesize a variety of CO₂ reduction catalysts that have tailored properties to maximize performance.

CHAPTER 6. SYNOPSIS

6.1 Conclusions and future perspective

The current global energy outlook is complex and multifaceted, with a range of factors influencing the production, consumption, and distribution of energy around the world. Despite efforts to improve energy efficiency and conservation, the energy demand is expected to continue to grow in the coming decades, driven by population growth, urbanization, and rising living standards in developing countries. The mix of energy sources is also changing, with renewable energy sources like solar and wind power playing an increasingly important role, fossil fuels remain a significant part of the energy mix in many countries. It is quite evident from Chapter 1 of this dissertation that a multi-pronged approach is needed to achieve net-zero carbon emission and mitigate climate change.

Biofuels offer a way to diversify the renewable energy sector, reducing reliance on solar and wind power, which can be intermittent and weather dependent. Biofuels also help reduce waste by utilizing organic matter that would otherwise be disposed of in landfills or left to decompose, which can lead to the release of methane, a potent greenhouse gas. However, there are challenges to biofuels production and one such challenge of developing well performing catalysts for deoxygenation of feedstock materials is explored in Chapter 3 of this work. Understanding the reaction mechanism of deoxygenation reactions on catalytic surfaces can greatly improve our ability to design better catalysts.

To move a step closer to achieving this objective, we employed DFT calculations to establish that PAc predominantly adopts a bidentate binding mode on Ni[111].

Microkinetic modeling making use of DFT-determined parameters shows that PAc

dehydroxylation followed by two α -carbon dehydrogenation steps of $\text{CH}_3\text{CH}_2\text{CO}^*$ intermediate to CH_3CCO^* , then the $-\text{CO}$ abstraction and ultimately hydrogenation to ethane as the dominant pathway at 573 K. The lateral interaction effect with first order approximated H^* coverage on the reaction mechanism showed an increase in the activation barriers of key elementary steps. The model also provides valuable insights on the reaction orders of the gas phase species. The pathway proposed in this contribution has a TOF of $2.75 \times 10^{-11} \text{s}^{-1}$, which is slower than the reported experimental value although, the E_{app} of 1.15 eV (0.92 eV if the value is estimated using Campbell's degree of rate control) is in reasonable agreement with experiment. We showed that the adsorption geometry of the organic molecule on the surface of the catalyst plays an important role in reaction mechanism.

Perovskites are a promising candidate for solar cells because they have comparable efficiencies to silicon-based solar cells with lower manufacturing cost, versatile absorption range of the solar spectrum and tunable properties. However, as stated in Chapter 1, they are challenged by surface instability and higher defects to name a few. To improve its stability and tune its optical properties, in Chapter 4, we studied the effect of SAMs of An^+ based ligands on the surface of FASnI_3 perovskite. We employed DFT calculations to explore some of the proposed ligands that are known to passivate the perovskite structure. We explored the bulk properties of cubic FASnI_3 perovskite and surface electronic properties of [110] FA-I terminated perovskite slab. The geometric structure calculations showed that substitution of surface FA^+ cations with An^+ and its fluorinated derivatives greatly reduced the surface energy of formation, indicating a more stable surface structure.

An^+ and its fluorinated derivatives bind stronger than FA^+ cations to the perovskite surface except for 2,3,4,5,6- FA^+ cation, likely due to the extent of ligand penetration. Surface modification of the FASnI_3 perovskite with An^+ and its fluorinated derivatives showed a correlation between the net molecular dipole moment and the work function. A correlation was also observed between the net dipole moment and the vacuum potential and the Fermi energy. The charge density difference plots showed that An^+ and its derivatives did not change the electronic structure significantly but showed stronger binding of the ligands on the surface when compared to the FA^+ ions. Understanding this behavior can lead to effective design of the perovskite surface to tune the work function and control the surface electronic properties.

In Chapter 5, we explore the possibility of improving catalysts for CO_2 conversion that can essentially close the carbon-loop and mitigate climate change. CO_2 conversion involves transforming CO_2 into other useful products, such as fuels, chemicals, or building materials, through chemical or biological processes. By converting CO_2 into valuable products, we can reduce the amount of CO_2 released into the atmosphere, thereby reducing the concentration of greenhouse gases and mitigating the effects of climate change.

Lowering the overpotential of the electrochemical reduction of CO_2 is vital to improve the efficiency of the organometallic catalyst. To achieve this objective, we used DFT calculations to study the electronic properties of the catalyst and the chromophore. From the electronic properties, we demonstrated that the PDI chromophore possess properties that make it viable for tethering to the $\text{Re}(\text{bpy})$ catalyst. Tethering the PDI chromophore to the catalyst is shown to lower the overpotential due to unique properties

of the PDI molecule. The geometric orientation between PDI and Re(bpy)-moiety is important to the electron-transfer dynamics during CO₂ reduction where an extended conformation was favorable. We also showed the PDI works cooperatively with the Re(bpy)-moiety to manage electrons for the reduction of CO₂. The active complex identified in the study facilitated the proton-coupled electron-mediated reduction of CO₂. It was further elucidated that the PDI can act as an electron reservoir for the Re(bpy)-moiety at low overpotentials as indicated by the MO diagram of the active complex. This electron reservoir effect allowed for enhanced CO₂ reduction activity at low overpotentials observed in experiments.¹¹² These results could help guide future molecular design by thoughtfully tailoring of both the chromophore (electron reservoir) and the metal–ligand complex. This work clearly demonstrates the utility of organic chromophore electron reservoirs to effectively lower the overpotential required for CO₂ reduction for Re(bpy) complexes. Given the abundance of photoactive π -conjugated chromophores, an opportunity exists to systematically synthesize a variety of CO₂ reduction catalysts that have tailored properties to maximize performance.

This dissertation reports on the computational methods and the analyses that provide atomic-scale understanding of key properties of materials for green energy generation. A requisite to design principles of materials through understanding of geometric effects of surfaces and molecules is presented. The overarching hypothesis of this dissertation, *critical understanding of surface and molecular geometry of functionalized materials from first principles can be used to tune the performance parameters for green energy generation*, is achieved through first principles simulations.

To further this initiative, artificial intelligence (AI) and machine learning (ML) methods are proving to be an accelerated approach to predicting properties of materials. Given the complexity of first principles calculations and the extensive resources that they command, AI/ML methods have the potential to drive materials discovery for green energy generation into new frontiers. The balance between acceleration and accuracy of the prediction is critical to these types of methods. In addition, data generation, collection and curation are also challenging, and emergence of many databases are beginning to address them. First principles calculations, in general, can generate enormous amount of data that is often not shared publicly. Mining data from output files of these calculations can greatly facilitate the ease of building AI/ML models with better accuracy, lower bias and avoid the problem of overfitting. The full potential of AI/ML methods remains to be explored but is showing promising signs in the field of materials discovery for green energy generation.

References

1. Gray, N.; McDonagh, S.; O'Shea, R.; Smyth, B.; Murphy, J. D., Decarbonising ships, planes and trucks: An analysis of suitable low-carbon fuels for the maritime, aviation and haulage sectors. *Advances in Applied Energy* **2021**, *1*, 100008.
2. Correa, D. F.; Beyer, H. L.; Fargione, J. E.; Hill, J. D.; Possingham, H. P.; Thomas-Hall, S. R.; Schenk, P. M., Towards the implementation of sustainable biofuel production systems. *Renewable and Sustainable Energy Reviews* **2019**, *107*, 250-263.
3. Tanzer, S. E.; Ramírez, A., When are negative emissions negative emissions? *Energy & Environmental Science* **2019**, *12* (4), 1210-1218.
4. Von Cossel, M.; Wagner, M.; Lask, J.; Magenau, E.; Bauerle, A.; Von Cossel, V.; Warrach-Sagi, K.; Elbersen, B.; Staritsky, I.; Van Eupen, M.; Iqbal, Y.; Jablonowski, N. D.; Happe, S.; Fernando, A. L.; Scordia, D.; Cosentino, S. L.; Wulfmeyer, V.; Lewandowski, I.; Winkler, B., Prospects of Bioenergy Cropping Systems for A More Social-Ecologically Sound Bioeconomy. *Agronomy* **2019**, *9* (10), 605.
5. Ogunkoya, D.; Roberts, W. L.; Fang, T.; Thapaliya, N., Investigation of the effects of renewable diesel fuels on engine performance, combustion, and emissions. *Fuel* **2015**, *140*, 541-554.
6. Donnis, B.; Egeberg, R. G.; Blom, P.; Knudsen, K. G., Hydroprocessing of Bio-Oils and Oxygenates to Hydrocarbons. Understanding the Reaction Routes. *Topics in Catalysis* **2009**, *52* (3), 229-240.
7. Kubičková, I.; Snåre, M.; Eränen, K.; Mäki-Arvela, P.; Murzin, D. Y., Hydrocarbons for diesel fuel via decarboxylation of vegetable oils. *Catalysis Today* **2005**, *106* (1), 197-200.
8. Centi, G.; van Santen, R. A., *Catalysis for Renewables: From Feedstock to Energy Production*. Wiley: 2008; pp 1-448.
9. Zhang, J.; Huo, X.; Li, Y.; Strathmann, T. J., Catalytic Hydrothermal Decarboxylation and Cracking of Fatty Acids and Lipids over Ru/C. *ACS Sustainable Chemistry & Engineering* **2019**, *7* (17), 14400-14410.
10. Do, P. T.; Chiappero, M.; Lobban, L. L.; Resasco, D. E., Catalytic Deoxygenation of Methyl-Octanoate and Methyl-Stearate on Pt/Al₂O₃. *Catalysis Letters* **2009**, *130* (1), 9-18.
11. Chiappero, M.; Do, P. T. M.; Crossley, S.; Lobban, L. L.; Resasco, D. E., Direct conversion of triglycerides to olefins and paraffins over noble metal supported catalysts. *Fuel* **2011**, *90* (3), 1155-1165.
12. Na, J.-G.; Yi, B. E.; Han, J. K.; Oh, Y.-K.; Park, J.-H.; Jung, T. S.; Han, S. S.; Yoon, H. C.; Kim, J.-N.; Lee, H.; Ko, C. H., Deoxygenation of microalgal oil into hydrocarbon with precious metal catalysts: Optimization of reaction conditions and supports. *Energy* **2012**, *47* (1), 25-30.
13. Mäki-Arvela, P.; Kubickova, I.; Snåre, M.; Eränen, K.; Murzin, D. Y., Catalytic Deoxygenation of Fatty Acids and Their Derivatives. *Energy & Fuels* **2007**, *21* (1), 30-41.

14. Snåre, M.; Kubičková, I.; Mäki-Arvela, P.; Eränen, K.; Wärnå, J.; Murzin, D. Y., Production of diesel fuel from renewable feeds: Kinetics of ethyl stearate decarboxylation. *Chemical Engineering Journal* **2007**, *134* (1), 29-34.
15. Lu, J.; Behtash, S.; Heyden, A., Theoretical Investigation of the Reaction Mechanism of the Decarboxylation and Decarbonylation of Propanoic Acid on Pd(111) Model Surfaces. *The Journal of Physical Chemistry C* **2012**, *116* (27), 14328-14341.
16. Yang, W.; Solomon, R. V.; Lu, J.; Mamun, O.; Bond, J. Q.; Heyden, A., Unraveling the mechanism of the hydrodeoxygenation of propionic acid over a Pt (1 1 1) surface in vapor and liquid phases. *Journal of Catalysis* **2020**, *381*, 547-560.
17. Otyuskaya, D.; Thybaut, J. W.; Alexiadis, V.; Alekseeva, M.; Venderbosch, R.; Yakovlev, V.; Marin, G. B., Fast pyrolysis oil stabilization kinetics over a Ni-Cu catalyst using propionic acid as a model compound. *Applied Catalysis B: Environmental* **2018**, *233*, 46-57.
18. Zare, M.; Solomon, R. V.; Yang, W.; Yonge, A.; Heyden, A., Theoretical Investigation of Solvent Effects on the Hydrodeoxygenation of Propionic Acid over a Ni(111) Catalyst Model. *The Journal of Physical Chemistry C* **2020**, *124* (30), 16488-16500.
19. Lu, J.; Behtash, S.; Faheem, M.; Heyden, A., Microkinetic modeling of the decarboxylation and decarbonylation of propanoic acid over Pd(111) model surfaces based on parameters obtained from first principles. *Journal of Catalysis* **2013**, *305*, 56-66.
20. Yang, W.; Solomon, R. V.; Mamun, O.; Bond, J. Q.; Heyden, A., Investigation of the reaction mechanism of the hydrodeoxygenation of propionic acid over a Rh(111) surface: A first principles study. *Journal of Catalysis* **2020**, *391*, 98-110.
21. Barbier, J., Deactivation of reforming catalysts by coking - a review. *Applied Catalysis* **1986**, *23* (2), 225-243.
22. Yeh, T. M.; Hockstad, R. L.; Linic, S.; Savage, P. E., Hydrothermal decarboxylation of unsaturated fatty acids over PtSn_x/C catalysts. *Fuel* **2015**, *156*, 219-224.
23. Yeh, T.; Linic, S.; Savage, P. E., Deactivation of Pt Catalysts during Hydrothermal Decarboxylation of Butyric Acid. *ACS Sustainable Chemistry & Engineering* **2014**, *2* (10), 2399-2406.
24. Santillan-Jimenez, E.; Crocker, M., Catalytic deoxygenation of fatty acids and their derivatives to hydrocarbon fuels via decarboxylation/decarbonylation. *Journal of Chemical Technology & Biotechnology* **2012**, *87* (8), 1041-1050.
25. Loe, R.; Santillan-Jimenez, E.; Morgan, T.; Sewell, L.; Ji, Y.; Jones, S.; Isaacs, M. A.; Lee, A. F.; Crocker, M., Effect of Cu and Sn promotion on the catalytic deoxygenation of model and algal lipids to fuel-like hydrocarbons over supported Ni catalysts. *Applied Catalysis B: Environmental* **2016**, *191*, 147-156.
26. Kiméné, A.; Wojcieszak, R.; Paul, S.; Dumeignil, F., Catalytic decarboxylation of fatty acids to hydrocarbons over non-noble metal catalysts: the state of the art. *Journal of Chemical Technology & Biotechnology* **2019**, *94* (3), 658-669.
27. Simakova, I.; Simakova, O.; Mäki-Arvela, P.; Murzin, D. Y., Decarboxylation of fatty acids over Pd supported on mesoporous carbon. *Catalysis Today* **2010**, *150* (1), 28-31.

28. Fu, J.; Lu, X.; Savage, P. E., Hydrothermal decarboxylation and hydrogenation of fatty acids over Pt/C. *ChemSusChem* **2011**, *4* (4), 481-6.
29. Lestari, S.; Mäki-Arvela, P.; Simakova, I.; Beltramini, J.; Lu, G. Q. M.; Murzin, D. Y., Catalytic deoxygenation of stearic acid and palmitic acid in semibatch mode. *Catalysis Letters* **2009**, *130* (1-2), 48-51.
30. Yang, L.; Carreon, M. A., Deoxygenation of Palmitic and Lauric Acids over Pt/ZIF-67 Membrane/Zeolite 5A Bead Catalysts. *ACS Applied Materials & Interfaces* **2017**, *9* (37), 31993-32000.
31. Pham, T. N.; Shi, D.; Resasco, D. E., Reaction kinetics and mechanism of ketonization of aliphatic carboxylic acids with different carbon chain lengths over Ru/TiO₂ catalyst. *Journal of Catalysis* **2014**, *314*, 149-158.
32. Onishi, H.; Aruga, T.; Iwasawa, Y., Catalytic reactions on a metal oxide single crystal: switchover of the reaction paths in formic acid decomposition on titanium dioxide TiO₂(110). *Journal of the American Chemical Society* **1993**, *115* (22), 10460-10461.
33. Bates, S. P.; Kresse, G.; Gillan, M. J., The adsorption and dissociation of ROH molecules on TiO₂(110). *Surface Science* **1998**, *409* (2), 336-349.
34. Wang, C.-y.; Groenzin, H.; Shultz, M. J., Comparative Study of Acetic Acid, Methanol, and Water Adsorbed on Anatase TiO₂ Probed by Sum Frequency Generation Spectroscopy. *Journal of the American Chemical Society* **2005**, *127* (27), 9736-9744.
35. Maçôas, E. M. S.; Khriachtchev, L.; Pettersson, M.; Fausto, R.; Räsänen, M., Internal Rotation in Propionic Acid: Near-Infrared-Induced Isomerization in Solid Argon. *The Journal of Physical Chemistry A* **2005**, *109* (16), 3617-3625.
36. Fu, J.; Mei, D., A theoretical study of propionic acid decarboxylation over hydroxyapatite supported platinum catalysts. *Catalysis Today* **2021**, *365*, 181-192.
37. Kammert, J. D.; Chemburkar, A.; Miyake, N.; Neurock, M.; Davis, R. J., Reaction Kinetics and Mechanism for the Catalytic Reduction of Propionic Acid over Supported ReOx Promoted by Pd. *ACS Catalysis* **2021**, *11* (3), 1435-1455.
38. Perovskite Mineral Data.
<http://webmineral.com/data/Perovskite.shtml#.ZBbn7XbMKUk>.
39. Jeon, N. J.; Na, H.; Jung, E. H.; Yang, T.-Y.; Lee, Y. G.; Kim, G.; Shin, H.-W.; Il Seok, S.; Lee, J.; Seo, J., A fluorene-terminated hole-transporting material for highly efficient and stable perovskite solar cells. *Nature Energy* **2018**, *3* (8), 682-689.
40. Jena, A. K.; Kulkarni, A.; Miyasaka, T., Halide Perovskite Photovoltaics: Background, Status, and Future Prospects. *Chem Rev* **2019**, *119* (5), 3036-3103.
41. Kojima, A.; Teshima, K.; Shirai, Y.; Miyasaka, T., Organometal Halide Perovskites as Visible-Light Sensitizers for Photovoltaic Cells. *Journal of the American Chemical Society* **2009**, *131* (17), 6050-6051.
42. Green, M. A.; Dunlop, E. D.; Hohl-Ebinger, J.; Yoshita, M.; Kopidakis, N.; Ho-Baillie, A. W. Y., Solar cell efficiency tables (Version 55). *Progress in Photovoltaics: Research and Applications* **2020**, *28* (1), 3-15.
43. Stoumpos, C. C.; Malliakas, C. D.; Kanatzidis, M. G., Semiconducting tin and lead iodide perovskites with organic cations: phase transitions, high mobilities, and near-infrared photoluminescent properties. *Inorg Chem* **2013**, *52* (15), 9019-38.

44. Miyata, A.; Mitioglu, A.; Plochocka, P.; Portugall, O.; Wang, J. T.-W.; Stranks, S. D.; Snaith, H. J.; Nicholas, R. J., Direct measurement of the exciton binding energy and effective masses for charge carriers in organic–inorganic tri-halide perovskites. *Nature Physics* **2015**, *11* (7), 582-587.
45. Steirer, K. X.; Schulz, P.; Teeter, G.; Stevanovic, V.; Yang, M.; Zhu, K.; Berry, J. J., Defect Tolerance in Methylammonium Lead Triiodide Perovskite. *ACS Energy Letters* **2016**, *1* (2), 360-366.
46. Xing, G.; Mathews, N.; Lim, S. S.; Yantara, N.; Liu, X.; Sabba, D.; Grätzel, M.; Mhaisalkar, S.; Sum, T. C., Low-temperature solution-processed wavelength-tunable perovskites for lasing. *Nat Mater* **2014**, *13* (5), 476-80.
47. Sadhanala, A.; Ahmad, S.; Zhao, B.; Giesbrecht, N.; Pearce, P. M.; Deschler, F.; Hoyer, R. L.; Gödel, K. C.; Bein, T.; Docampo, P.; Dutton, S. E.; De Volder, M. F.; Friend, R. H., Blue-Green Color Tunable Solution Processable Organolead Chloride-Bromide Mixed Halide Perovskites for Optoelectronic Applications. *Nano Lett* **2015**, *15* (9), 6095-101.
48. Li, G.; Tan, Z.-K.; Di, D.; Lai, M. L.; Jiang, L.; Lim, J. H.-W.; Friend, R. H.; Greenham, N. C., Efficient Light-Emitting Diodes Based on Nanocrystalline Perovskite in a Dielectric Polymer Matrix. *Nano Letters* **2015**, *15* (4), 2640-2644.
49. Yang, Y.; Yang, M.; Moore, David T.; Yan, Y.; Miller, Elisa M.; Zhu, K.; Beard, Matthew C., Top and bottom surfaces limit carrier lifetime in lead iodide perovskite films. *Nature Energy* **2017**, *2* (2), 16207.
50. Murali, B.; Yengel, E.; Yang, C.; Peng, W.; Alarousu, E.; Bakr, O. M.; Mohammed, O. F., The Surface of Hybrid Perovskite Crystals: A Boon or Bane. *ACS Energy Letters* **2017**, *2* (4), 846-856.
51. Wang, J.; Fu, W.; Jariwala, S.; Sinha, I.; Jen, A. K. Y.; Ginger, D. S., Reducing Surface Recombination Velocities at the Electrical Contacts Will Improve Perovskite Photovoltaics. *ACS Energy Letters* **2019**, *4* (1), 222-227.
52. Sarritsu, V.; Sestu, N.; Marongiu, D.; Chang, X.; Masi, S.; Rizzo, A.; Colella, S.; Quochi, F.; Saba, M.; Mura, A.; Bongiovanni, G., Optical determination of Shockley-Read-Hall and interface recombination currents in hybrid perovskites. *Sci Rep* **2017**, *7*, 44629.
53. Stolterfoht, M.; Caprioglio, P.; Wolff, C. M.; Márquez, J. A.; Nordmann, J.; Zhang, S.; Rothhardt, D.; Hörmann, U.; Amir, Y.; Redinger, A.; Kegelmann, L.; Zu, F.; Albrecht, S.; Koch, N.; Kirchartz, T.; Saliba, M.; Unold, T.; Neher, D., The impact of energy alignment and interfacial recombination on the internal and external open-circuit voltage of perovskite solar cells. *Energy & Environmental Science* **2019**, *12* (9), 2778-2788.
54. Zhao, L.; Kerner, R. A.; Xiao, Z.; Lin, Y. L.; Lee, K. M.; Schwartz, J.; Rand, B. P., Redox Chemistry Dominates the Degradation and Decomposition of Metal Halide Perovskite Optoelectronic Devices. *ACS Energy Letters* **2016**, *1* (3), 595-602.
55. Manser, J. S.; Christians, J. A.; Kamat, P. V., Intriguing Optoelectronic Properties of Metal Halide Perovskites. *Chemical Reviews* **2016**, *116* (21), 12956-13008.
56. Li, T.; Chen, Z.; Wang, Y.; Tu, J.; Deng, X.; Li, Q.; Li, Z., Materials for Interfaces in Organic Solar Cells and Photodetectors. *ACS Applied Materials & Interfaces* **2020**, *12* (3), 3301-3326.

57. Lee, S.-K.; Rana, K.; Ahn, J.-H., Graphene Films for Flexible Organic and Energy Storage Devices. *The Journal of Physical Chemistry Letters* **2013**, *4* (5), 831-841.
58. Hu, Z.; Zhao, Y.; Zou, W.; Lu, Q.; Liao, J.; Li, F.; Shang, M.; Lin, L.; Liu, Z., Doping of Graphene Films: Open the way to Applications in Electronics and Optoelectronics. *Advanced Functional Materials* **2022**, *32* (42), 2203179.
59. Zhang, F.; Klein, C.; Longhi, E.; Barlow, S.; Marder, S. R.; Sarusi, G.; Kahn, A., Molecular-Reductant-Induced Control of a Graphene–Organic Interface for Electron Injection. *Chemistry of Materials* **2019**, *31* (17), 6624-6632.
60. Cowan, S. R.; Schulz, P.; Giordano, A. J.; Garcia, A.; MacLeod, B. A.; Marder, S. R.; Kahn, A.; Ginley, D. S.; Ratcliff, E. L.; Olson, D. C., Chemically Controlled Reversible and Irreversible Extraction Barriers Via Stable Interface Modification of Zinc Oxide Electron Collection Layer in Polycarbazole-based Organic Solar Cells. **2014**, *24*.
61. Xia, J.; Liang, C.; Mei, S.; Gu, H.; He, B.; Zhang, Z.; Liu, T.; Wang, K.; Wang, S.; Chen, S.; Cai, Y.; Xing, G., Deep surface passivation for efficient and hydrophobic perovskite solar cells. *Journal of Materials Chemistry A* **2021**, *9* (5), 2919-2927.
62. Boehm, A. M.; Liu, T.; Park, S. M.; Abtahi, A.; Graham, K. R., Influence of Surface Ligands on Energetics at FASnI₃/C60 Interfaces and Their Impact on Photovoltaic Performance. *ACS Applied Materials & Interfaces* **2020**, *12* (5), 5209-5218.
63. Park, S. M.; Abtahi, A.; Boehm, A. M.; Graham, K. R., Surface Ligands for Methylammonium Lead Iodide Films: Surface Coverage, Energetics, and Photovoltaic Performance. *ACS Energy Letters* **2020**, *5* (3), 799-806.
64. Shu, H.; Xia, J.; Yang, H.; Luo, J.; Wan, Z.; Malik, H. A.; Han, F.; Yao, X.; Jia, C., Self-Assembled Hydrophobic Molecule-Based Surface Modification: A Strategy to Improve Efficiency and Stability of Perovskite Solar Cells. *ACS Sustainable Chemistry & Engineering* **2020**, *8* (29), 10859-10869.
65. Gu, P.-Y.; Wang, N.; Wang, C.; Zhou, Y.; Long, G.; Tian, M.; Chen, W.; Sun, X. W.; Kanatzidis, M. G.; Zhang, Q., Pushing up the efficiency of planar perovskite solar cells to 18.2% with organic small molecules as the electron transport layer. *Journal of Materials Chemistry A* **2017**, *5* (16), 7339-7344.
66. Wang, B.; Iocozzia, J.; Zhang, M.; Ye, M.; Yan, S.; Jin, H.; Wang, S.; Zou, Z.; Lin, Z., The charge carrier dynamics, efficiency and stability of two-dimensional material-based perovskite solar cells. *Chemical Society Reviews* **2019**, *48* (18), 4854-4891.
67. Ravi, V. K.; Santra, P. K.; Joshi, N.; Chugh, J.; Singh, S. K.; Rensmo, H.; Ghosh, P.; Nag, A., Origin of the Substitution Mechanism for the Binding of Organic Ligands on the Surface of CsPbBr₃ Perovskite Nanocubes. *The Journal of Physical Chemistry Letters* **2017**, *8* (20), 4988-4994.
68. Wang, F.; Geng, W.; Zhou, Y.; Fang, H. H.; Tong, C. J.; Loi, M. A.; Liu, L. M.; Zhao, N., Phenylalkylamine Passivation of Organolead Halide Perovskites Enabling High-Efficiency and Air-Stable Photovoltaic Cells. *Adv Mater* **2016**, *28* (45), 9986-9992.
69. Mohd Yusoff, A. R. b.; Vasilopoulou, M.; Georgiadou, D. G.; Palilis, L. C.; Abate, A.; Nazeeruddin, M. K., Passivation and process engineering approaches of halide perovskite films for high efficiency and stability perovskite solar cells. *Energy & Environmental Science* **2021**, *14* (5), 2906-2953.

70. Li, J.; Duan, J.; Yang, X.; Duan, Y.; Yang, P.; Tang, Q., Review on recent progress of lead-free halide perovskites in optoelectronic applications. *Nano Energy* **2021**, *80*, 105526.
71. Fan, Q.; Biesold-McGee, G. V.; Ma, J.; Xu, Q.; Pan, S.; Peng, J.; Lin, Z., Lead-Free Halide Perovskite Nanocrystals: Crystal Structures, Synthesis, Stabilities, and Optical Properties. *Angewandte Chemie International Edition* **2020**, *59* (3), 1030-1046.
72. Shao, S.; Liu, J.; Portale, G.; Fang, H.-H.; Blake, G. R.; ten Brink, G. H.; Koster, L. J. A.; Loi, M. A., Highly Reproducible Sn-Based Hybrid Perovskite Solar Cells with 9% Efficiency. *Advanced Energy Materials* **2018**, *8* (4), 1702019.
73. Yu, B.-B.; Chen, Z.; Zhu, Y.; Wang, Y.; Han, B.; Chen, G.; Zhang, X.; Du, Z.; He, Z., Heterogeneous 2D/3D Tin-Halides Perovskite Solar Cells with Certified Conversion Efficiency Breaking 14%. *Advanced Materials* **2021**, *33* (36), 2102055.
74. Jiang, X.; Li, H.; Zhou, Q.; Wei, Q.; Wei, M.; Jiang, L.; Wang, Z.; Peng, Z.; Wang, F.; Zang, Z.; Xu, K.; Hou, Y.; Teale, S.; Zhou, W.; Si, R.; Gao, X.; Sargent, E. H.; Ning, Z., One-Step Synthesis of SnI₂·(DMSO)_x Adducts for High-Performance Tin Perovskite Solar Cells. *Journal of the American Chemical Society* **2021**, *143* (29), 10970-10976.
75. Pascual, J.; Nasti, G.; Aldamasy, M. H.; Smith, J. A.; Flatken, M.; Phung, N.; Di Girolamo, D.; Turren-Cruz, S.-H.; Li, M.; Dallmann, A.; Avolio, R.; Abate, A., Origin of Sn(ii) oxidation in tin halide perovskites. *Materials Advances* **2020**, *1* (5), 1066-1070.
76. Aftab, A.; Ahmad, M. I., A review of stability and progress in tin halide perovskite solar cell. *Solar Energy* **2021**, *216*, 26-47.
77. Pazoki, M.; Jacobsson, T. J.; Hagfeldt, A.; Boschloo, G.; Edvinsson, T., Effect of metal cation replacement on the electronic structure of metalorganic halide perovskites: Replacement of lead with alkaline-earth metals. *Physical Review B* **2016**, *93* (14), 144105.
78. Castelli, I. E.; García-Lastra, J. M.; Thygesen, K. S.; Jacobsen, K. W., Bandgap calculations and trends of organometal halide perovskites. *APL Materials* **2014**, *2* (8), 081514.
79. Peng, L.; Xie, W., Theoretical and experimental investigations on the bulk photovoltaic effect in lead-free perovskites MASnI₃ and FASnI₃. *RSC Advances* **2020**, *10* (25), 14679-14688.
80. Shi, T.; Zhang, H.-S.; Meng, W.; Teng, Q.; Liu, M.; Yang, X.; Yan, Y.; Yip, H.-L.; Zhao, Y.-J., Effects of organic cations on the defect physics of tin halide perovskites. *Journal of Materials Chemistry A* **2017**, *5* (29), 15124-15129.
81. Zhao, Z.; Gu, F.; Li, Y.; Sun, W.; Ye, S.; Rao, H.; Liu, Z.; Bian, Z.; Huang, C., Mixed-Organic-Cation Tin Iodide for Lead-Free Perovskite Solar Cells with an Efficiency of 8.12%. *Advanced Science* **2017**, *4* (11), 1700204.
82. Ke, W.; Stoumpos, C. C.; Zhu, M.; Mao, L.; Spanopoulos, I.; Liu, J.; Kontsevoi, O. Y.; Chen, M.; Sarma, D.; Zhang, Y.; Wasielewski, M. R.; Kanatzidis, M. G., Enhanced photovoltaic performance and stability with a new type of hollow 3D perovskite {en}FASnI₃. *Science Advances* **2017**, *3* (8), e1701293.
83. Saitoh, T.; Matsudo, T.; Matsubara, C., Micelle-mediated extraction for concentrating hydrophobic organic compounds. *Journal of Chromatography A* **2000**, *879* (2), 121-128.

84. Cheng, Y.-J.; Yang, S.-H.; Hsu, C.-S., Synthesis of Conjugated Polymers for Organic Solar Cell Applications. *Chemical Reviews* **2009**, *109* (11), 5868-5923.
85. Yang, S.; Wang, Y.; Liu, P.; Cheng, Y.-B.; Zhao, H. J.; Yang, H. G., Functionalization of perovskite thin films with moisture-tolerant molecules. *Nature Energy* **2016**, *1* (2), 15016.
86. Li, X.; Dar, M. I.; Yi, C.; Luo, J.; Tschumi, M.; Zakeeruddin, S. M.; Nazeeruddin, M. K.; Han, H.; Grätzel, M., Improved performance and stability of perovskite solar cells by crystal crosslinking with alkylphosphonic acid ω -ammonium chlorides. *Nat Chem* **2015**, *7* (9), 703-11.
87. Noel, N. K.; Abate, A.; Stranks, S. D.; Parrott, E. S.; Burlakov, V. M.; Goriely, A.; Snaith, H. J., Enhanced Photoluminescence and Solar Cell Performance via Lewis Base Passivation of Organic-Inorganic Lead Halide Perovskites. *ACS Nano* **2014**, *8* (10), 9815-9821.
88. Lackner, K. S., A Guide to CO₂ Sequestration. *Science* **2003**, *300* (5626), 1677-1678.
89. Khoo, H. H.; Tan, R. B. H., Life Cycle Investigation of CO₂ Recovery and Sequestration. *Environmental Science & Technology* **2006**, *40* (12), 4016-4024.
90. Agarwal, A. S.; Zhai, Y.; Hill, D.; Sridhar, N., The Electrochemical Reduction of Carbon Dioxide to Formate/Formic Acid: Engineering and Economic Feasibility. *ChemSusChem* **2011**, *4* (9), 1301-1310.
91. Qiao, J.; Liu, Y.; Hong, F.; Zhang, J., A review of catalysts for the electroreduction of carbon dioxide to produce low-carbon fuels. *Chemical Society Reviews* **2014**, *43* (2), 631-675.
92. Windle, C. D.; Perutz, R. N., Advances in Molecular Photocatalytic and Electrocatalytic CO₂ Reduction. *Coord. Chem. Rev.* **2012**, *256* (21), 2562.
93. Costentin, C.; Robert, M.; Savéant, J. M., Catalysis of the Electrochemical Reduction of Carbon Dioxide. *Chem. Soc. Rev.* **2013**, *42*, 2423.
94. Kinzel, N. W.; Werlé, C.; Leitner, W., Transition Metal Complexes as Catalysts for the Electroconversion of CO₂: An Organometallic Perspective. *Angewandte Chemie International Edition* **2021**, *60* (21), 11628-11686.
95. Osborn, J. A.; Wilkinson, G.; Mrowca, J. J., Tris(triphenylphosphine)halorhodium(I). In *Inorganic Syntheses*, 1967; pp 67-71.
96. Sampaio, R. N.; Grills, D. C.; Polyansky, D. E.; Szalda, D. J.; Fujita, E., Unexpected Roles of Triethanolamine in the Photochemical Reduction of CO₂ to Formate by Ruthenium Complexes. *Journal of the American Chemical Society* **2020**, *142* (5), 2413-2428.
97. Sekizawa, K.; Sato, S.; Arai, T.; Morikawa, T., Solar-Driven Photocatalytic CO₂ Reduction in Water Utilizing a Ruthenium Complex Catalyst on p-Type Fe₂O₃ with a Multiheterojunction. *ACS Catalysis* **2018**, *8* (2), 1405-1416.
98. Ishida, H.; Tanaka, K.; Tanaka, T., Electrochemical CO₂ reduction catalyzed by ruthenium complexes [Ru(bpy)₂(CO)₂]²⁺ and [Ru(bpy)₂(CO)Cl]⁺. Effect of pH on the formation of CO and HCOO. *Organometallics* **1987**, *6* (1), 181-186.

99. Chen, Z.; Chen, C.; Weinberg, D. R.; Kang, P.; Concepcion, J. J.; Harrison, D. P.; Brookhart, M. S.; Meyer, T. J., Electrocatalytic reduction of CO₂ to CO by polypyridyl ruthenium complexes. *Chemical Communications* **2011**, 47 (47), 12607-12609.
100. Fachinetti, G.; Fochi, G.; Funaioli, T.; Zanazzi, P. F., Isolation of a tetranuclear iron cluster promoting CO₂ reduction and intermediate to iron carbonyl disproportionation. *Journal of the Chemical Society, Chemical Communications* **1987**, (2), 89-90.
101. Grodkowski, J.; Dhanasekaran, T.; Neta, P.; Hambright, P.; Brunschwig, B. S.; Shinozaki, K.; Fujita, E., Reduction of Cobalt and Iron Phthalocyanines and the Role of the Reduced Species in Catalyzed Photoreduction of CO₂. *The Journal of Physical Chemistry A* **2000**, 104 (48), 11332-11339.
102. Grodkowski, J.; Behar, D.; Neta, P.; Hambright, P., Iron Porphyrin-Catalyzed Reduction of CO₂. Photochemical and Radiation Chemical Studies. *The Journal of Physical Chemistry A* **1997**, 101 (3), 248-254.
103. Yuan, H.; Du, J.; Ming, M.; Chen, Y.; Jiang, L.; Han, Z., Combination of Organic Dye and Iron for CO₂ Reduction with Pentanuclear Fe₂Na₃ Purpurin Photocatalysts. *Journal of the American Chemical Society* **2022**, 144 (10), 4305-4309.
104. Ogata, T.; Yanagida, S.; Brunschwig, B. S.; Fujita, E., Mechanistic and Kinetic Studies of Cobalt Macrocycles in a Photochemical CO₂ Reduction System: Evidence of Co-CO₂ Adducts as Intermediates. *Journal of the American Chemical Society* **1995**, 117 (25), 6708-6716.
105. Behar, D.; Dhanasekaran, T.; Neta, P.; Hosten, C. M.; Ejeh, D.; Hambright, P.; Fujita, E., Cobalt Porphyrin Catalyzed Reduction of CO₂. Radiation Chemical, Photochemical, and Electrochemical Studies. *The Journal of Physical Chemistry A* **1998**, 102 (17), 2870-2877.
106. Rudolph, M.; Dautz, S.; Jäger, E.-G., Macrocyclic [N₄₂-] Coordinated Nickel Complexes as Catalysts for the Formation of Oxalate by Electrochemical Reduction of Carbon Dioxide. *Journal of the American Chemical Society* **2000**, 122 (44), 10821-10830.
107. Beley, M.; Collin, J.-P.; Ruppert, R.; Sauvage, J.-P., Nickel(II)-cyclam: an extremely selective electrocatalyst for reduction of CO₂ in water. *Journal of the Chemical Society, Chemical Communications* **1984**, (19), 1315-1316.
108. Christensen, P.; Hamnett, A.; Muir, A. V. G.; Timney, J. A., An in Situ Infrared Study of CO₂ Reduction Catalysed by Rhenium Tricarbonyl Bipyridyl Derivatives. *J. Chem. Soc., Dalton Trans.* **1992**, (9), 1455.
109. Ishitani, O.; George, M. W.; Ibusuki, T.; Johnson, F. P. A.; Koike, K.; Nozaki, K.; Pac, C.; Turner, J. J.; Westwell, J. R., Photophysical Behavior of a New CO₂ Reduction Catalyst, Re(CO)₂(bpy){P(OEt)₃}₂⁺. *Inorganic Chemistry* **1994**, 33 (21), 4712-4717.
110. Koike, K.; Hori, H.; Ishizuka, M.; Westwell, J. R.; Takeuchi, K.; Ibusuki, T.; Enjouji, K.; Konno, H.; Sakamoto, K.; Ishitani, O., Key Process of the Photocatalytic Reduction of CO₂ Using [Re(4,4'-X₂-bipyridine)(CO)₃PR₃]⁺ (X = CH₃, H, CF₃; PR₃ = Phosphorus Ligands): Dark Reaction of the One-Electron-Reduced Complexes with CO₂. *Organometallics* **1997**, 16 (26), 5724-5729.
111. Hisao, H.; Kazuhide, K.; Koji, T.; Yoshiyuki, S., Rhenium-Mediated Photochemical Carbon Dioxide Reduction in Compressed Carbon Dioxide. *Chemistry Letters* **2000**, 29 (5), 522-523.

112. Koenig, J. D. B.; Dubrawski, Z. S.; Rao, K. R.; Willkomm, J.; Gelfand, B. S.; Risko, C.; Piers, W. E.; Welch, G. C., Lowering Electrocatalytic CO₂ Reduction Overpotential Using N-Annulated Perylene Diimide Rhenium Bipyridine Dyads with Variable Tether Length. *Journal of the American Chemical Society* **2021**, *143* (40), 16849-16864.
113. Hawecker, J.; Lehn, J. M.; Ziessel, R., Electrocatalytic Reduction of Carbon Dioxide Mediated by Re(Bipy)(CO)₃Cl (Bipy = 2,2'-Bipyridine). *J. Chem. Soc., Chem. Commun.* **1984**, 0 (6), 328.
114. Franco, F.; Cometto, C.; Garino, C.; Minero, C.; Sordello, F.; Nervi, C.; Gobetto, R., Photo- and Electrocatalytic Reduction of CO₂ by [Re(CO)₃α,A'-Diimine-(4-Piperidinyl-1,8-Naphthalimide)Cl] Complexes. *Eur. J. Inorg. Chem.* **2015**, *2015* (2), 296.
115. Martinez, J. F.; La Porte, N. T.; Chaudhuri, S.; Sinopoli, A.; Bae, Y. J.; Sohail, M.; Batista, V. S.; Wasielewski, M. R., Effect of Electronic Coupling on Electron Transfer Rates from Photoexcited Naphthalenediimide Radical Anion to Re(Bpy)(CO)₃X. *J. Phys. Chem. C* **2019**, *123* (16), 10178.
116. Martinez, J. F.; La Porte, N. T.; Wasielewski, M. R., Electron Transfer from Photoexcited Naphthalene-1,4:5,8-Bis(Dicarboximide) Radical Anion to Mn(Bpy)(CO)₃X and Re(Bpy)(CO)₃X CO₂ Reduction Catalysts Linked via a Saturated Methylene Bridge. *J. Photochem. Photobiol., A* **2019**, *372*, 21.
117. Martinez, J. F.; La Porte, N. T.; Wasielewski, M. R., Electron Transfer from Photoexcited Naphthalene Diimide Radical Anion to Electrocatalytically Active Re(Bpy)(CO)₃Cl in a Molecular Triad. *J. Phys. Chem. C* **2018**, *122* (5), 2608.
118. Hedström, S.; Chaudhuri, S.; La Porte, N. T.; Rudshiteyn, B.; Martinez, J. F.; Wasielewski, M. R.; Batista, V. S., Thousandfold Enhancement of Photoreduction Lifetime in Re(Bpy)(CO)₃ via Spin-Dependent Electron Transfer from a Perylenediimide Radical Anion Donor. *J. Am. Chem. Soc.* **2017**, *139* (46), 16466.
119. Porte, N. T. L.; Martinez, J. F.; Hedström, S.; Rudshiteyn, B.; Phelan, B. T.; Mauck, C. M.; Young, R. M.; Batista, V. S.; Wasielewski, M. R., Photoinduced Electron Transfer from Rylenediimide Radical Anions and Dianions to Re(Bpy)(CO)₃ Using Red and near-Infrared Light. *Chem. Sci.* **2017**, *8* (5), 3821.
120. Liu, Z.; Wu, Y.; Zhang, Q.; Gao, X., Non-fullerene small molecule acceptors based on perylene diimides. *Journal of Materials Chemistry A* **2016**, *4* (45), 17604-17622.
121. Chen, W.; Zhang, Q., Recent Progress in Non-Fullerene Small Molecule Acceptors in Organic Solar Cells (OSCs). *J. Mater. Chem. C* **2017**, *5* (6), 1275.
122. Milton, M.; Cheng, Q.; Yang, Y.; Nuckolls, C.; Hernández Sánchez, R.; Sisto, T. J., Molecular Materials for Nonaqueous Flow Batteries with a High Coulombic Efficiency and Stable Cycling. *Nano Lett.* **2017**, *17* (12), 7859.
123. Koenig, J. D. B.; Laventure, A.; Welch, G. C., Harnessing Direct (Hetero)Arylation in Pursuit of a Saddle-Shaped Perylene Diimide Tetramer. *ACS Appl. Energy Mater.* **2019**, *2* (12), 8939.
124. Cann, J. R.; Cabanetos, C.; Welch, G. C., Synthesis of Molecular Dyads and Triads Based Upon N-Annulated Perylene Diimide Monomers and Dimers. *Eur. J. Org. Chem.* **2018**, *2018* (48), 6933.
125. Vespa, M.; Cann, J. R.; Dayneko, S. V.; Melville, O. A.; Hendsbee, A. D.; Zou, Y.; Lessard, B. H.; Welch, G. C., Synthesis of a Perylene Diimide Dimer with Pyrrolic N-H

Bonds and N-Functionalized Derivatives for Organic Field-Effect Transistors and Organic Solar Cells. *Eur. J. Org. Chem.* **2018**, 2018 (33), 4592.

126. Hendsbee, A. D.; Sun, J. P.; Law, W. K.; Yan, H.; Hill, I. G.; Spasyuk, D. M.; Welch, G. C., Synthesis, Self-Assembly, and Solar Cell Performance of N-Annulated Perylene Diimide Non-Fullerene Acceptors. *Chem. Mater.* **2016**, 28 (19), 7098.

127. Costentin, C.; Robert, M.; Savéant, J.-M., Catalysis of the electrochemical reduction of carbon dioxide. *Chemical Society Reviews* **2013**, 42 (6), 2423-2436.

128. Wiberg, C.; Busch, M.; Evenäs, L.; Ahlberg, E., The Electrochemical Response of Core-Functionalized Naphthalene Diimides (NDI) - a Combined Computational and Experimental Investigation. *Electrochim. Acta* **2021**, 367, 137480.

129. Salvatore, D.; Berlinguette, C. P., Voltage Matters When Reducing CO₂ in an Electrochemical Flow Cell. *ACS Energy Lett.* **2020**, 5 (1), 215.

130. Kibria, M. G.; Edwards, J. P.; Gabardo, C. M.; Dinh, C. T.; Seifitokaldani, A.; Sinton, D.; Sargent, E. H., Electrochemical CO₂ Reduction into Chemical Feedstocks: From Mechanistic Electrocatalysis Models to System Design. *Adv. Mater.* **2019**, 31 (31), 1807166.

131. Kamata, R.; Kumagai, H.; Yamazaki, Y.; Sahara, G.; Ishitani, O., Photoelectrochemical CO₂ Reduction Using a Ru(II)-Re(I) Supramolecular Photocatalyst Connected to a Vinyl Polymer on a NiO Electrode. *ACS Appl. Mater. Interfaces* **2019**, 11 (6), 5632.

132. Qiao, X.; Li, Q.; Schauggaard, R. N.; Noffke, B. W.; Liu, Y.; Li, D.; Liu, L.; Raghavachari, K.; Li, L., Well-Defined Nanographene-Rhenium Complex as an Efficient Electrocatalyst and Photocatalyst for Selective CO₂ Reduction. *J. Am. Chem. Soc.* **2017**, 139 (11), 3934.

133. Costentin, C.; Drouet, S.; Robert, M.; Savéant, J. M., A Local Proton Source Enhances CO₂ Electroreduction to CO by a Molecular Fe Catalyst. *Science* **2012**, 338 (6103), 90.

134. Takeda, H.; Cometto, C.; Ishitani, O.; Robert, M., Electrons, Photons, Protons and Earth-Abundant Metal Complexes for Molecular Catalysis of CO₂ Reduction. *ACS Catal.* **2017**, 7 (1), 70.

135. Davethu, P. A.; de Visser, S. P., CO₂ Reduction on an Iron-Porphyrin Center: A Computational Study. *The Journal of Physical Chemistry A* **2019**, 123 (30), 6527-6535.

136. Yamazaki, Y.; Ohkubo, K.; Saito, D.; Yatsu, T.; Tamaki, Y.; Tanaka, S.; Koike, K.; Onda, K.; Ishitani, O., Kinetics and Mechanism of Intramolecular Electron Transfer in Ru(II)-Re(I) Supramolecular CO₂-Reduction Photocatalysts: Effects of Bridging Ligands. *Inorg. Chem.* **2019**, 58 (17), 11480.

137. Koike, K.; Grills, D. C.; Tamaki, Y.; Fujita, E.; Okubo, K.; Yamazaki, Y.; Saigo, M.; Mukuta, T.; Onda, K.; Ishitani, O., Investigation of Excited State, Reductive Quenching, and Intramolecular Electron Transfer of Ru(II)-Re(I) Supramolecular Photocatalysts for CO₂ Reduction Using Time-Resolved IR Measurements. *Chem. Sci.* **2018**, 9 (11), 2961.

138. Benson, E. E.; Kubiak, C. P.; Sathrum, A. J.; Smieja, J. M., Electrocatalytic and homogeneous approaches to conversion of CO₂ to liquid fuels. *Chemical Society Reviews* **2009**, 38 (1), 89-99.

139. Froehlich, J. D.; Kubiak, C. P., The Homogeneous Reduction of CO₂ by [Ni(cyclam)]⁺: Increased Catalytic Rates with the Addition of a CO Scavenger. *Journal of the American Chemical Society* **2015**, *137* (10), 3565-3573.
140. Benson Eric, E.; Sampson Matthew, D.; Grice Kyle, A.; Smieja Jonathan, M.; Froehlich Jesse, D.; Friebel, D.; Keith John, A.; Carter Emily, A.; Nilsson, A.; Kubiak Clifford, P., The Electronic States of Rhenium Bipyridyl Electrocatalysts for CO₂ Reduction as Revealed by X-ray Absorption Spectroscopy and Computational Quantum Chemistry. *Angew. Chem., Int. Ed.* **2013**, *52* (18), 4841.
141. Manbeck, G. F.; Muckerman, J. T.; Szalda, D. J.; Himeda, Y.; Fujita, E., Push or Pull? Proton Responsive Ligand Effects in Rhenium Tricarbonyl CO₂ Reduction Catalysts. *The Journal of Physical Chemistry B* **2015**, *119* (24), 7457-7466.
142. Lee, J. G., Computational Materials Science: An Introduction. CRC Press: 2011; pp 197-238.
143. Sholl, D.; Steckel, J. A., Density Functional Theory: A Practical Introduction. Wiley: 2011; pp 93-110.
144. Burke, K.; Perdew, J. P.; Wang, Y., Derivation of a Generalized Gradient Approximation: The PW91 Density Functional. In *Electronic Density Functional Theory: Recent Progress and New Directions*, Dobson, J. F.; Vignale, G.; Das, M. P., Eds. Springer US: Boston, MA, 1998; pp 81-111.
145. Perdew, J. P.; Burke, K.; Ernzerhof, M., Generalized Gradient Approximation Made Simple. *Physical Review Letters* **1996**, *77* (18), 3865-3868.
146. Kresse, G.; Joubert, D., From ultrasoft pseudopotentials to the projector augmented-wave method. *Physical Review B* **1999**, *59* (3), 1758-1775.
147. Henkelman, G.; Uberuaga, B. P.; Jónsson, H., A climbing image nudged elastic band method for finding saddle points and minimum energy paths. *The Journal of Chemical Physics* **2000**, *113* (22), 9901-9904.
148. Henkelman, G.; Jónsson, H., A dimer method for finding saddle points on high dimensional potential surfaces using only first derivatives. *The Journal of Chemical Physics* **1999**, *111* (15), 7010-7022.
149. Olsen, R. A.; Kroes, G. J.; Henkelman, G.; Arnaldsson, A.; Jónsson, H., Comparison of methods for finding saddle points without knowledge of the final states. *The Journal of Chemical Physics* **2004**, *121* (20), 9776-9792.
150. Berne, B. J.; Ciccotti, G.; Coker, D. F., *Classical And Quantum Dynamics In Condensed Phase Simulations: Proceedings Of The International School Of Physics*. World Scientific Publishing Company: 1998.
151. Filot, I. A. W., Introduction to microkinetic modeling. Technische Universiteit Eindhoven, 2018; pp 1-227.
152. Rao, K. R.; Pace, R. B.; Suarez, H.; Santillan-Jimenez, E.; Risko, C., Carboxylic Acid Decarbonylation on Nickel: The Critical Role of the Acid Binding Geometry. *ACS Catalysis* **2023**, *13* (13), 9102-9112.
153. Silva, G. C. R.; Qian, D.; Pace, R.; Heintz, O.; Caboche, G.; Santillan-Jimenez, E.; Crocker, M., Promotional Effect of Cu, Fe and Pt on the Performance of Ni/Al₂O₃ in the Deoxygenation of Used Cooking Oil to Fuel-Like Hydrocarbons. *Catalysts* **2020**, *10* (1), 91.

154. Zhang, Z.; Lin, W.; Li, Y.; Okejiri, F.; Lu, Y.; Liu, J.; Chen, H.; Lu, X.; Fu, J., Heterogeneous Non-noble Catalyst for Highly Selective Production of Linear α -Olefins from Fatty Acids: A Discovery of NiFe/C. *ChemSusChem* **2020**, *13* (18), 4922-4928.
155. Han, Q.; Rehman, M. U.; Wang, J.; Rykov, A.; Gutiérrez, O. Y.; Zhao, Y.; Wang, S.; Ma, X.; Lercher, J. A., The synergistic effect between Ni sites and Ni-Fe alloy sites on hydrodeoxygenation of lignin-derived phenols. *Applied Catalysis B: Environmental* **2019**, *253*, 348-358.
156. Kresse, G.; Hafner, J., Ab initio molecular dynamics for liquid metals. *Physical Review B* **1993**, *47* (1), 558-561.
157. Kresse, G.; Furthmüller, J., Efficiency of ab-initio total energy calculations for metals and semiconductors using a plane-wave basis set. *Computational Materials Science* **1996**, *6* (1), 15-50.
158. Press, W. H.; Teukolsky, S. A.; Vetterling, W. T.; Flannery, B. P., NUMERICAL RECIPES The Art of Scientific Computing. 3rd Edition ed.; Cambridge University Press: New York, 1986; pp 515-520.
159. Gussoni, M.; Rui, M.; Zerbi, G., Electronic and relaxation contribution to linear molecular polarizability. An analysis of the experimental values. *Journal of Molecular Structure* **1998**, *447* (3), 163-215.
160. Wang, S.-G.; Cao, D.-B.; Li, Y.-W.; Wang, J.; Jiao, H., CO₂ Reforming of CH₄ on Ni(111): A Density Functional Theory Calculation. *The Journal of Physical Chemistry B* **2006**, *110* (20), 9976-9983.
161. Breidi, A.; Fries, S. G.; Ruban, A. V., Ideal compressive strength of fcc Co, Ni, and Ni-rich alloys along the $\langle 001 \rangle$ direction: A first-principles study. *Physical Review B* **2016**, *93* (14), 144106.
162. Connétable, D.; Maugis, P., Effect of stress on vacancy formation and diffusion in fcc systems: comparison between DFT calculations and elasticity theory. *Acta Materialia* **2020**, 869-882.
163. Liu, X. D.; Zhang, H. Y.; Lu, K.; Hu, Z. Q., The lattice expansion in nanometre-sized Ni polycrystals. *Journal of Physics: Condensed Matter* **1994**, *6* (34), L497-L501.
164. Li, H.; Ebrahimi, F., Synthesis and characterization of electrodeposited nanocrystalline nickel-iron alloys. *Materials Science and Engineering: A* **2003**, *347* (1), 93-101.
165. Henkelman, G.; Jóhannesson, G.; Jónsson, H., Methods for Finding Saddle Points and Minimum Energy Paths. In *Theoretical Methods in Condensed Phase Chemistry*, Schwartz, S. D., Ed. Springer Netherlands: Dordrecht, 2002; pp 269-302.
166. Grimme, S., Accurate description of van der Waals complexes by density functional theory including empirical corrections. *Journal of Computational Chemistry* **2004**, *25* (12), 1463-1473.
167. Yildirim, H.; Greber, T.; Kara, A., Trends in Adsorption Characteristics of Benzene on Transition Metal Surfaces: Role of Surface Chemistry and van der Waals Interactions. *The Journal of Physical Chemistry C* **2013**, *117* (40), 20572-20583.
168. Tereshchuk, P.; Da Silva, J. L. F., Ethanol and Water Adsorption on Close-Packed 3d, 4d, and 5d Transition-Metal Surfaces: A Density Functional Theory Investigation with

- van der Waals Correction. *The Journal of Physical Chemistry C* **2012**, *116* (46), 24695-24705.
169. Liu, B.; Cheng, L.; Curtiss, L.; Greeley, J., Effects of van der Waals density functional corrections on trends in furfural adsorption and hydrogenation on close-packed transition metal surfaces. *Surface Science* **2014**, *622*, 51-59.
170. Silvestrelli, P. L.; Ambrosetti, A., Inclusion of screening effects in the van der Waals corrected DFT simulation of adsorption processes on metal surfaces. *Physical Review B* **2013**, *87* (7), 075401.
171. Hensley, A. J. R.; Ghale, K.; Rieg, C.; Dang, T.; Anderst, E.; Studt, F.; Campbell, C. T.; McEwen, J.-S.; Xu, Y., DFT-Based Method for More Accurate Adsorption Energies: An Adaptive Sum of Energies from RPBE and vdW Density Functionals. *The Journal of Physical Chemistry C* **2017**, *121* (9), 4937-4945.
172. Webb, G., The formation and role of carbonaceous residues in metal-catalysed reactions of hydrocarbons. *Catalysis Today* **1990**, *7* (2), 139-155.
173. Motagamwala, A. H.; Dumesic, J. A., Microkinetic Modeling: A Tool for Rational Catalyst Design. *Chemical Reviews* **2021**, *121* (2), 1049-1076.
174. Linstrom, P. J.; Mallard, W. G., The NIST Chemistry WebBook: A Chemical Data Resource on the Internet. *Journal of Chemical & Engineering Data* **2001**, *46* (5), 1059-1063.
175. Henkelman, G. VTST tools. <http://theory.cm.utexas.edu/>.
176. Sock, M.; Eichler, A.; Surnev, S.; Andersen, J. N.; Klötzer, B.; Hayek, K.; Ramsey, M. G.; Netzer, F. P., High-resolution electron spectroscopy of different adsorption states of ethylene on Pd(111). *Surface Science* **2003**, *545* (1), 122-136.
177. Gabasch, H.; Hayek, K.; Klötzer, B.; Knop-Gericke, A.; Schlögl, R., Carbon Incorporation in Pd(111) by Adsorption and Dehydrogenation of Ethene. *The Journal of Physical Chemistry B* **2006**, *110* (10), 4947-4952.
178. Jungwirthová, I.; Kesmodel, L. L., Thermal Evolution of Acetylene Overlayers on Pd(111). *The Journal of Physical Chemistry B* **2001**, *105* (3), 674-680.
179. Behtash, S.; Lu, J.; Mamun, O.; Williams, C. T.; Monnier, J. R.; Heyden, A., Solvation Effects in the Hydrodeoxygenation of Propanoic Acid over a Model Pd(211) Catalyst. *The Journal of Physical Chemistry C* **2016**, *120* (5), 2724-2736.
180. Neurock, M., The microkinetics of heterogeneous catalysis. By J. A. Dumesic, D. F. Rudd, L. M. Aparicio, J. E. Rekoske, and A. A. Treviño, ACS Professional Reference Book, American Chemical Society, Washington, DC, 1993, 315 pp. *AIChE Journal* **1994**, *40* (6), 1085-1087.
181. Lugo-José, Y. K.; Monnier, J. R.; Williams, C. T., Gas-phase, catalytic hydrodeoxygenation of propanoic acid, over supported group VIII noble metals: Metal and support effects. *Applied Catalysis A: General* **2014**, *469*, 410-418.
182. Demir, B.; Kropp, T.; Rivera-Dones, K. R.; Gilcher, E. B.; Huber, G. W.; Mavrikakis, M.; Dumesic, J. A., A self-adjusting platinum surface for acetone hydrogenation. *Proceedings of the National Academy of Sciences* **2020**, *117* (7), 3446-3450.

183. Campbell, C. T., Finding the Rate-Determining Step in a Mechanism: Comparing DeDonder Relations with the “Degree of Rate Control”. *Journal of Catalysis* **2001**, *204* (2), 520-524.
184. Stegelmann, C.; Andreasen, A.; Campbell, C. T., Degree of Rate Control: How Much the Energies of Intermediates and Transition States Control Rates. *Journal of the American Chemical Society* **2009**, *131* (23), 8077-8082.
185. Motagamwala, A. H.; Ball, M. R.; Dumesic, J. A., Microkinetic Analysis and Scaling Relations for Catalyst Design. *Annual Review of Chemical and Biomolecular Engineering* **2018**, *9* (1), 413-450.
186. Paniagua, S. A.; Giordano, A. J.; Smith, O. N. L.; Barlow, S.; Li, H.; Armstrong, N. R.; Pemberton, J. E.; Brédas, J.-L.; Ginger, D.; Marder, S. R., Phosphonic Acids for Interfacial Engineering of Transparent Conductive Oxides. *Chemical Reviews* **2016**, *116* (12), 7117-7158.
187. Lee, J.; Jung, B.-J.; Lee, J.-I.; Chu, H. Y.; Do, L.-M.; Shim, H.-K., Modification of an ITO anode with a hole-transporting SAM for improved OLED device characteristics. *Journal of Materials Chemistry* **2002**, *12* (12), 3494-3498.
188. Hotchkiss, P. J.; Jones, S. C.; Paniagua, S. A.; Sharma, A.; Kippelen, B.; Armstrong, N. R.; Marder, S. R., The modification of indium tin oxide with phosphonic acids: mechanism of binding, tuning of surface properties, and potential for use in organic electronic applications. *Acc Chem Res* **2012**, *45* (3), 337-46.
189. Koh, S. E.; McDonald, K. D.; Holt, D. H.; Dulcey, C. S.; Chaney, J. A.; Pehrsson, P. E., Phenylphosphonic acid functionalization of indium tin oxide: surface chemistry and work functions. *Langmuir* **2006**, *22* (14), 6249-55.
190. Satoh, T.; Imanishi, M.; Nishikawa, T.; Mori, T., Properties of Interface between Organic Hole-Transporting Layer and Indium Tin Oxide Anode Modified by Fluorinated Self-Assembled Monolayer. *Japanese Journal of Applied Physics* **2012**, *51* (3R), 035701.
191. Benneckendorf, F. S.; Hillebrandt, S.; Ullrich, F.; Rohnacher, V.; Hietzschold, S.; Jänsch, D.; Freudenberg, J.; Beck, S.; Mankel, E.; Jaegermann, W.; Pucci, A.; Bunz, U. H. F.; Müllen, K., Structure–Property Relationship of Phenylene-Based Self-Assembled Monolayers for Record Low Work Function of Indium Tin Oxide. *The Journal of Physical Chemistry Letters* **2018**, *9* (13), 3731-3737.
192. He, S.-M.; Lin, H.-Y.; Shen, C.-J.; Su, C.-Y., Wrinkle-Free Graphene Films on Fluorinated Self-Assembled Monolayer-Modified Substrates for Enhancing the Electrical Performance of Transistors. *ACS Applied Nano Materials* **2022**, *5* (4), 5793-5802.
193. Ku, G. M.; Lee, E.; Kang, B.; Lee, J. H.; Cho, K.; Lee, W. H., Relationship between the dipole moment of self-assembled monolayers incorporated in graphene transistors and device electrical stabilities. *RSC Advances* **2017**, *7* (43), 27100-27104.
194. Newton, L.; Slater, T.; Clark, N.; Vijayaraghavan, A., Self assembled monolayers (SAMs) on metallic surfaces (gold and graphene) for electronic applications. *Journal of Materials Chemistry C* **2013**, *1* (3), 376-393.
195. Kresse, G.; Furthmüller, J., Efficient iterative schemes for ab initio total-energy calculations using a plane-wave basis set. *Physical Review B* **1996**, *54* (16), 11169-11186.
196. Press, W. H.; Teukolsky, S. A.; Vetterling, W. T.; Flannery, B. P., NUMERICAL RECIPES The Art of Scientific Computing. . *Cambridge University Press: New York* **1986**.

197. Dudarev, S. L.; Botton, G. A.; Savrasov, S. Y.; Humphreys, C. J.; Sutton, A. P., Electron-energy-loss spectra and the structural stability of nickel oxide: An LSDA+U study. *Physical Review B* **1998**, *57* (3), 1505-1509.
198. Zhu, Z.; Chueh, C. C.; Li, N.; Mao, C.; Jen, A. K., Realizing Efficient Lead-Free Formamidinium Tin Triiodide Perovskite Solar Cells via a Sequential Deposition Route. *Adv Mater* **2018**, *30* (6).
199. Ozaki, M.; Katsuki, Y.; Liu, J.; Handa, T.; Nishikubo, R.; Yakumaru, S.; Hashikawa, Y.; Murata, Y.; Saito, T.; Shimakawa, Y.; Kanemitsu, Y.; Saeki, A.; Wakamiya, A., Solvent-Coordinated Tin Halide Complexes as Purified Precursors for Tin-Based Perovskites. *ACS Omega* **2017**, *2* (10), 7016-7021.
200. Koh, T. M.; Krishnamoorthy, T.; Yantara, N.; Shi, C.; Leong, W. L.; Boix, P. P.; Grimsdale, A. C.; Mhaisalkar, S. G.; Mathews, N., Formamidinium tin-based perovskite with low Eg for photovoltaic applications. *Journal of Materials Chemistry A* **2015**, *3* (29), 14996-15000.
201. Grimme, S.; Antony, J.; Ehrlich, S.; Krieg, H., A consistent and accurate ab initio parametrization of density functional dispersion correction (DFT-D) for the 94 elements H-Pu. *The Journal of Chemical Physics* **2010**, *132* (15), 154104.
202. Grimme, S.; Ehrlich, S.; Goerigk, L., Effect of the damping function in dispersion corrected density functional theory. *Journal of Computational Chemistry* **2011**, *32* (7), 1456-1465.
203. Steiner, S.; Khmelevskiy, S.; Marsmann, M.; Kresse, G., Calculation of the magnetic anisotropy with projected-augmented-wave methodology and the case study of disordered $\text{Fe}_{1-x}\text{Co}_x$ alloys. *Physical Review B* **2016**, *93* (22), 224425.
204. Schueller, E. C.; Laurita, G.; Fabini, D. H.; Stoumpos, C. C.; Kanatzidis, M. G.; Seshadri, R., Crystal Structure Evolution and Notable Thermal Expansion in Hybrid Perovskites Formamidinium Tin Iodide and Formamidinium Lead Bromide. *Inorganic Chemistry* **2018**, *57* (2), 695-701.
205. Kahmann, S.; Nazarenko, O.; Shao, S.; Hordiichuk, O.; Kepenekian, M.; Even, J.; Kovalenko, M. V.; Blake, G. R.; Loi, M. A., Negative Thermal Quenching in FASnI₃ Perovskite Single Crystals and Thin Films. *ACS Energy Letters* **2020**, *5* (8), 2512-2519.
206. Frisch, M. J.; Trucks, G. W.; Schlegel, H. B.; Scuseria, G. E.; Robb, M. A.; Cheeseman, J. R.; Scalmani, G.; Barone, V.; Petersson, G. A.; Nakatsuji, H.; Li, X.; Caricato, M.; Marenich, A. V.; Bloino, J.; Janesko, B. G.; Gomperts, R.; Mennucci, B.; Hratchian, H. P.; Ortiz, J. V.; Izmaylov, A. F.; Sonnenberg, J. L.; Williams-Young, D.; Ding, F.; Lipparini, F.; Egidi, F.; Goings, J.; Peng, B.; Petrone, A.; Henderson, T.; Ranasinghe, D.; Zakrzewski, V. G.; J. Gao; Rega, N.; Zheng, G.; Liang, W.; Hada, M.; Ehara, M.; Toyota, K.; Fukuda, R.; Hasegawa, J.; Ishida, M.; Nakajima, T.; Honda, Y.; Kitao, O.; Nakai, H.; Vreven, T.; Throssell, K.; J. A. Montgomery, J.; Peralta, J. E.; Ogliaro, F.; Bearpark, M. J.; Heyd, J. J.; Brothers, E. N.; Kudin, K. N.; Staroverov, V. N.; Keith, T. A.; Kobayashi, R.; Normand, J.; Raghavachari, K.; Rendell, A. P.; Burant, J. C.; Iyengar, S. S.; Tomasi, J.; Cossi, M.; Millam, J. M.; Klene, M.; Adamo, C.; Cammi, R.; Ochterski, J. W.; Martin, R. L.; Morokuma, K.; Farkas, O.; Foresman, J. B.; Fox, a. D. J. *Gaussian 16, Revision A.03*, Gaussian, Inc.: Wallingford CT, 2016.

207. Zhao, Y.; Truhlar, D. G., The M06 Suite of Density Functionals for Main Group Thermochemistry, Thermochemical Kinetics, Noncovalent Interactions, Excited States, and Transition Elements: Two New Functionals and Systematic Testing of Four M06-Class Functionals and 12 Other Functionals. *Theor. Chem. Acc.* **2008**, *120* (1), 215.
208. Hariharan, P. C.; Pople, J. A., The Influence of Polarization Functions on Molecular Orbital Hydrogenation Energies. *Theor. Chim. Acta* **1973**, *28* (3), 213.
209. Hehre, W. J.; Ditchfield, R.; Pople, J. A., Self—Consistent Molecular Orbital Methods. XII. Further Extensions of Gaussian—Type Basis Sets for Use in Molecular Orbital Studies of Organic Molecules. *J. Chem. Phys.* **1972**, *56* (5), 2257.
210. Petersson, G. A.; Al-Laham, M. A., A Complete Basis Set Model Chemistry. II. Open-shell Systems and the Total Energies of the First-row Atoms. *J. Chem. Phys.* **1991**, *94* (9), 6081.
211. Petersson, G. A.; Bennett, A.; Tensfeldt, T. G.; Al-Laham, M. A.; Shirley, W. A.; Mantzaris, J., A Complete Basis Set Model Chemistry. I. The Total Energies of Closed-shell Atoms and Hydrides of the First-row Elements. *J. Chem. Phys.* **1988**, *89* (4), 2193.
212. Stroppa, A.; Di Sante, D.; Barone, P.; Bokdam, M.; Kresse, G.; Franchini, C.; Whangbo, M.-H.; Picozzi, S., Tunable ferroelectric polarization and its interplay with spin-orbit coupling in tin iodide perovskites. *Nature Communications* **2014**, *5* (1), 5900.
213. Kepenekian, M.; Robles, R.; Katan, C.; Saponi, D.; Pedesseau, L.; Even, J., Rashba and Dresselhaus Effects in Hybrid Organic–Inorganic Perovskites: From Basics to Devices. *ACS Nano* **2015**, *9* (12), 11557-11567.
214. Kim, G.-W.; Kang, G.; Malekshahi Byranvand, M.; Lee, G.-Y.; Park, T., Graded Mixed Hole Transport Layer in a Perovskite Solar Cell: Improving Moisture Stability and Efficiency. *ACS Applied Materials & Interfaces* **2017**, *9* (33), 27720-27726.
215. Kittel, C., *Introduction to Solid State Physics*. 8th ed.; Wiley: 2004.
216. Grote, C.; Berger, R. F., Strain Tuning of Tin–Halide and Lead–Halide Perovskites: A First-Principles Atomic and Electronic Structure Study. *The Journal of Physical Chemistry C* **2015**, *119* (40), 22832-22837.
217. Jung, Y.-K.; Lee, J.-H.; Walsh, A.; Soon, A., Influence of Rb/Cs Cation-Exchange on Inorganic Sn Halide Perovskites: From Chemical Structure to Physical Properties. *Chemistry of Materials* **2017**, *29* (7), 3181-3188.
218. Yang, W.-F.; Igbari, F.; Lou, Y.-H.; Wang, Z.-K.; Liao, L.-S., Tin Halide Perovskites: Progress and Challenges. *Advanced Energy Materials* **2020**, *10* (13), 1902584.
219. Kim, J. Y.; Lee, J.-W.; Jung, H. S.; Shin, H.; Park, N.-G., High-Efficiency Perovskite Solar Cells. *Chemical Reviews* **2020**, *120* (15), 7867-7918.
220. Jung, Y.-K.; Butler, K. T.; Walsh, A., Halide Perovskite Heteroepitaxy: Bond Formation and Carrier Confinement at the PbS–CsPbBr₃ Interface. *The Journal of Physical Chemistry C* **2017**, *121* (49), 27351-27356.
221. Harding, C. R.; Cann, J.; Laventure, A.; Sadeghianlemraski, M.; Abd-Ellah, M.; Rao, K. R.; Gelfand, B. S.; Aziz, H.; Kaake, L.; Risko, C.; Welch, G. C., Acid dyeing for green solvent processing of solvent resistant semiconducting organic thin films. *Materials Horizons* **2020**, *7* (11), 2959-2969.

222. Hay, P. J.; Wadt, W. R., Ab Initio Effective Core Potentials for Molecular Calculations. Potentials for the Transition Metal Atoms Sc to Hg. *J. Chem. Phys.* **1985**, *82* (1), 270.
223. Hay, P. J.; Wadt, W. R., Ab initio effective core potentials for molecular calculations. Potentials for K to Au including the outermost core orbitals. *Journal of Chemical Physics* **1985**, *82*, 299.
224. Wadt, W. R.; Hay, P. J., Ab Initio Effective Core Potentials for Molecular Calculations. Potentials for Main Group Elements Na to Bi. *J. Chem. Phys.* **1985**, *82* (1), 284.
225. Dennington, R.; Keith, T. A.; Millam, J. M. *GaussView, Version 5.0.9*, Semichem Inc., Shawnee Mission: KS, 2009.
226. Marenich, A. V.; Cramer, C. J.; Truhlar, D. G., Universal Solvation Model Based on Solute Electron Density and on a Continuum Model of the Solvent Defined by the Bulk Dielectric Constant and Atomic Surface Tensions. *The Journal of Physical Chemistry B* **2009**, *113* (18), 6378-6396.
227. Ho, J.; Zwicker, V. E.; Yuen, K. K. Y.; Jolliffe, K. A., Quantum Chemical Prediction of Equilibrium Acidities of Ureas, Deltamides, Squaramides, and Croconamides. *The Journal of Organic Chemistry* **2017**, *82* (19), 10732-10736.
228. Shields, G. C.; Seybold, P. G., *Computational Approaches for the Prediction of pKa Values*. 1st Edition ed.; CRC Press: Boca Raton, Florida, 2014.
229. Liptak, M. D.; Shields, G. C., Accurate pKa Calculations for Carboxylic Acids Using Complete Basis Set and Gaussian-n Models Combined with CPCM Continuum Solvation Methods. *Journal of the American Chemical Society* **2001**, *123* (30), 7314-7319.
230. Chipman, D. M., Computation of pKa from Dielectric Continuum Theory. *The Journal of Physical Chemistry A* **2002**, *106* (32), 7413-7422.
231. Ribeiro, R. F.; Marenich, A. V.; Cramer, C. J.; Truhlar, D. G., Use of Solution-Phase Vibrational Frequencies in Continuum Models for the Free Energy of Solvation. *The Journal of Physical Chemistry B* **2011**, *115* (49), 14556-14562.
232. Ho, J., Are thermodynamic cycles necessary for continuum solvent calculation of pKas and reduction potentials? *Physical Chemistry Chemical Physics* **2015**, *17* (4), 2859-2868.
233. Percec, V.; Peterca, M.; Tadjiev, T.; Zeng, X.; Ungar, G.; Leowanawat, P.; Aqad, E.; Imam, M. R.; Rosen, B. M.; Akbey, U.; Graf, R.; Sekharan, S.; Sebastiani, D.; Spiess, H. W.; Heiney, P. A.; Hudson, S. D., Self-Assembly of Dendronized Perylene Bisimides into Complex Helical Columns. *Journal of the American Chemical Society* **2011**, *133* (31), 12197-12219.
234. Schwartz, P.-O.; Biniek, L.; Zaborova, E.; Heinrich, B.; Brinkmann, M.; Leclerc, N.; Méry, S., Perylenediimide-Based Donor-Acceptor Dyads and Triads: Impact of Molecular Architecture on Self-Assembling Properties. *Journal of the American Chemical Society* **2014**, *136* (16), 5981-5992.
235. Zhang, J.; Bai, F.; Li, Y.; Hu, H.; Liu, B.; Zou, X.; Yu, H.; Huang, J.; Pan, D.; Ade, H.; Yan, H., Intramolecular π -stacked perylene-diimide acceptors for non-fullerene organic solar cells. *Journal of Materials Chemistry A* **2019**, *7* (14), 8136-8143.

236. Smieja, J. M.; Benson, E. E.; Kumar, B.; Grice, K. A.; Seu, C. S.; Miller, A. J. M.; Mayer, J. M.; Kubiak, C. P., Kinetic and Structural Studies, Origins of Selectivity, and Interfacial Charge Transfer in the Artificial Photosynthesis of CO. *Proc. Natl. Acad. Sci. U. S. A.* **2012**, *109* (39), 15646.
237. Sahara, G.; Ishitani, O., Efficient Photocatalysts for CO₂ Reduction. *Inorg. Chem.* **2015**, *54*, 5096.
238. Lang, P.; Pfrunder, M.; Quach, G.; Braun-Cula, B.; Moore, E. G.; Schwalbe, M., Sensitized Photochemical CO₂ Reduction by Hetero-Pacman Compounds Linking a ReI Tricarbonyl with a Porphyrin Unit. *Chem. - Eur. J.* **2019**, *25* (17), 4509.
239. Machan, C. W.; Sampson, M. D.; Chabolla, S. A.; Dang, T.; Kubiak, C. P., Developing a Mechanistic Understanding of Molecular Electrocatalysts for CO₂ Reduction Using Infrared Spectroelectrochemistry. *Organometallics* **2014**, *33* (18), 4550.
240. Riplinger, C.; Sampson, M. D.; Ritzmann, A. M.; Kubiak, C. P.; Carter, E. A., Mechanistic Contrasts between Manganese and Rhenium Bipyridine Electrocatalysts for the Reduction of Carbon Dioxide. *J. Am. Chem. Soc.* **2014**, *136* (46), 16285.
241. Grice, K. A.; Gu, N. X.; Sampson, M. D.; Kubiak, C. P., Carbon Monoxide Release Catalysed by Electron Transfer: Electrochemical and Spectroscopic Investigations of [Re(Bpy-R)(CO)₄](OTf) Complexes Relevant to CO₂ Reduction. *Dalton Trans.* **2013**, *42* (23), 8498.
242. Marenich, A. V.; Cramer, C. J.; Truhlar, D. G., Universal Solvation Model Based on Solute Electron Density and on a Continuum Model of the Solvent Defined by the Bulk Dielectric Constant and Atomic Surface Tensions. *J. Phys. Chem. B* **2009**, *113* (18), 6378.
243. Schaugaard, R. N.; Raghavachari, K.; Li, L., Redox “Innocence” of Re(I) in Electrochemical CO₂ Reduction Catalyzed by Nanographene-Re Complexes. *Inorg. Chem.* **2018**, *57* (17), 10548.
244. Oh, S.; Gallagher, J. R.; Miller, J. T.; Surendranath, Y., Graphite-Conjugated Rhenium Catalysts for Carbon Dioxide Reduction. *J. Am. Chem. Soc.* **2016**, *138* (6), 1820.
245. Reuillard, B.; Ly, K. H.; Rosser, T. E.; Kuehnel, M. F.; Zebger, I.; Reisner, E., Tuning Product Selectivity for Aqueous CO₂ Reduction with a Mn(Bipyridine)-Pyrene Catalyst Immobilized on a Carbon Nanotube Electrode. *J. Am. Chem. Soc.* **2017**, *139* (41), 14425.
246. Orchanian, N. M.; Hong, L. E.; Marinescu, S. C., Immobilized Molecular Wires on Carbon-Cloth Electrodes Facilitate CO₂ Electrolysis. *ACS Catal.* **2019**, *9* (10), 9393.
247. Orchanian, N. M.; Hong, L. E.; Skrainka, J. A.; Esterhuizen, J. A.; Popov, D. A.; Marinescu, S. C., Surface-Immobilized Conjugated Polymers Incorporating Rhenium Bipyridine Motifs for Electrocatalytic and Photocatalytic CO₂ Reduction. *ACS Appl. Energy Mater.* **2019**, *2* (1), 110.
248. Willkomm, J.; Bertin, E.; Atwa, M.; Lin, J. B.; Birss, V.; Piers, W. E., Grafting of a Molecular Rhenium CO₂ Reduction Catalyst onto Colloid-Imprinted Carbon. *ACS Appl. Energy Mater.* **2019**, *2* (4), 2414.
249. Sinha, S.; Sonea, A.; Shen, W.; Hanson, S. S.; Warren, J. J., Heterogeneous Aqueous CO₂ Reduction Using a Pyrene-Modified Rhenium(I) Diimine Complex. *Inorg. Chem.* **2019**, *58* (16), 10454.

250. Luna, P. D.; Hahn, C.; Higgins, D.; Jaffer, S. A.; Jaramillo, T. F.; Sargent, E. H., What Would It Take for Renewably Powered Electrosynthesis to Displace Petrochemical Processes? *Science* **2019**, *364* (6438), eaav3506.
251. Qiao, X.; Li, Q.; Schaugaard, R. N.; Noffke, B. W.; Liu, Y.; Li, D.; Liu, L.; Raghavachari, K.; Li, L.-s., Well-Defined Nanographene–Rhenium Complex as an Efficient Electrocatalyst and Photocatalyst for Selective CO₂ Reduction. *Journal of the American Chemical Society* **2017**, *139* (11), 3934-3937.
252. Wang, M.; Torbensen, K.; Salvatore, D.; Ren, S.; Joulié, D.; Dumoulin, F.; Mendoza, D.; Lassalle-Kaiser, B.; İsci, U.; Berlinguette, C. P.; Robert, M., CO₂ Electrochemical Catalytic Reduction with a Highly Active Cobalt Phthalocyanine. *Nat. Commun.* **2019**, *10* (1), 1.
253. Ren, S.; Joulié, D.; Salvatore, D.; Torbensen, K.; Wang, M.; Robert, M.; Berlinguette, C. P., Molecular Electrocatalysts Can Mediate Fast, Selective CO₂ Reduction in a Flow Cell. *Science* **2019**, *365* (6451), 367.

VITA

Name

Keerthan Raghavendra Rao

Education

B.E. Visveswaraya Technological University, Belgaum, 2016

MS. Purdue University, West Lafayette, 2017

PhD. University of Kentucky, Lexington, 2023